AD-A057 786 MISSOURI UNIV-COLUMBIA RESEARCH REACTOR FACILITY F/G 20/12
SILICON DETECTOR COMPENSATION BY NUCLEAR TRANSMUTATION.(U)
FEB 78 J M MEESE F33615-76-C-5230

UNCLASSIFIED AFML-TR-77-178 NL

1 OF 2

AD
A057786

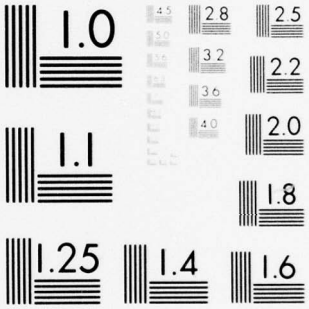

MICROCOPY RESOLUTION TEST CHART
NATIONAL BUREAU OF STANDARDS 1963-A

LEVEL II
A038471
ADA057786
AD NO.
DDC FILE COPY

AFML-TR-77-178

SILICON DETECTOR COMPENSATION BY NUCLEAR TRANSMUTATION

UNIVERSITY OF MISSOURI
RESEARCH REACTOR FACILITY (MURR)
COLUMBIA, MISSOURI 65201

FEBRUARY 1978

TECHNICAL REPORT AFML-TR-77-178
Final Technical Report for Period 30 June 1976 to 31 July 1977

DDC
RECEIVED
AUG 21 1978
A

Approved for public release; distribution unlimited.

AIR FORCE MATERIALS LABORATORY
AIR FORCE WRIGHT AERONAUTICAL LABORATORIES
AIR FORCE SYSTEMS COMMAND
WRIGHT-PATTERSON AIR FORCE BASE, OHIO 45433

78 08 18 071

NOTICE

When Government drawings, specifications, or other data are used for any purpose other than in connection with a definitely related Government procurement operation, the United States Government thereby incurs no responsibility nor any obligation whatsoever; and the fact that the government may have formulated, furnished, or in any way supplied the said drawings, specifications, or other data, is not to be regarded by implication or otherwise as in any manner licensing the holder or any other person or corporation, or conveying any rights or permission to manufacture, use, or sell any patented invention that may in any way be related thereto.

This report has been reviewed by the Information Office (OI) and is releasable to the National Technical Information Service (NTIS). At NTIS, it will be available to the general public, including foreign nations.

This technical report has been reviewed and is approved for publication.

Robert J. Spry

ROBERT J. SPRY
Project Engineer

FOR THE COMMANDER

W G D Frederick

WILLIAM G. D. FREDERICK, Chief
Laser & Optical Materials Branch
Electromagnetic Materials Division
Air Force Materials Laboratory

"If your address has changed, if you wish to be removed from our mailing list, or if the addressee is no longer employed by your organization please notify AFML/LPO *,W-PAFB, OH 45433 to help us maintain a current mailing list".*

Copies of this report should not be returned unless return is required by security considerations, contractual obligations, or notice on a specific document.

AIR FORCE/56780/26 July 1978 — 225

UNCLASSIFIED

SECURITY CLASSIFICATION OF THIS PAGE (When Data Entered)

REPORT DOCUMENTATION PAGE

READ INSTRUCTIONS BEFORE COMPLETING FORM

1. REPORT NUMBER: AFML-TR-77-178

2. GOVT ACCESSION NO.

3. RECIPIENT'S CATALOG NUMBER

4. TITLE (and Subtitle): SILICON DETECTOR COMPENSATION BY NUCLEAR TRANSMUTATION.

5. TYPE OF REPORT & PERIOD COVERED: Final Technical Report. 30 June 76 — 31 July 77

6. PERFORMING ORG. REPORT NUMBER

7. AUTHOR(s): J. M. Meese

8. CONTRACT OR GRANT NUMBER(s): F33615-76-C-5230

9. PERFORMING ORGANIZATION NAME AND ADDRESS: University of Missouri, Research Reactor Facility, Columbia, Missouri 65201

10. PROGRAM ELEMENT, PROJECT, TASK AREA & WORK UNIT NUMBERS: WU. ILIR0080

11. CONTROLLING OFFICE NAME AND ADDRESS: Air Force Materials Laboratory, Air Force Systems Command, Wright Patterson AFB, Ohio 45433

12. REPORT DATE: Feb 78

13. NUMBER OF PAGES: 164

14. MONITORING AGENCY NAME & ADDRESS (if different from Controlling Office)

15. SECURITY CLASS. (of this report): UNCLASSIFIED

15a. DECLASSIFICATION/DOWNGRADING SCHEDULE

16. DISTRIBUTION STATEMENT (of this Report)

Approved for public release, distribution unlimited.

17. DISTRIBUTION STATEMENT (of the abstract entered in Block 20, if different from Report)

18. SUPPLEMENTARY NOTES

19. KEY WORDS (Continue on reverse side if necessary and identify by block number)

Silicon, NTD, Neutron Transmutation Doping, IR Detectors, Radiation Damage, Ga-Doped Silicon, Semiconductor, Compensation

20. ABSTRACT (Continue on reverse side if necessary and identify by block number)

The effects of nuclear transmutation doping in high quality detector grade silicon have been studied. A theoretical treatment of the variations of electrical parameters with fluence and the experimental isochronal annealings of float zone Si, transmutation doped ~~at MURR but obtained from a variety of~~ sources, are presented. It is found that several annealing stages observed previously only in Czochralski Si are also observed in this lightly compensated float zone Si. A large concentration of acceptors is produced as a result of thermal irradiation and annealing to 500°C. This concentration is

next page

DD FORM 1 JAN 73 1473 EDITION OF 1 NOV 65 IS OBSOLETE

UNCLASSIFIED

SECURITY CLASSIFICATION OF THIS PAGE (When Data Entered)

410 149

independent of fluence and appears to be related to residual Si impurities previously undetected by electrical, optical or neutron activation analysis experiments. Defect decoration of oxygen or carbon impurities is believed to be the source of these acceptors. Techniques have been devised to produce very high resistivities as a result of high precision nuclear transmutation compensation in nominally undoped material. The effect of isochronal annealing on compensation of residual boron states in Ga doped detector grade material has been studied. A theoretical and experimental study has been made of resistivity fluctuation as a function of neutron transmutation compensation ratio of phosphorus to boron. Transmutation compensation in IR detector Si is indeed possible to a high degree of accuracy and the wafer uniformity obtained is far superior to that obtained by conventional techniques.

PREFACE

This final report describes work performed by personnel of the University of Missouri Research Reactor Facility, Columbia, Missouri 65201, during the period from 30 June 1976 to 31 July 1977, under Contract F33615-76-C-5230, Work Unit ILIR0080. The program was monitored by Dr. Robert J. Spry, Air Force Materials Laboratory, Air Force Systems Command, Wright-Patterson Air Force Base, Ohio.

The program was directed toward the compensation of residual boron in infrared detector grade silicon by nuclear transmutation doping. This investigation was conducted by Dr. J. M. Meese, principal investigator, Dr. D. M. Alger, Mr. S. L. Gunn, Mr. W. F. Richardson, Mr. P. J. Glairon, Dr. D. M. McKown, and Dr. J. Steven Morris.

ACCESSION for
NTIS White Section
DDC Buff Section
UNANNOUNCED
JUSTIFICATION
BY
DISTRIBUTION/AVAILABILITY CODES
Dist. AVAIL. and/or SPECIAL
A

78 08 18 071

TABLE OF CONTENTS

		Page
I.	INTRODUCTION	1
II.	THEORETICAL ANALYSIS	4
III.	EXPERIMENTAL TECHNIQUES AND APPARATUS	29
	A. Reactor Description	29
	B. Bulk Pool Variable Flux Irradiation Facility	33
	C. Neutron Flux Detection and Integration System	36
	D. Neutron Activation Analysis Systems	40
	E. Four-point and Thermal Probes	40
	F. Minority Carrier Lifetime Apparatus	47
	G. High Impedance Van der Pauw Resistivity and Hall System (Electronics, Vacuum System, Helitran)	51
	H. Photoconductivity System	54
	I. Miscellaneous: Sample Preparation Equipment, Annealing System, Irradiation of Silicon, Post-Irradiation Handling	58
IV.	EXPERIMENTAL RESULTS AND DISCUSSION	59
	A. Materials Evaluation Before Irradiation	62
	B. Neutron Activation Analysis	83
	C. Irradiation and Annealing Experiments	90
V.	PROGRESS AND ACCOMPLISHMENTS	156
VI.	REFERENCES	162

PRECEDING PAGE NOT FILMED
BLANK

LIST OF ILLUSTRATIONS

Figure		Page
1.	Resistivity and carrier concentration vs. fluence	14
2.	Expanded fluence scale plot of Figure 1	15
3.	Resistivity vs. fluence	19
4.	Hall mobility vs. fluence	20
5.	Hall coefficient vs. fluence	21
6.	Actual carrier coefficient p, n, and Hall coefficient carrier concentration p_H, n_H, vs. fluence	22
7.	Final compensation ratio as a function of initial compensation ratio for various fluence ratios, ϕ/ϕ_c	26
8.	Comparison of research reactor peak flux values in the United States	31
9.	Flux trap, beamports, reflector and bulk pool facilities	32
10.	Thermal neutron flux profile in I-2 reflector position	34
11.	Movable box detail for bulk pool irradiation facility	35
12.	Support rods for variable flux facility	37
13.	Detector holder for variable flux facility	38
14.	Current vs. voltage for four point probe resistivity measurement (top of VZ-072-#5)	44
15.	Current vs. voltage for bottom of VZ-072-#5	45
16.	Typical photoconductive decay curves for determining minority carrier lifetime	49
17.	Minority carrier lifetime measurement apparatus	52
18.	Exponential decay generator	53
19.	Switching circuit for resistivity and Hall effect measurements	55

PRECEDING PAGE NOT FILMED BLANK

LIST OF ILLUSTRATIONS (Cont.)

Figure		Page
20.	Analog voltage amplifier and current source for digital Gaussmeter	56
21.	Analog to digital converter circuitry for digital Gaussmeter	57
22.	Axial resistivity and axial lifetime of 1 in. or 1/2 in. pieces from VZ-072	69
23.	Radial resistivity of VZ-072-1-top	70
24.	Radial resistivity of VZ-072-2-top	71
25.	Radial resistivity of VZ-072-3-top	72
26.	Radial resistivity of VZ-072-4-top	73
27.	Radial resistivity of VZ-072-5-top	74
28.	Radial resistivity of VZ-072-5-bottom	75
29.	Radial resistivity of a typical VZ-083 sample	76
30.	Radial resistivity of a typical Hughes wafer	77
31.	Carrier concentration vs. reciprocal temperature for a neutron transmutation doped Czochralski wafer	79
32.	Carrier concentration vs. reciprocal temperature for a Wacker Ga doped float zone wafer 102531-II (MURR-77)	84
33.	Carrier concentration vs. reciprocal temperature for a Rockwell Ga doped float zone wafer GZ-156-21 (MURR-85)	85
34.	Concentration of gold vs. percent of sample weight removed	91
35.	A comparison of isochronal annealing of transmutation doped float zone and Czochralski silicon	105
36.	Isochronal annealing of two float zone samples irradiated to produce ∿100 Ω-cm n-type	109

LIST OF ILLUSTRATIONS (Cont.)

Figure		Page
37.	Semilog plot of the ln of the reciprocal of the fraction of phosphorus not electrically active vs. reciprocal annealing temperature for the Topsil sample shown in Figure 36 . . .	112
38.	Isochronal annealing of resistivity and minority carrier lifetime of Rockwell float zone (argon anneal) bulk sample	116
39.	Argon isochronal anneal of Rockwell float zone wafer	117
40.	Argon isochronal anneal of Topsil wafer . . .	118
41.	Argon isochronal anneal of T.I. Lopex wafer .	119
42.	Vacuum isochronal anneal of Wacker wafer . . .	120
43.	Vacuum isochronal anneal of T.I. Lopex wafer .	121
44.	Vacuum isochronal anneal of Rockwell wafer . .	122
45.	Vacuum isochronal anneal of Topsil wafer . . .	123
46.	Comparison of vacuum and argon isochronal anneals for Topsil wafers	125
47.	Comparison of vacuum and argon isochronal anneals for T.I. Lopex wafers	126
48.	Argon isochronal anneal of Hughes wafer where $\phi \simeq \phi_c$	127
49.	Argon isochronal anneal of Topsil wafer irradiated to $\phi = 1.02\ \phi_c$	129
50.	Argon isochronal anneals of fast neutron damage. Thermal neutron flux was suppressed by using boron irradiation can.	132
51.	Annealing furnace tube, sample boat, and silicon spacers	135
52.	The effect of a final lap on $\rho(x)$	137

LIST OF ILLUSTRATIONS (Cont.)

Figure		Page
53.	$\rho(x)$ vs. x for undoped wafer from GZ-156, the ingot to be used for NTD detector fabrication .	143
54.	$\rho(x)$ vs. x before and after cleaving into a half wafer for VZ-083	144
55.	Isochronal argon anneals for transmutation compensated Ga doped Si	149
56.	Experimental and theoretical resistivity fluctuations as a function of phosphorus to boron concentration ratio for an initial resistivity fluctuation before compensation of 4.72%	151
57.	$\rho(x)$ vs. x data for various ratios of [P]/[B] obtained by nuclear transmutation doping and annealing	157

LIST OF TABLES

Table		Page
1.	Nuclear Data	4
2.	^{31}P - Theoretical Production Rates	6
3.	Typical Experimental Mobility Values in Si	7
4.	Integrator System Calibration Data	39
5.	A Comparison of Four-point Probe Resistivity Measurements Made at Rockwell and MURR	46
6.	Summary of Undoped Sample Characterization Before Irradiation	64
7.	Summary of Minority Carrier Lifetimes	67
8.	Summary of Drift Mobilities	68
9.	Summary of Analytical Conditions and Detection Limits for Neutron Activation Analysis of Silicon	88
10.	Elemental Concentrations Measured in Four Silicon Ingots	89
11.	Number of Displacements per Phosphorus Produced	98
12.	Summary of Irradiations (undoped material)	100
13.	Summary of Prominent Annealing Features	131
14.	Results of Single Temperature Annealing Procedure for Different Target Resistivities	141
15.	Summary of Irradiations (Ga doped Si)	146

I. INTRODUCTION

The primary objective of this program is to devise, through the research to be discussed, an optimum set of techniques capable of compensating the residual boron always found in detector grade silicon by the process of nuclear transmutation doping. The material to be developed by this program is intended for use in infrared detector systems such as those of the Air Force LADIR (Low Cost Arrays for the Detection of Infrared) program.

The best silicon available today contains residual boron, a shallow acceptor, in concentrations of the order of 10^{12}B/cm^3. This is because the segregation coefficient of this impurity is close to unity, and, therefore, will not be substantially removed by successive passes in a zone refiner. This residual boron concentration has several adverse effects on the operation of extrinsic photoconductor IR detectors fabricated from Ga or In doped silicon. Since the B ionization energy is less than those of Ga or In, the B levels thermally ionize at temperatures below those of the impurities of interest forcing the detectivity out of the background limited condition at prematurely low temperatures. This effect requires additional detector array cooling, which results in increased system weight and cost, to hold the detectors in the background limited region. As a result system size and cost increase unless these boron levels can be populated by carriers from compensating donor levels. Furthermore, the shallow boron optical transition is beyond the atmospheric transmission windows through which the IR data information is obtained. Therefore, these boron

optical transitions can respond to undesirable background thermal radiation to produce a type of nonuseful background noise.

Both of these problems can be eliminated with a minimum degradation in theoretical detector gain if nearly exact compensation of the boron acceptors is accomplished by the addition of shallow donors. Greatly overcompensating the boron, however, is undesirable because the additional donor carriers fill the Ga or In levels once all the B levels are compensated. This reduces detector gain by reducing the number of desirable optical transitions from which signal information is obtained. Additionally, the extra impurities from over-compensation represent additional charged impurity scattering centers reducing the carrier mobility, which is dominated by charged impurity scattering at the low temperatures at which these detectors operate. This lowering of carrier mobility reduces the gain of the detector, which is proportional to the product of mobility times lifetime. Carrier lifetime is also reduced by overcompensation since additional recombination centers are created.

Nuclear transmutation doping of silicon appears to offer several advantages over conventional doping techniques for producing the desired compensating donor concentration. Briefly, the transmutation doping process is based on the conversion of the isotope ^{30}Si to ^{31}Si through an (n, γ) reaction induced by thermal neutron capture during reactor irradiation. The ^{31}Si isotope is unstable and decays through β^- emission to ^{31}P, the desired donor impurity. Since the production rate of ^{31}P is $3.355\ ppb/10^{18} n/cm^2$, the production of donors is slow enough to

provide careful control of the dopant concentration. Furthermore, the donors added by transmutation doping are distributed uniformly throughout the lattice because the microscopic abundance ratios of the Si isotopes are uniform and the thermal neutron diffusion length is very long compared to typical ingot dimensions.

The two major advantages of NTD-Si, tight control over doping concentration and uniformity of dopant distribution, are somewhat offset by the radiation damage effects which occur during irradiation. These effects cause no difficulty for float zone Si neutron doped to a resistivity of 100 Ω-cm or lower. For higher final resistivity material, the success or failure depends intimately on residual impurity defect interactions and their annealing properties. One of the major goals of the present research is to define the limits of final resistivity which can be achieved relative to the properties of the starting material.

The balance of this report is contained in five major sections as follows:

- Section II develops the theoretical tools to understand the expected electrical properties resulting from transmutation doped Si as functions of neutron fluence. A discussion of the transmutation doping process is also presented.
- Section III is a description of the experimental techniques and apparatus employed throughout this work.
- Section IV gives a description of the experimental results and a discussion of possible interpretations.

- Section V discusses the significant accomplishments achieved during the program and discusses areas of difficulty where further research will be required.

II. THEORETICAL ANALYSIS

The basic physics of transmutation doping in Si has been discussed by Tanenbaum and Mills.[1] Although they discuss all possible nuclear reactions with all the silicon and oxygen isotopes such as (n, γ), (n, 2n), (n, p), and (n, α), we will confine our attention to the (n, γ) reactions with Si as being the only significant reactions in a thermal neutron flux. This viewpoint has been verified experimentally.[1]

The natural abundance, thermal neutron (n, γ) absorption cross section and half-lives of the relevant isotopes of silicon and phosphorus are listed in Table 1.

Table 1. Nuclear Data.

Natural Abundance	Isotope	$\sigma(n, \gamma)$	$T_{1/2}$
92.27%	^{28}Si	0.08 ± 0.03 b	stable
4.68%	^{29}Si	0.28 ± 0.09 b	stable
3.05%	^{30}Si	0.11 ± 0.01 b	2.62h
100%	^{31}P	0.20 ± 0.02 b	14.3d
At. Wgt. Si = 28.086, N(Si) = 4.996×10^{22} atoms/cm^3			
Density Si = 2.33 gm/cm^3			

The nuclear reactions of interest are the following:

$$^{28}Si\ (n, \gamma)\ ^{29}Si \qquad (1)$$

$$^{29}Si\ (n, \gamma)\ ^{30}Si \qquad (2)$$

$$^{30}Si\ (n,\ \gamma)\ ^{31}Si \rightarrow\ ^{31}P + \beta^- \qquad (3)$$

$$T_{1/2} = 2.62h$$

$$^{31}P\ (n,\ \gamma)\ ^{32}P \rightarrow\ ^{32}S + \beta^- \qquad (4)$$

$$T_{1/2} = 14.3d$$

The first two reactions redistribute the natural abundance of the silicon isotopes but do not lead to any doping effects or radioactivity. Reaction (2) is quite fortunate in that it serves to replace the ^{30}Si isotope approximately as it is burned up in reaction (3) which produces the dopant ^{31}P. Reaction (4) transmutes the stable isotope ^{31}P to the unstable isotope ^{32}P which β^- decays to ^{32}S. Since reaction (4) is a second order effect, the doping is thought to be negligible compared to the doping from ^{31}P (see Ref. 1). This reaction is important, however, as the primary source of radioactivity for times which are long compared to the half-life of reaction (3).

From the data given in Table 1, we can calculate the production rate of the desired dopant. The total number of Si atoms/cm^3 is found to be

$$N(Si) = \frac{2.33\ (6.023 \times 10^{22})}{28.086} = 4.996 \times 10^{22}\ \text{atoms/cm}^3.$$

The density of ^{30}Si isotopes is then found to be

$$N(^{30}Si) = 0.0305\ N(Si) = 1.524 \times 10^{21}\ \text{atoms/cm}^3.$$

The theoretical production rate for phosphorus is then found from the expression

$$\frac{d[^{31}P]}{d\Phi} = N(^{30}Si)\ \sigma[^{30}Si\ (n, \gamma)\ ^{31}Si]$$

$$= 1.676 \times 10^{-4}\ \ ^{31}P \text{ atoms/cm}^3/\text{n/cm}^2$$

where Φ is the irradiation fluence of thermal neutrons (n/cm^2). Table 2 lists the theoretical production of donors in Si in several useful sets of units.

TABLE 2. ^{31}P-Theoretical Production Rates.

Production Rate (K)	Units
1.676×10^{-4}	P atoms/cm^3 per n/cm^2
1.676×10^{14}	P atoms/cm^3 per 10^{18} n/cm^2
3.355	ppb per 10^{18} n/cm^2

Knowing the concentration of donors added per unit fluence, it is now possible to calculate the final resistivity after irradiation and annealing from the starting resistivity if the mobility of the majority carrier is known. To this end an analysis of mobility data for Si has been performed on data taken from two review papers.[2,3] Since these authors quote the same references but give different values, we have averaged when this has occurred. We have also discarded three values which differed abnormally from the mean, μ_{Hn} = 1345, μ_{Dn} = 1590, and μ_{Dp}=356 cm^2/V-sec.

The result of the average of all other data is summarized in Table 3.

TABLE 3. **Typical Experimental Mobility Values in Si.**

$$\mu_{Dp} = (494 \pm 11)\ cm^2/V\text{-}sec$$

$$\mu_{Dn} = (1396 \pm 64)\ cm^2/V\text{-}sec$$

$$r_p = \mu_H/\mu_D = 0.77 \pm 0.06$$

$$r_n = 1.3 \pm 0.1$$

$$b = \mu_n/\mu_p = 2.826$$

$$p = \frac{[e\mu_p]^{-1}}{\rho} = \frac{(1.265 \pm 0.29) \times 10^{16}\ cm^{-3}}{\rho}$$

$$= \frac{(253 \pm 5.7)\ ppb}{\rho}$$

$$n = \frac{[e\mu_n]^{-1}}{\rho} = \frac{(4.477 \pm 0.197) \times 10^{15}\ cm^{-3}}{\rho}$$

$$= \frac{(89.54 \pm 3.94)\ ppb}{\rho}$$

These expressions will be useful expressions for estimating the ppb added by neutron irradiation in the sections to follow.

If the initial and final carrier concentrations are large at room temperature compared to the number of intrinsic carriers, then the following expressions for the carrier densities in terms of donor and acceptor concentrations are

$$p_o = N_A - N_{D_o}, \qquad \text{p-type starting material}$$

$$n_o = N_{D_o} - N_A, \qquad \text{n-type starting material}$$

$$p_f = N_A - N_{D_f}, \qquad \text{p-type ending material}$$

$$n_f = N_{D_f} - N_A, \qquad \text{n-type ending material}$$

then,

$$n_f - n_o = N_{D_f} - N_{D_o}, \qquad \text{n-type to n-type}$$

$$n_f + p_o = N_{D_f} - N_{D_o}, \qquad \text{p-type to n-type}$$

$$p_o - p_f = N_{D_f} - N_{D_o}, \qquad \text{p-type to p-type.}$$

But $N_{D_f} - N_{D_o}$ is just the concentration of donors added by transmutation which we will call $N_P = K\Phi$ where K is the production rate given in Table 2 and Φ is the fluence (number of neutrons/cm^2). Therefore, we see that in all cases for which n_i can be neglected, the concentration of phosphorus added can be determined by the concentrations of uncompensated carriers and the material type.

We can determine the concentration, N_P, of phosphorus atoms added either from the fluence Φ or the initial and final resistivities and types using the following expressions,

$$N_P = K\Phi = \left[3.355 \times 10^{-18} \frac{\text{ppb}}{\text{n/cm}^2}\right] \Phi \qquad (5)$$

$$N_p = \begin{cases} \dfrac{K_n}{\rho_{n_f}} - \dfrac{K_n}{\rho_{n_o}} & \text{n-type} \rightarrow \text{n-type} \\[2ex] \dfrac{K_n}{\rho_{n_f}} + \dfrac{K_p}{\rho_{p_o}} & \text{p-type} \rightarrow \text{n-type} \\[2ex] \dfrac{K_p}{\rho_{p_o}} - \dfrac{K_p}{\rho_{p_f}} & \text{p-type} \rightarrow \text{p-type} \end{cases} \tag{6}$$

where K_n = 89.54 ppb Ω-cm and K_p = 253 ppb Ω-cm. The conversion between ppb and atoms/cm^3 is 1 ppb = 4.996 x 10^{13} atoms/cm^3.

By equating the two expressions above, the fluence necessary to obtain a desired final resistivity can be determined from the initial resistivity and type as

$$\Phi = \begin{cases} \dfrac{K_n}{K_\bullet} (\rho_{n_f}^{-1} - \rho_{n_o}^{-1}) & \text{n-type} \rightarrow \text{n-type} \\[2ex] \dfrac{K_n}{K} \rho_{n_f}^{-1} + \dfrac{K_p}{K} \rho_{p_o}^{-1} & \text{p-type} \rightarrow \text{n-type} \\[2ex] \dfrac{K_p}{K} (\rho_{p_o}^{-1} - \rho_{p_f}^{-1}). & \text{p-type} \rightarrow \text{p-type} \end{cases} \tag{7}$$

The resistivity after irradiation and annealing as a function of fluence can also be calculated for those cases where n_i is not negligible compared to the majority carrier concentration.

The resistivity vs fluence has been calculated for transmutation doped samples using the following assumptions:

1. 100% electrical activity is obtained by annealing.
2. The mobilities remain constant and are taken as μ_n = 1500 cm^2/V-sec, μ_p = 600 cm^2/V-sec in the following figures. [S.M. Sze, Physics of Semiconductor Devices, Wiley, New York (1969)].

3. The shallow donors and acceptors are completely ionized at room temperature.

4. The production rate of phosphorus is given by K = 3.355 ppb/10^{18}n/cm^2, which is obtained from the cross-section.

5. The number of intrinsic carriers at room temperature is $n_i = 1.391 \times 10^{10} cm^{-3}$. [H.Y. Fan, Solid State Physics 1, 283 (1955)].

From charge conservation, the complete ionization assumption, and the relation

$$np = n_i^2$$

we obtain

$$p = 1/2\left[N_A - N_D + \sqrt{(N_A - N_D)^2 + 4n_i^2}\right].$$

For a production rate of donors given by K, this equation becomes for p-type material

$$p = 1/2\left[(N_A - N_D - K\phi) + \sqrt{(N_A - N_D - K\phi)^2 + 4n_i^2}\right]. \quad (8)$$

If we define the degree of initial compensation k_o by the expression

$$k_o = \frac{N_D}{N_A},$$

then the degree of compensation as a function of fluence is given by

$$k = \frac{N_D + K\phi}{N_A}.$$

For complete compensation, k = 1; for no compensation k = o. We define one more quantity, a, the degree of uncompensation by

$$a = 1-k = \frac{N_A - N_D - K\phi}{N_A} \cong \frac{p}{N_A}. \quad (9a)$$

For no irradiation, we assume that $p_o >> n_i$ so that

$$a_o = 1-k_o = \frac{N_A - N_D}{N_A} = \frac{p_o}{N_A} \quad . \tag{9b}$$

It can be shown by substitution of Eq. (9a) into Eq. (8) that

$$p = \frac{N_A}{2} \left[a + \sqrt{a^2 + \left(\frac{2n_i}{N_A}\right)^2} \right] . \tag{10}$$

We now define the fluence necessary for complete compensation as ϕ_c. This is obtained when k = 1 or a = o and is obtained from Eq. (9a)

$$o = 1 - 1 = \frac{N_A - N_D - K\phi_c}{N_A}$$

or

$$\phi_c = \frac{N_A - N_D}{K} = \frac{p_o}{K} \quad .$$

It can now be shown by substituting $K = (N_A - N_D)/\phi_c$ from the last equation into Eq. (9a) that

$$a = \left(1 - \frac{N_D}{N_A}\right) \left(1 - \frac{\phi}{\phi_c}\right)$$

$$= a_o \left(1 - \frac{\phi}{\phi_c}\right).$$

Then, from Eq. (10)

$$p = \frac{N_A a_o}{2} \left[\left(1 - \frac{\phi}{\phi_c}\right) + \sqrt{\left(1 - \frac{\phi}{\phi_c}\right)^2 + \left(\frac{2n_i}{N_A a_o}\right)^2} \right] .$$

But from Eq. (9a) with ϕ = o,

$$N_A a_o = p_o$$

therefore, we obtain

$$p = \frac{p_o}{2} \left[\left(1 - \frac{\phi}{\phi_c}\right) + \sqrt{\left(1 - \frac{\phi}{\phi_c}\right)^2 + \left(\frac{2n_i}{p_o}\right)^2} \right] . \tag{11}$$

It can similarly be shown for overcompensation (n-type produced)

$$n = \frac{p_o}{2} \left[- \left(1 - \frac{\phi}{\phi_c}\right) + \sqrt{\left(1 - \frac{\phi}{\phi_c}\right)^2 + \left(\frac{2n_i}{p_o}\right)^2} \right] . \tag{12}$$

It should be noted that the number of carriers is symmetrical with respect to the fluence on either side of $\phi = \phi_c$. It should also be noted that the number of free carriers as a function of fluence is independent of the degree of initial compensation. It can be shown that Eqs. (11) and (12) form a universal doping curve since doubling the initial concentration doubles the normalized fluence coordinate $(1 - \phi/\phi_c)$, i.e., if $p_o = 2\, p_o'$, then

$$p = \frac{p_o'}{2} \left[2\left(1 - \frac{\phi}{\phi_c}\right) + \sqrt{\left[2\left(1 - \frac{\phi}{\phi_c}\right)\right]^2 + \left(\frac{2n_i}{p_o'}\right)^2} \right] .$$

An expression for the resistivity as a function of fluence can be obtained from the expressions

$$\rho = \frac{1}{e(n\mu_n + p\mu_p)}$$

$$b = \mu_n/\mu_p$$

and

$$np = n_i^2$$

therefore,

$$\rho = \begin{cases} \dfrac{p}{e\mu_p\,(bn_i^{\,2} + p^2)}, & \text{p-type} \\[2ex] \dfrac{n}{e\mu_p(bn^2 + n_i^{\,2})}, & \text{n-type} \end{cases} \tag{13}$$

By substituting n or p as a function of fluence from Eqs. (11) and (12) the resistivity, ρ, can be obtained as a function of fluence. This expression is plotted in Figures (1) and (2) for typical p-type float zone material [the parameters are given on Figures (1) and (2) and differ from those on Figures (3) - (6)].

The sensitivity of resistivity to fluence should be noted near complete compensation. Furthermore, in the expanded scale in Figure 2, note the maximum resistivity occurs at a fluence below that necessary for 100% compensation. This is a result of the fact that the carrier mobilities are not equal. The intrinsic resistivity, ρ_i, is the resistivity obtained at exact compensation.

By differentiation of Eq. (13), it can be shown that

$$\rho_m = \frac{1}{2en_i\sqrt{\mu_n\mu_p}} \tag{14}$$

where ρ_m is the highest resistivity obtainable. Also, by using $\sigma = ne\mu_n + pe\mu_p$ and setting $d\sigma/dp = o$, one obtains the hole concentration $p_m = n_i\sqrt{\mu_n/\mu_p}$ corresponding to the maximum resistivity ρ_m.

It can be similarly shown that the fluence, ϕ_m, to obtain maximum resistivity, is related to the critical fluence to obtain 100% compensation by using Eq. (11) with $\phi = \phi_m$ and the expressions $p = p_m = n_i\sqrt{\mu_n/\mu_p}$ and $\phi_c = p_o/K$ to give the expression

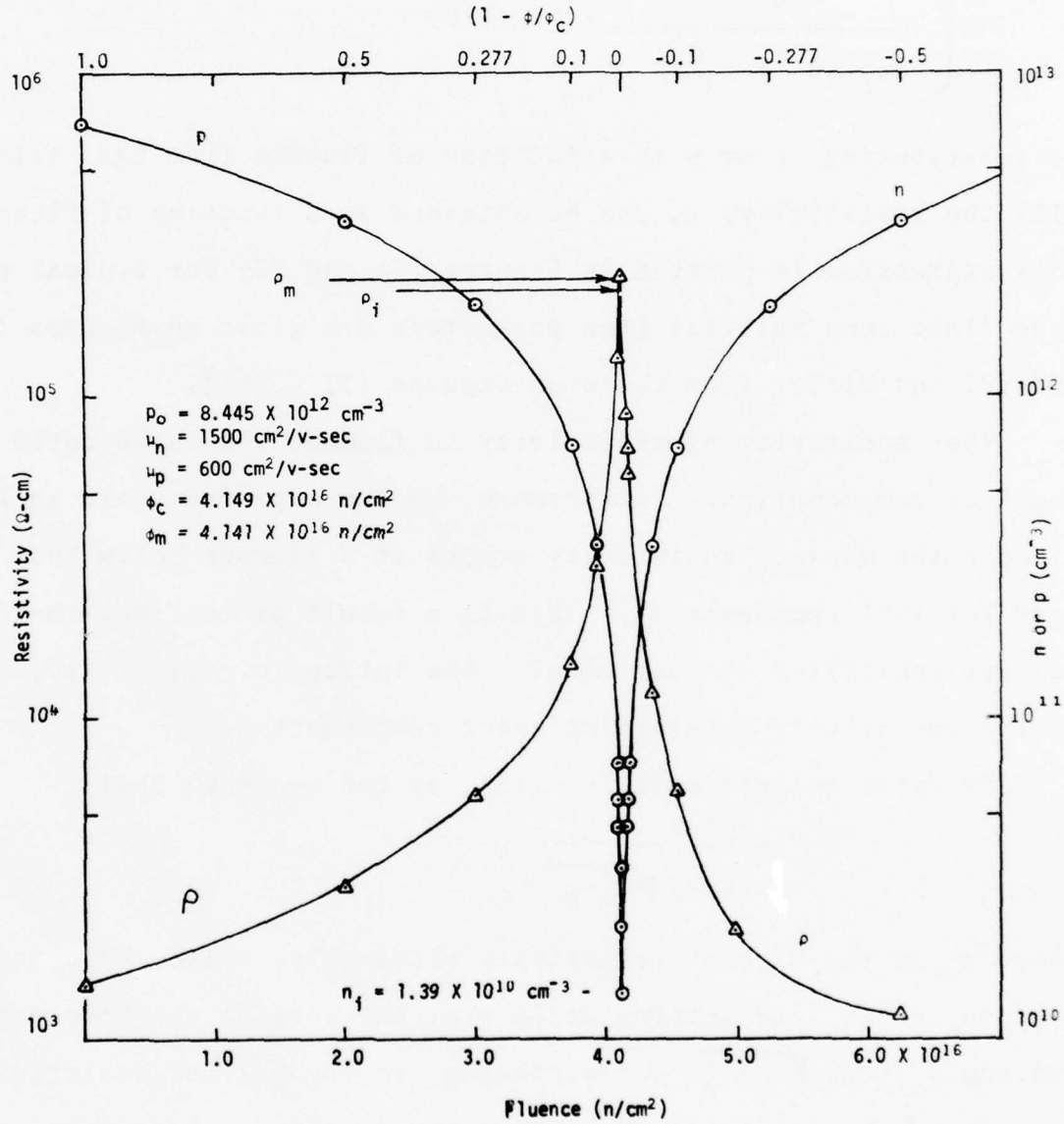

Figure 1. Resistivity and carrier concentration vs. fluence.

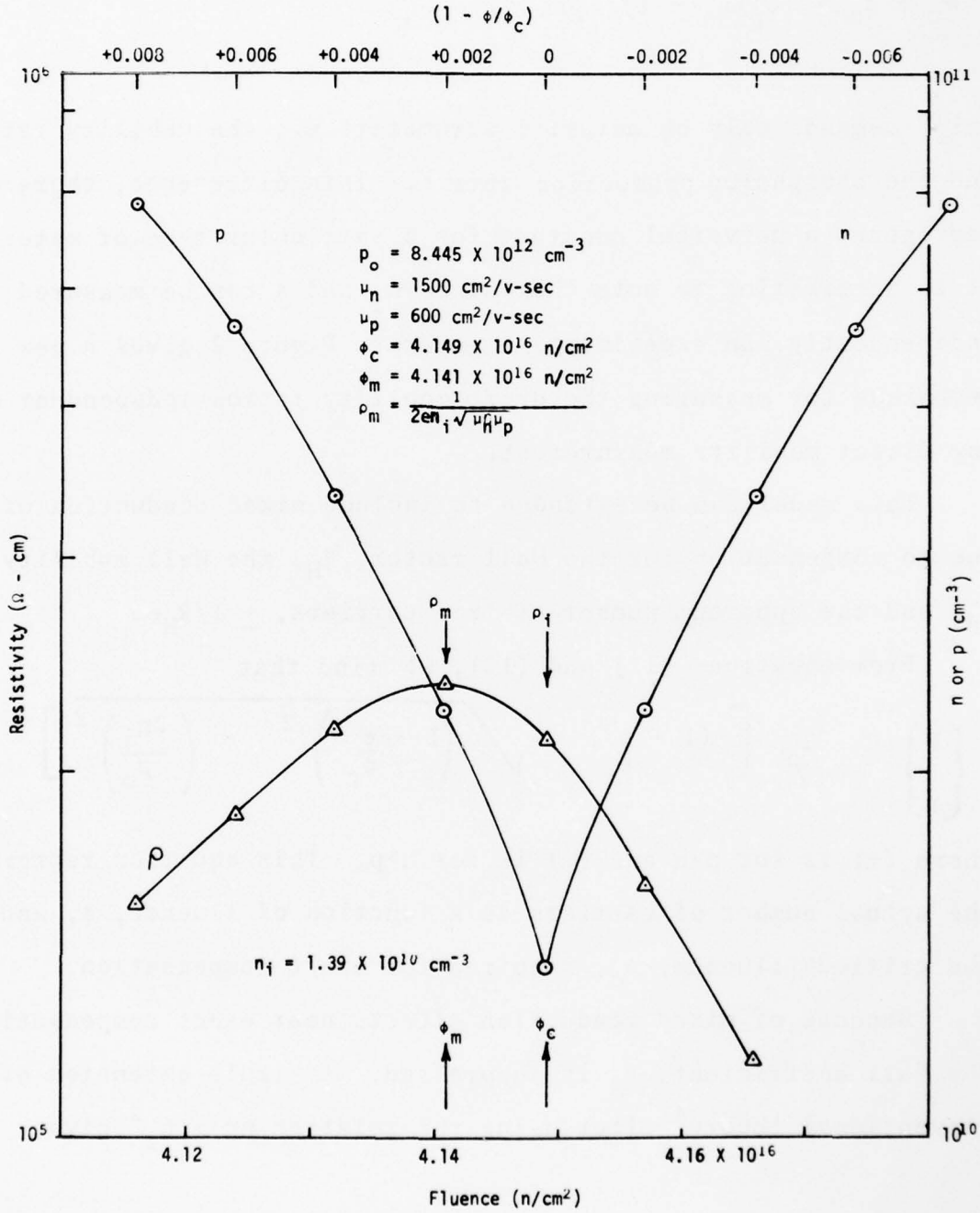

Figure 2. Expanded fluence scale plot of Figure 1.

$$\phi_c - \phi_m = (\mu_p/\mu_n - 1)(n_i/K)/\sqrt{\mu_n/\mu_p} \tag{15}$$

which depends only on material parameters n_i, the mobility ratio, and the phosphorus production rate K. This difference, therefore, represents a universal constant for a particular type of material. It is interesting to note that since n_i and K can be measured independently, an experiment to generate Figure 2 gives a new technique for measuring the drift mobility ratios independent of any direct mobility measurement.

This model can be extended to include mixed conduction effects due to compensation for the Hall factor, R_H, the Hall mobility, μ_H, and the apparent number of free carriers, $\pm 1/R_H e$.

From equations (11) and (12), we find that

$$\begin{Bmatrix} p \\ n \end{Bmatrix} = \frac{p_o}{2}\left[\pm\left(1 - \frac{\phi}{\phi_c}\right) + \sqrt{\left(1 - \frac{\phi}{\phi_c}\right)^2 + \left(\frac{2n_i}{p_o}\right)^2}\right] \tag{16}$$

where (+) is for p>n and (-) is for n>p. This equation represents the actual number of carriers as a function of fluence, ϕ, and the critical fluence, ϕ_c, required for exact compensation.

Because of mixed conduction effects near exact compensation, the Hall coefficient, R_H is suppressed. A simple extension of conventional theory[4] after using the relation $np = n_i^2$ gives

$$R_H = \begin{cases} \dfrac{p(p^2 - n_i^2 b^2)}{e\,(p^2 + n_i^2 b)^2}, & p>n \\[2ex] \dfrac{n(n_i^2 - n^2 b^2)}{e(n_i^2 + n^2 b)^2}, & n>p \end{cases} \tag{17}$$

where $b = \mu_n/\mu_p$ is the ratio of drift mobilities. Using the usual relation between Hall mobility and R_H,

$$\mu_H = \pm \frac{R_H}{\rho} \qquad \begin{cases} (+)\ R_H>o \\ (-)\ R_H<o \end{cases}$$

and equation (13),

$$\rho = \begin{cases} \dfrac{p}{e\mu_p(bn_i^2 + p^2)} & \text{for } R_H>o \\[2ex] \dfrac{n}{e\mu_p(bn^2 + n_i^2)} = \dfrac{bn}{\mu_n e(bn^2 + n_i^2)} & \text{for } R_H<o, \end{cases} \tag{13}$$

we obtain

$$\mu_H = \begin{cases} \dfrac{\mu_p(p^2 - n_i^2 b^2)}{(p^2 + n_i^2 b)} & \text{for } R_H>o \\[2ex] \dfrac{\mu_n(n^2 b^2 - n_i^2)}{b(n^2 b + n_i^2)} & \text{and for } R_H<o. \end{cases} \tag{18}$$

Note that near complete compensation, the Hall mobility is considerably suppressed as $p \to n_i b$ or $n \to n_i/b$.

The apparent free carrier concentration obtained from the

Hall coefficient is, near compensation, larger than the actual carrier concentration since

$$p_H = \frac{1}{R_H e} = \frac{(p^2 + n_i^2 b)^2}{p(p^2 - n_i^2 b^2}$$

$$n_H = -\frac{1}{R_H e} = \frac{(n^2 b + n_i^2)^2}{n(n^2 b^2 - n_i^2)} \quad . \tag{19}$$

These equations are now in a form from which μ_H, R_H, and n_H or p_H can be obtained as a function of fluence by direct substitution of Eq. (16) into Eqs. (17), (18), and (19). Programs have been written to generate these variables as a function of fluence. Data calculated from the code is shown for a typical case [p_o and ϕ_c different than for Figs. (1) and (2)] in Figs. (3), (4), (5), and (6).

Note that as $p \to n_i b$; $R_H \to o$, $\mu_H \to o$, $p_H \to \infty$. This is not the same condition as obtained for the resistivity which reaches a maximum at $p = b^{\frac{1}{2}} n_i$.

Although the above equations relate the measurable room temperature electrical properties, ρ, μ_H, n_H, and p_H to the fluence, ϕ, no direct information is obtained from room temperature electrical measurements on the ratio of boron concentration to phosphorus concentration. We have shown that the free carrier concentration can be compensated in principle to any degree of precision, however, additional information from low temperature measurements is required to determine if the desired ratio of boron to phosphorus has been obtained. The question remains, given a particular value of irradiation fluence ratio, ϕ/ϕ_c,

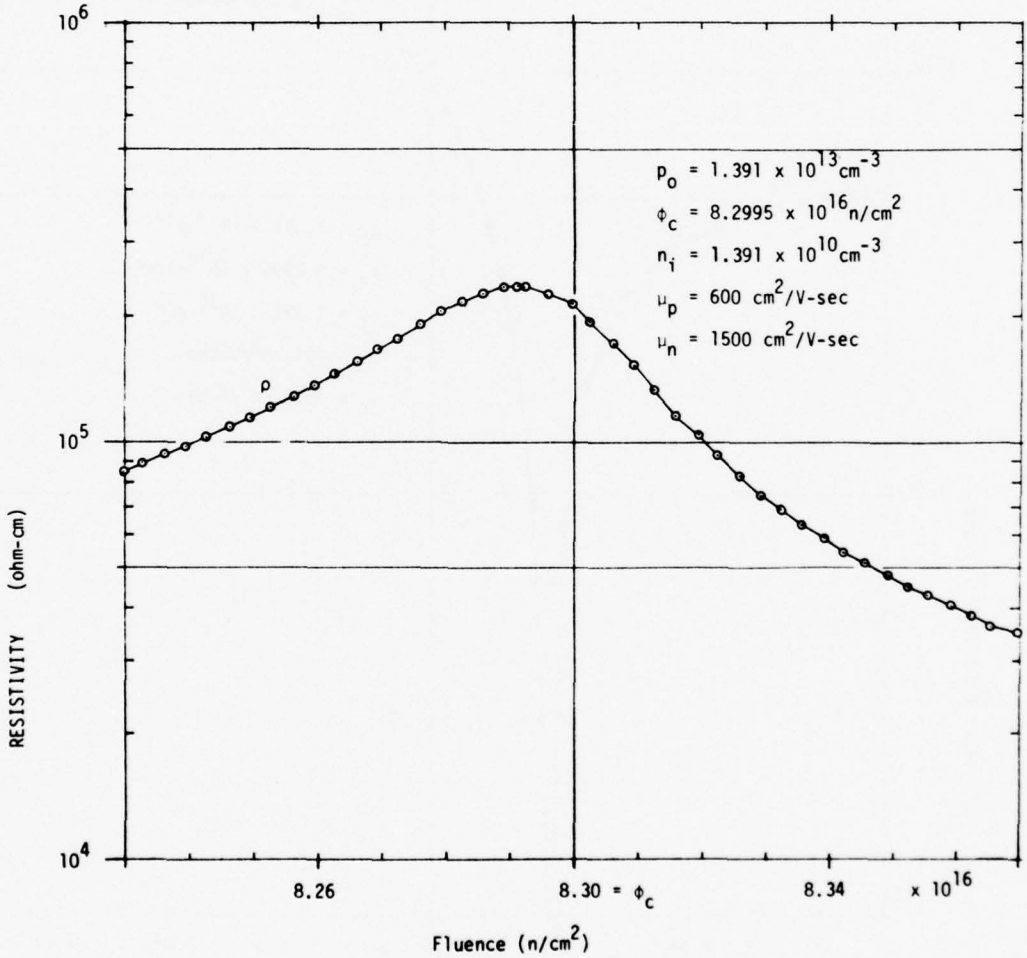

Figure 3. Resistivity vs. fluence.

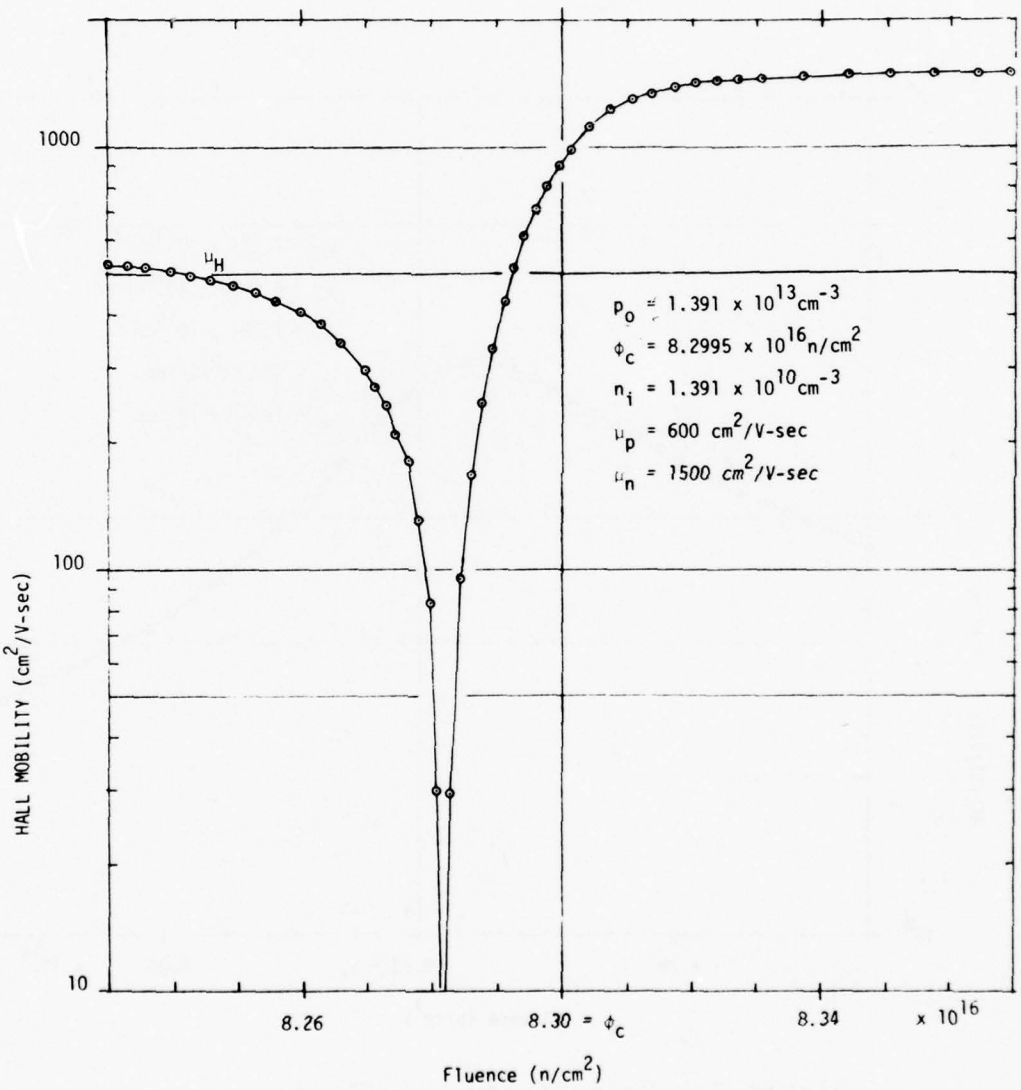

Figure 4. Hall mobility vs. fluence.

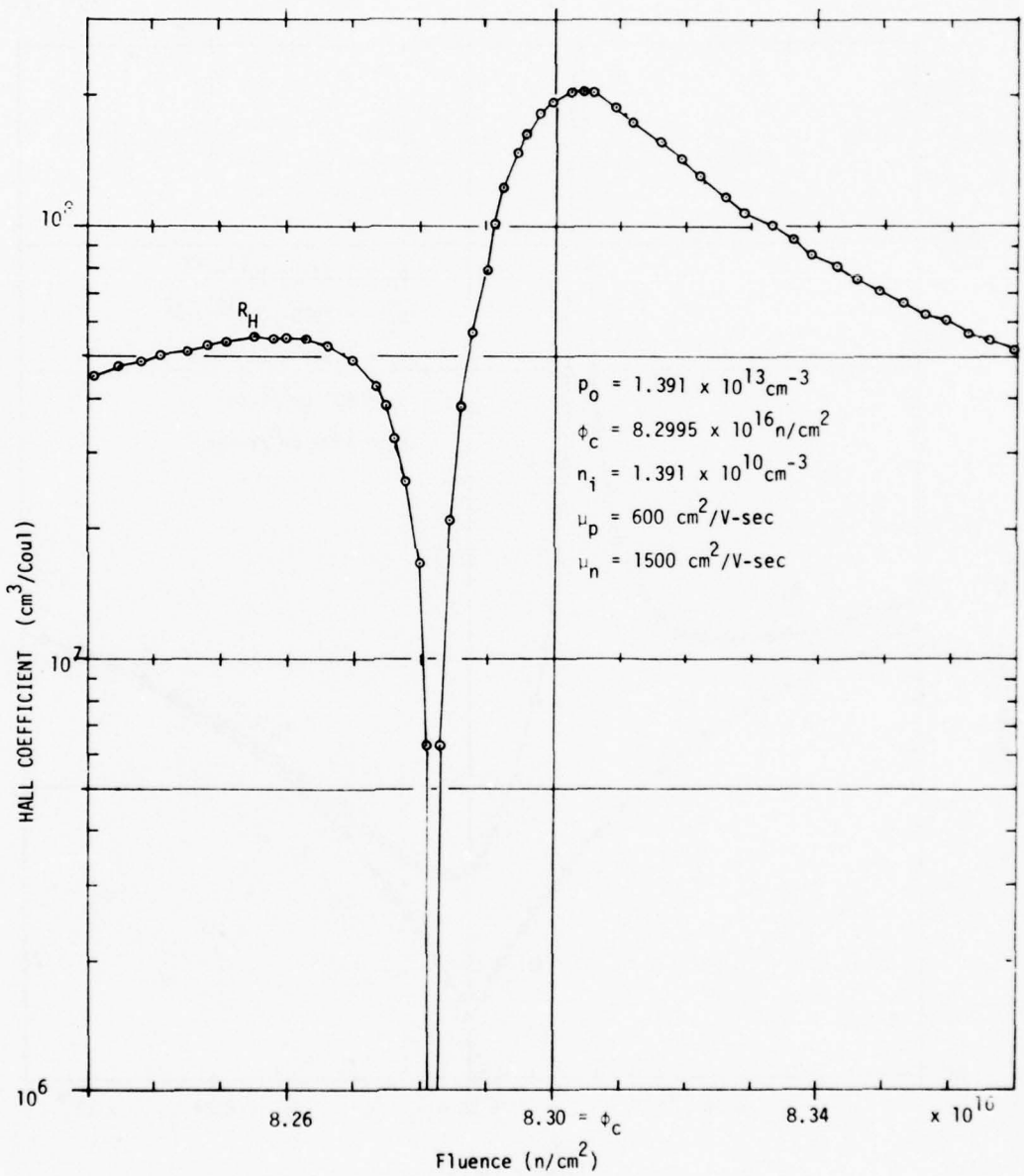

Figure 5. Hall coefficient vs. fluence.

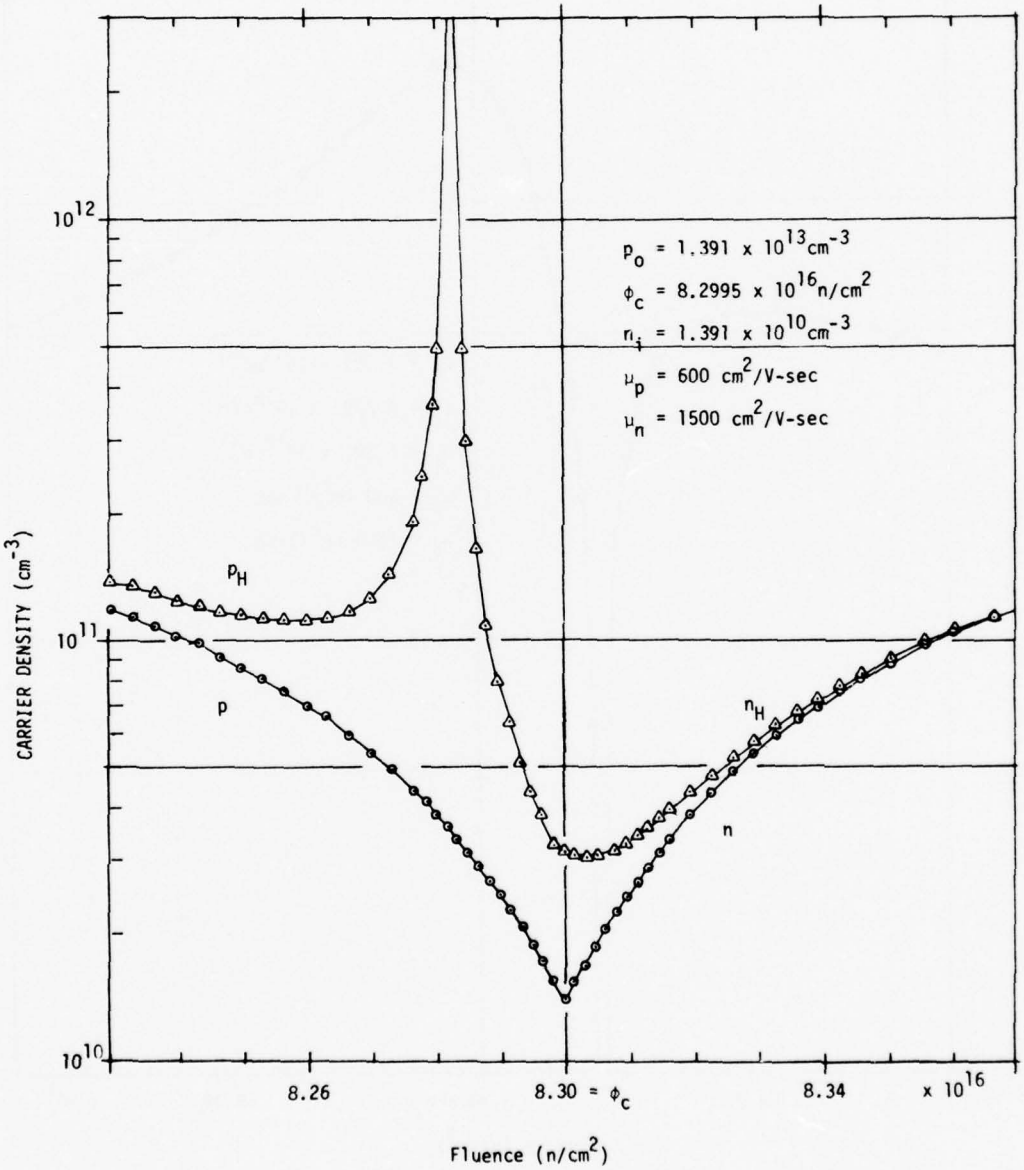

Figure 6. Actual carrier concentration, p, n, and Hall coefficient carrier concentration p_H, n_H, vs. fluence.

how closely does this ratio represent the boron to phosphorus ratio? The answer is easily obtained. The conclusion from the analysis to be presented is that ϕ/ϕ_c is exactly equal to the compensation ratio only at exact compensation, or when $\phi = \phi_c$. For other fluences, this ratio is not exactly equal to the compensation ratio but is a good approximation for all practical cases of interest. To demonstrate this, we will consider two cases, the case of undercompensation and the case of overcompensation.

Case I: Overcompensation, $\phi > \phi_c$, p-type to n-type

The initial compensation ratio in the p-type material before irradiation is defined conventionally as

$$k_o = N_{D_o}/N_A$$

while after irradiation, the compensation ratio is defined conventionally as

$$k_f = N_A/N_{D_f} \quad .$$

Since for all starting material available that has been adequately zone refined, $p_o >> n_i$,

$$p_o = N_A - N_{D_o} = K\phi_c$$

where again, K is the production rate of donors by the transmutation process. Also

$$N_{D_f} = N_{D_o} + K\phi,$$

therefore, the final compensation ratio is given by

$$k_f = \frac{N_A}{N_{D_f}} = \frac{N_{D_o} + K\phi_c}{N_{D_o} + K\phi} .$$

By rearrangement and using the relation $K\phi_c = N_A - N_{D_o}$ it can shown that

$$k_f = \frac{(N_A/N_{D_o} - 1)^{-1}}{(N_A/N_{D_o} - 1)^{-1} + (\phi/\phi_c)}$$

and, using the definition of k_o,

$$k_f = \frac{\left(k_o^{-1} - 1\right)^{-1} + 1}{\left(k_o^{-1} - 1\right)^{-1} + \frac{\phi}{\phi_c}} .$$

From the above equation, we find that

$$k_f^{-1} = k_o + \frac{\phi}{\phi_c}(1-k_o), \quad \phi \geqslant \phi_c. \tag{20}$$

Note that when $\phi = \phi_c$, $k_f \approx 1$. Exact compensation can be determined without an explicit knowledge of the starting material compensation ratio, k_o, if the initial carrier conceptration, p_o, and the phosphorus production rate, K, are known. In general,

$$k_f^{-1} = N_{D_f}/N_A \neq \phi/\phi_c.$$

Case II: Undercompensation, $\phi < \phi_c$, p-type to p-type

In this case, the initial and final compensation ratios are defined conventionally by the expressions

$$k_f = N_{D_F}/N_A, \quad k_o = N_{D_o}/N_A .$$

Therefore,

$$k_f = \frac{N_{D_o} + K\phi}{N_{D_o} + K\phi_c}$$

and by an analysis similar to Case I, we obtain

$$k_f = k_o + (1 - k_o)\ \phi/\phi_c; \quad \phi_c \geq \phi \ . \tag{21}$$

Again, we find that for $\phi = \phi_c$, $k_f = 1$ but for other ratios of ϕ/ϕ_c, $k_f \neq \phi/\phi_c$.

The results of Eqs. (20) and (21) are represented graphically in Figure 7. In this figure, the final ratio of phosphorus to boron concentrations, N_{D_f}/N_A, is plotted as a function of the starting material compensation ratio, N_{D_o}/N_A, for different fluence ratios ϕ/ϕ_c. It is seen that for initial compensation ratios less than a few percent

$$\frac{\phi}{\phi_c} \simeq \frac{N_{D_f}}{N_A} \tag{22}$$

to a very good approximation. Starting compensation ratios of this order of magnitude should exist for multipass zone refined Si because of the differences in segregation coefficients for boron and phosphorus. Even when the initial compensation ratio is as high as 20%, the error in estimating the final compensation ratio using Eq. (22) is no more than 20% for $\phi/\phi_c \leq 2$, an overcompensation of up to 100%. Estimates of the compensation ratio by any known experimental technique, including low temperature electrical measurements are not likely to exceed, for the low impurity concentrations with which we are here dealing, the accuracy which can be obtained from simple room temperature electrical measurements coupled with information about the number of zone passes.

It should be noted in concluding this section that the fluctuations in carrier concentration have not been taken into account in the previous equations. This will be discussed further

UNDERCOMPENSATION: $\Phi/\Phi_c < 1$

$$k_{f_{un}} = \frac{N_{D_f}}{N_A} = k_o + (1 - k_o)\ \Phi/\Phi_c$$

OVERCOMPENSATION: $\Phi/\Phi_c > 1$

$$k_{f_{ov}} = \frac{N_A}{N_{D_f}} = k_{f_{un}}^{-1}$$

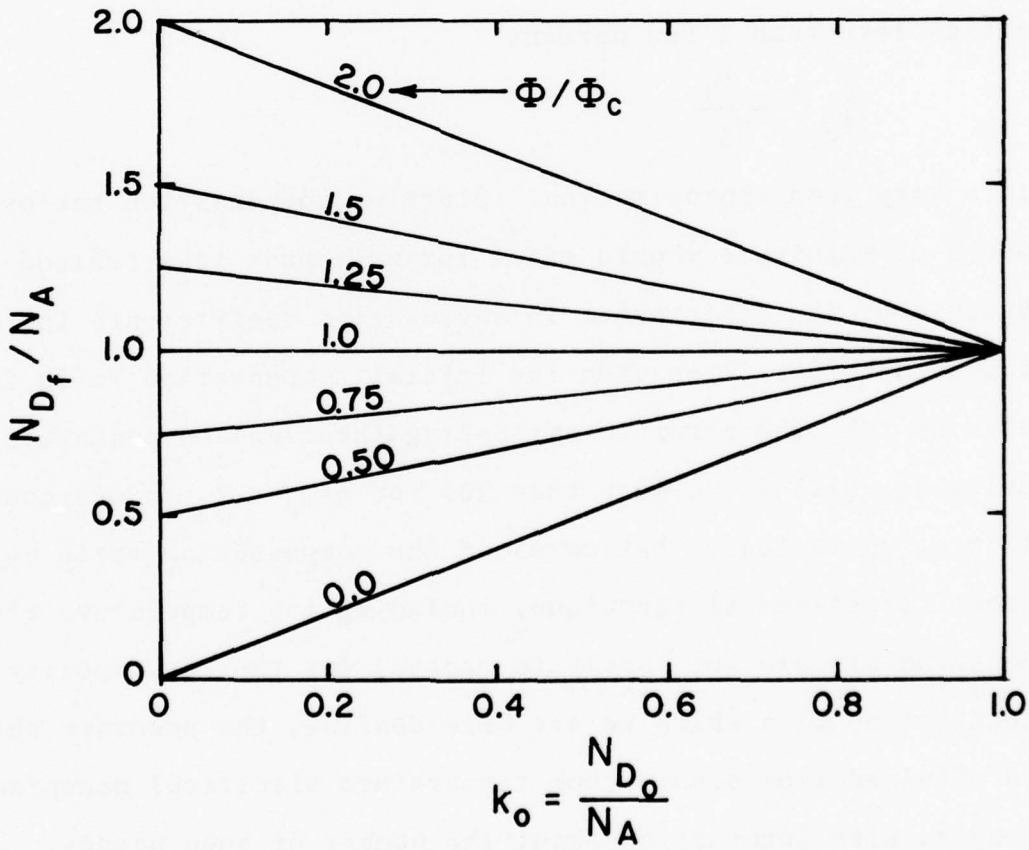

Figure 7. Final compensation ratio as a function of initial compensation ratio for various fluence ratios, ϕ/ϕ_c.

in a later section. The equations presented in this section are exact; however, they can only apply to local concentrations in the wafer, not averages. This is illustrated by considering, for example, our definition of critical fluence, ϕ_c. Since the initial carrier concentration, p_o, is a function of position on the wafer,

$$p_o = p_o(x, y),$$

and, from our previous definition, $\phi_c = p_o/K$,

$$\phi_c = \phi_c\ (x, y).$$

We are faced with the perplexing problem that different parts of the wafer require different fluences to reach exact compensation! If we irradiate so as to compensate the average concentration exactly, parts of the wafer will be undercompensated and other parts will be overcompensated. Under such circumstances, the definition of exact compensation fluence, ϕ_c, must be the subject of considerable investigation. We have, indeed, identified at least a half dozen possible definitions for the critical fluence. All of these critical fluences differ slightly; however, it can be shown that most fall within $\pm$ 0.5% of each other for typical starting material fluctuations.

To illustrate some of the problems involved, we make the hyphothesis that we can use average values for the electrical measurements to determine ϕ_c. Then

$$\phi_c = \frac{\overline{p_o}}{K} \qquad \text{for } \overline{p_o} >> n_i$$

or, in terms of average resistivity,

$$\phi_c = \frac{1}{K} \frac{K_p}{\bar{\rho}_o} \quad . \tag{23}$$

But it can easily be shown that these two quantities are not equal for a working definition of $\bar{p}_o$ and $\bar{\rho}_o$ given by

$$\bar{p}_o = \frac{p_{o\ max} + p_{o\ min}}{2}$$

and

$$\bar{\rho}_o = \frac{\rho_{o\ max} + \rho_{o\ min}}{2} \quad .$$

Since $p_o = K_p/\rho_o$, then

$$\bar{p}_o = \frac{K_p}{2} \left(\frac{1}{\rho_{o\ max}} + \frac{1}{\rho_{o\ min}}\right)$$

$$= K_p \frac{\bar{\rho}_o}{\rho_{o\ max}\ \rho_{o\ min}} \neq \frac{K_p}{\bar{\rho}_o} \quad .$$

It can be shown with some difficulty that the error introduced by using equation (23) to define ϕ_c compared to a different definition for the critical fluence, ϕ_c', which produces equal numbers of carrier fluctuations on either side of intrinsic can be estimated by the relation

$$\frac{\phi_c'}{\phi_c} = \frac{1}{4} \left[\frac{\rho_{o\ max}}{\rho_{o\ min}} + \frac{\rho_{o\ min}}{\rho_{o\ max}}\right] + 1.$$

Based on the minimum and maximum resistivity values for samples VZ-083, we find that

$$\frac{\phi_c'}{\phi_c} = 1.0025.$$

A total fluence error of about 0.25% is, therefore, introduced by

using Eq. (23) and the above definition for average resistivity.

The definition of $\bar{\rho}$ given above is also suspect since the true average (which may or may not be equal to estimates made from 4-point probe data in a particular experiment) is

$$\overline{\rho(x, y)} = A^{-1} \iint \rho(x, y)\, dxdy$$

where $A = \iint dxdy$. The previous definition for $\bar{\rho}$,

$$\bar{\rho} = \frac{\rho_{max} + \rho_{min}}{2}$$

assumes implicitly a symmetrical distribution of data points about the mean. Since resistivity is not directly proportional to carrier concentration, and since fluctuations in carrier concentration depend on pull rate, rotation rate and temperature fluctuations during growth, it is very unlikely that the simple definition for $\bar{\rho}$ used above will hold exactly. We can, however, be reasonably encouraged from the estimate of critical fluence error introduced by these approximations. It is important, however, to maintain a certain degree of caution when working in the regime of exact compensation, a regime accessible for the first time only by transmutation doping.

III. EXPERIMENTAL TECHNIQUES AND APPARATUS

In this section, a description of the apparatus and techniques required to irradiate the Si and to evaluate the material before and after irradiation is described.

A. Reactor Description

The reactor at the University of Missouri is a high flux, light water moderated research reactor designed to operate

on highly enriched fuel. It has a beryllium reflector, a graphite moderator and forced cooling system for pool and core. The reactor is operated at a power level of 10 MW. The reactor runs routinely at 10 MW for 120 hours per week, 52 weeks per year. A comparison of the peak flux of the MURR reactor with other research reactors in the United States is shown in Figure 8.

A cross-sectional view of the reactor core and various experimental stations is shown in Figure 9. One of the major advantages of the MURR reactor for Si irradiation is the easy access to the sample positions in the pool and reflector.

At present, two 2" dia. x 30" long silicon sample irradiation positions with sample rotators are located in the graphite reflector in positions I-2 and H-2 in Figure 9. The average flux at these positions is about $3 \times 10^{13} n/cm^2/sec$. The pneumatic tubes used for activation analysis rapid sampling handling are also shown in Figure 9.

Beyond the graphite positions is the S-basket with seven 3" dia. Si holes which can be rotated manually or mechanically. The flux in the S-basket varies from $10^{13} n/cm^2/sec$ to $10^{12} n/cm^2/sec$.

For the very low fluences required for the exact compensation of detector Si, a variable flux pool facility was developed and constructed. The samples in this position are also mechanically rotated. The flux in this facility is a

SOME RESEARCH REACTORS IN THE UNITED STATES

#	REACTOR	LOCATION	POWER (MW)	PEAK FLUX (n/cm^2-sec $\times 10^{14}$)	NO. BEAM TUBES	PEAK BEAM SOURCE FLUX (n/cm^2-sec $\times 10^{14}$)
1	ILL*	Grenoble	57	120	25+	12
2	HFIR	ORNL	100	50	4+	9
3	HFBR	BNL	40	56	9	6
4	MURR	Columbia, Mo.	10	7	7+1	1.2
5	GETR	Pleasanton, Calif.	50	4	(1)	1.0
6	NBSR	NBS	10	2	13	0.9
7	MITR	Boston, Mass.	5	2.2	11	0.8
8	ORR	ORNL	30	4	6	0.8
9	GTRR	Atlanta, Ga.	5	1	10	0.7
10	CP-5	ANL	5	2	8	0.3
11	ALRR	AMES	5	1.2	9	0.3
12	Mich.	Ann Arbor, Mich.	2	0.2	10	0.3
13	RIR	Rhode Island	2	0.2		0.2

*added for comparison

Figure 8. Comparison of research reactor peak flux values in the United States.

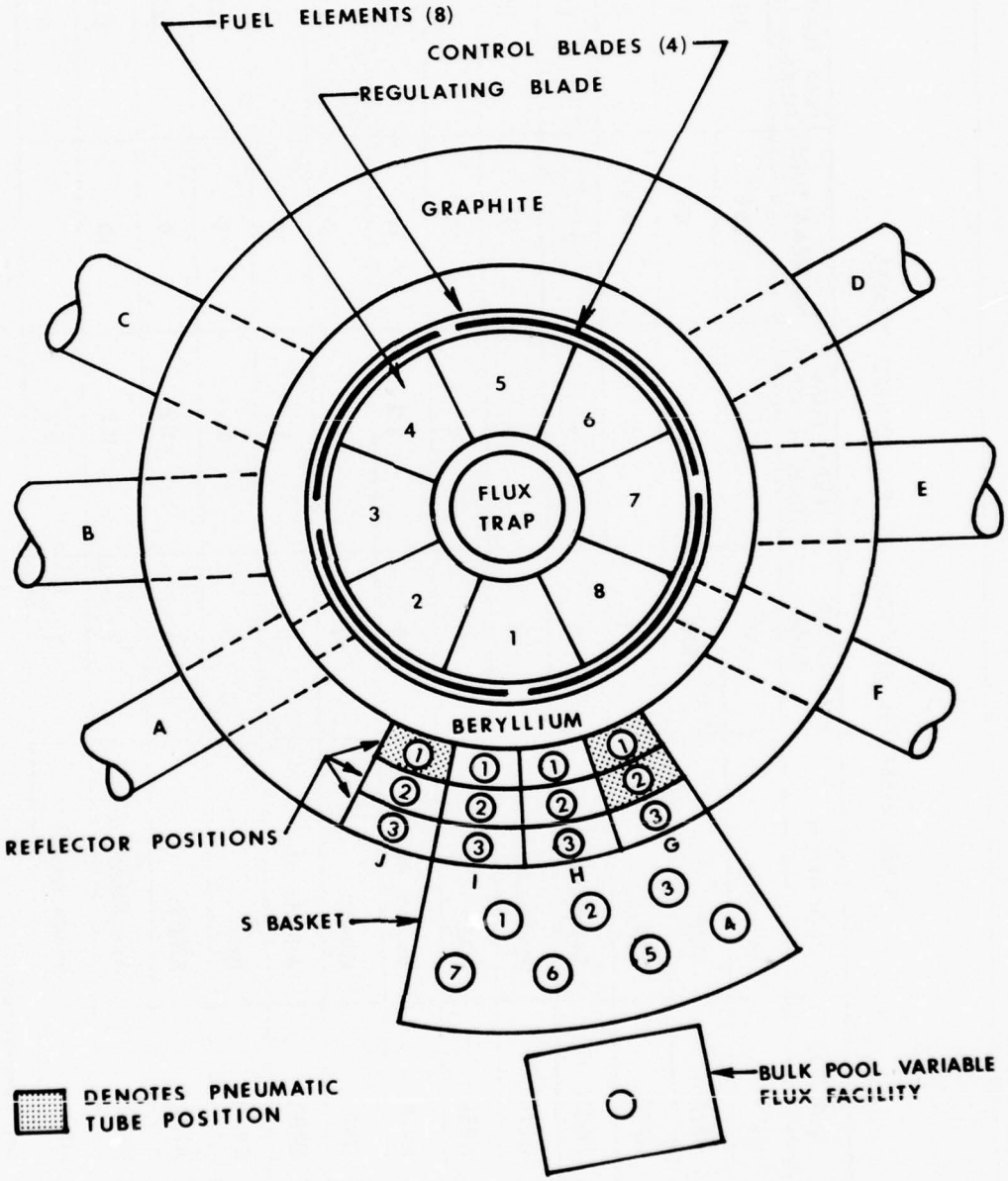

Figure 9. Flux trap, beamports, reflector and bulk pool facilities.

maximum in the present close-in position and is about $7 \times 10^{11} n/cm^2/sec$. This flux can be reduced considerably by moving the facility further out in the pool. The approximate position of the bulk pool Si facility is shown in Figure 9.

A typical flux profile for the I-2 position is shown in Figure 10. Silicon ingots up to 10" length are positioned in the linear portion of this flux and flipped end for end at precisely 50% of the total fluence. The flux profiles in other positions are approximately the same shape but tend to flatten at the peak at positions further from the core. In the variable flux facility, the peak is sufficiently flat to make the peak of the flux profile useful over a 5" length.

B. Bulk Pool Variable Flux Irradiation Facility

A calculation of the fluence required to compensate a typical residual boron concentration of about 3×10^{12} atoms/cm^3 yields a fluence of 1 to $2 \times 10^{16} n/cm^2$. A typical loading or unloading time of five minutes and a fluence accuracy of $\pm$ 0.5% restricts the irradiation flux to a value between 1×10^{11} to $1 \times 10^{12} n/cm^2/sec$. Since this flux is an order of magnitude lower then that obtained in the S-Basket, a special irradiation facility was constructed for this project. The general location of this "Bulk Pool Variable Flux Facility" is shown in Figure 9.

Figure 11 shows the construction details of the movable box

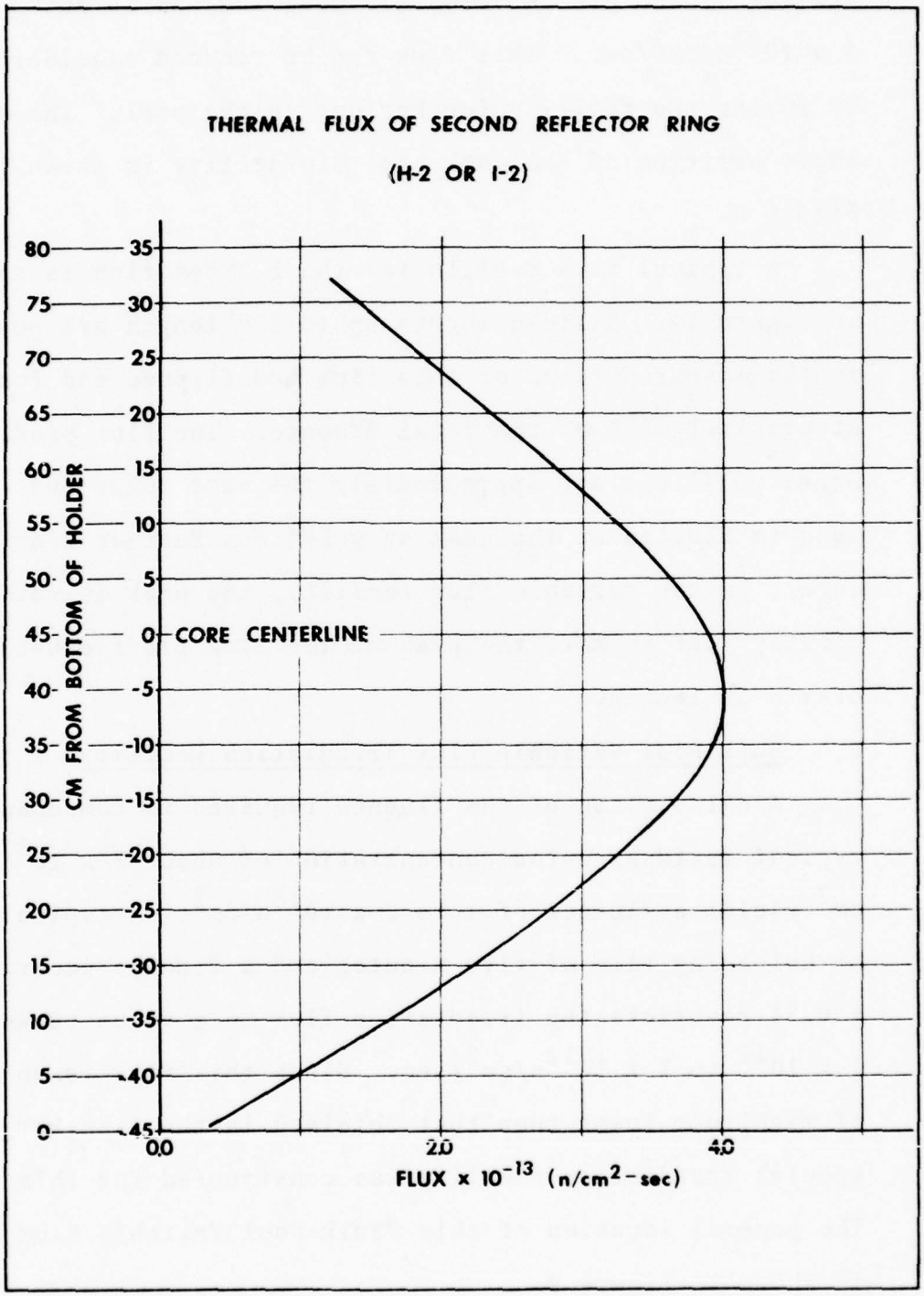

Figure 10. Thermal neutron flux profiles in I-2 reflector position.

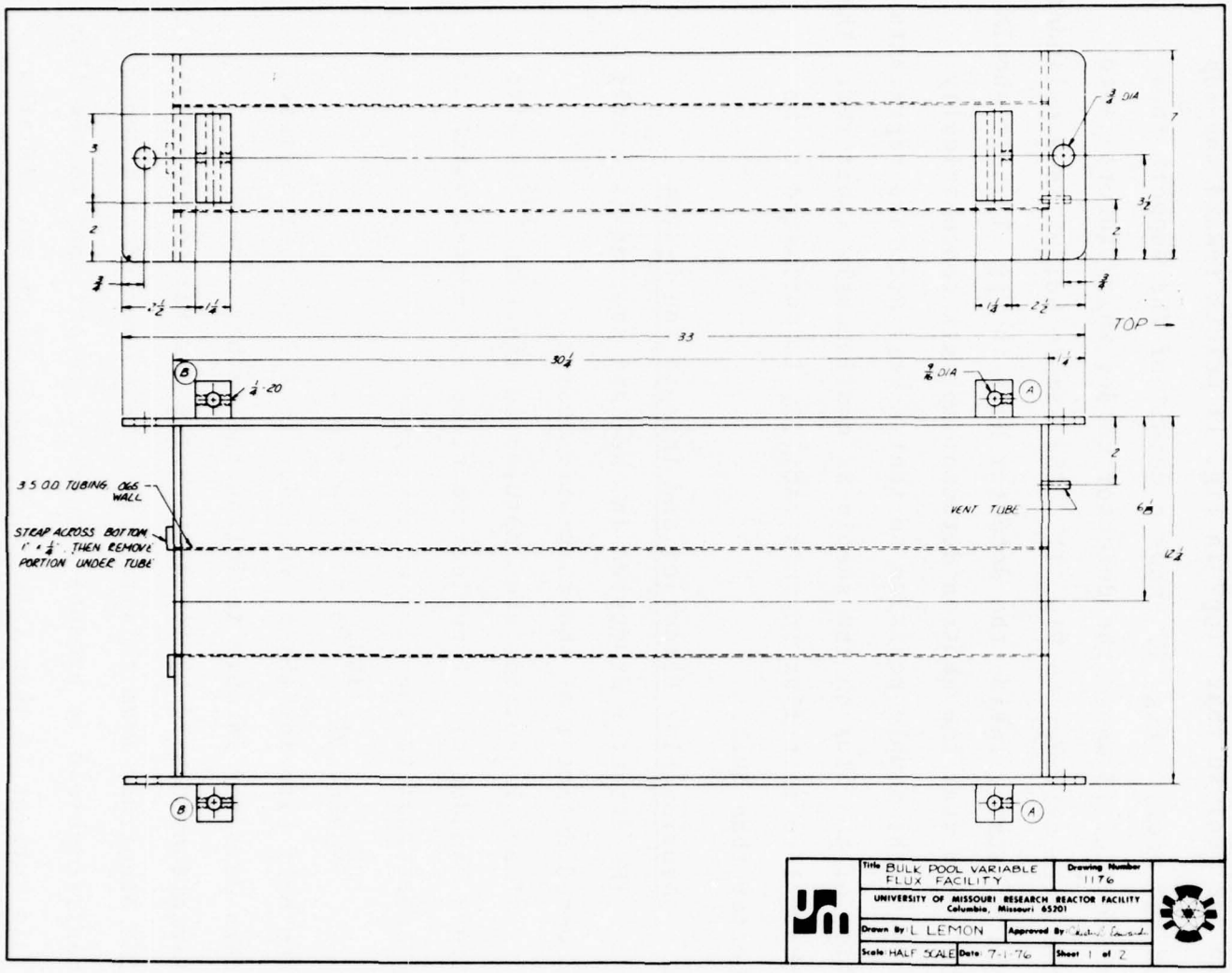

Figure 11. Movable box detail for bulk pool irradiation facility.

which is held onto the S-Basket by two rigid rods which pass through holes A. (The sample holding tube is oriented in the pool so that "Top" in Fig. 11 points toward the top of the pool). Fig. 12 shows a detail of the support rods while Fig. 13 shows the detector holder which inserts into the main cylinder in Fig. 11. The sample holder is a cylinder which rotates inside the detector hole in Fig. 13. It should be noted that the neutron detector spirals concentrically around the sample position so that a very accurate representation of the flux on the sample is continuously monitored. The thermal to fast flux in this facility is estimated to be better than 30:1.

C. Neutron Flux Detection and Integration System

The detector discussed in the last section is a self powered detector of the thin wire design.

Thermal neutrons are captured in the thin ^{103}Rh wire (100% abundance). A nuclear reaction is induced which is proportional to the flux of the type

$$^{103}Rh(n, \gamma)\ ^{104}Rh \rightarrow {}^{104}Pd + \beta^{-}.$$

The half life for the β^{-} emission is 4.2 sec., therefore, this detector is able to follow the rather slow flux variations caused by movement of the reactor control rods. The electrons from this reaction are collected on a concentric shield to produce a current proportional to the flux. This current is then integrated and an alarm set off at a predetermined preset.

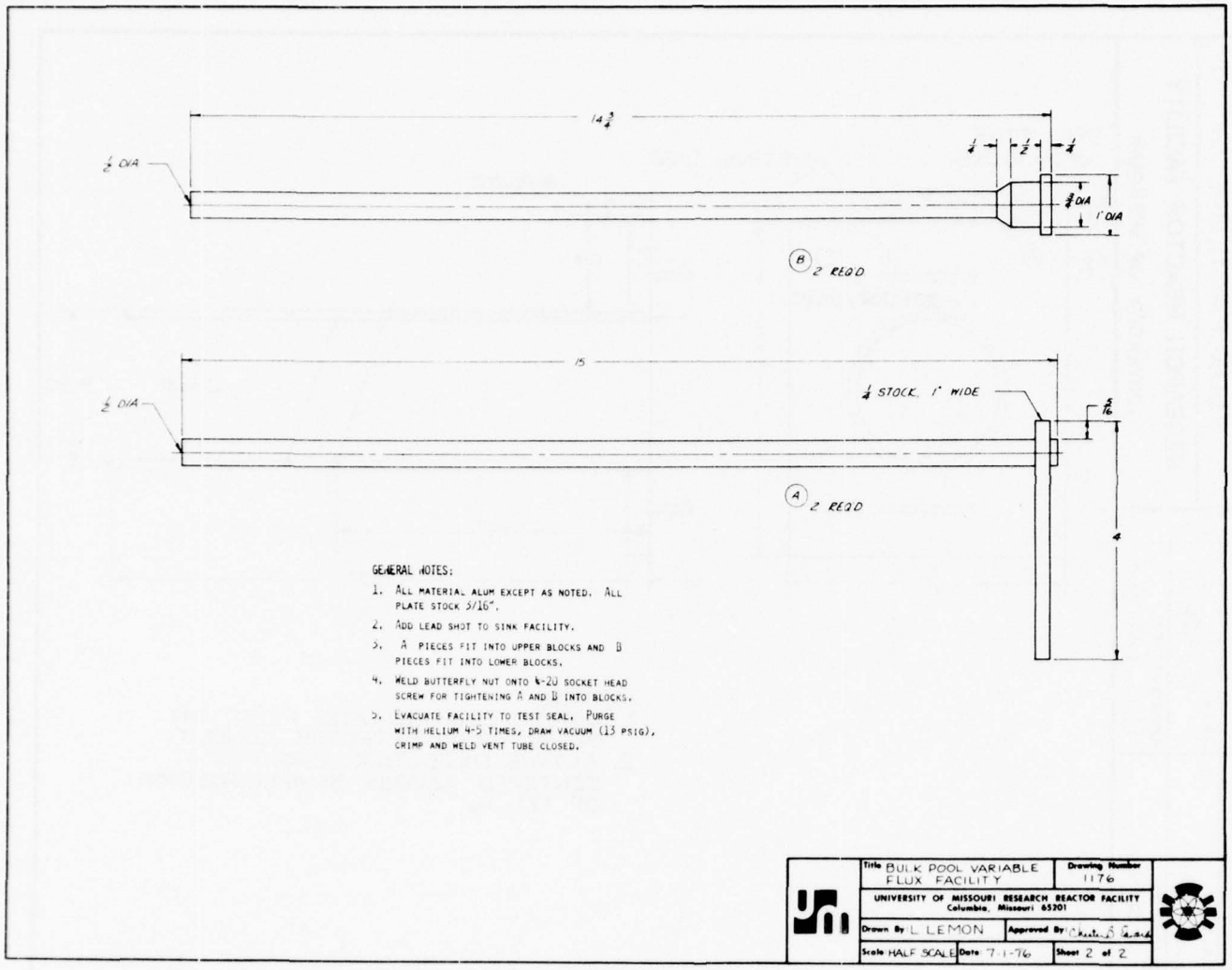

Figure 12. Support rods for variable flux facility.

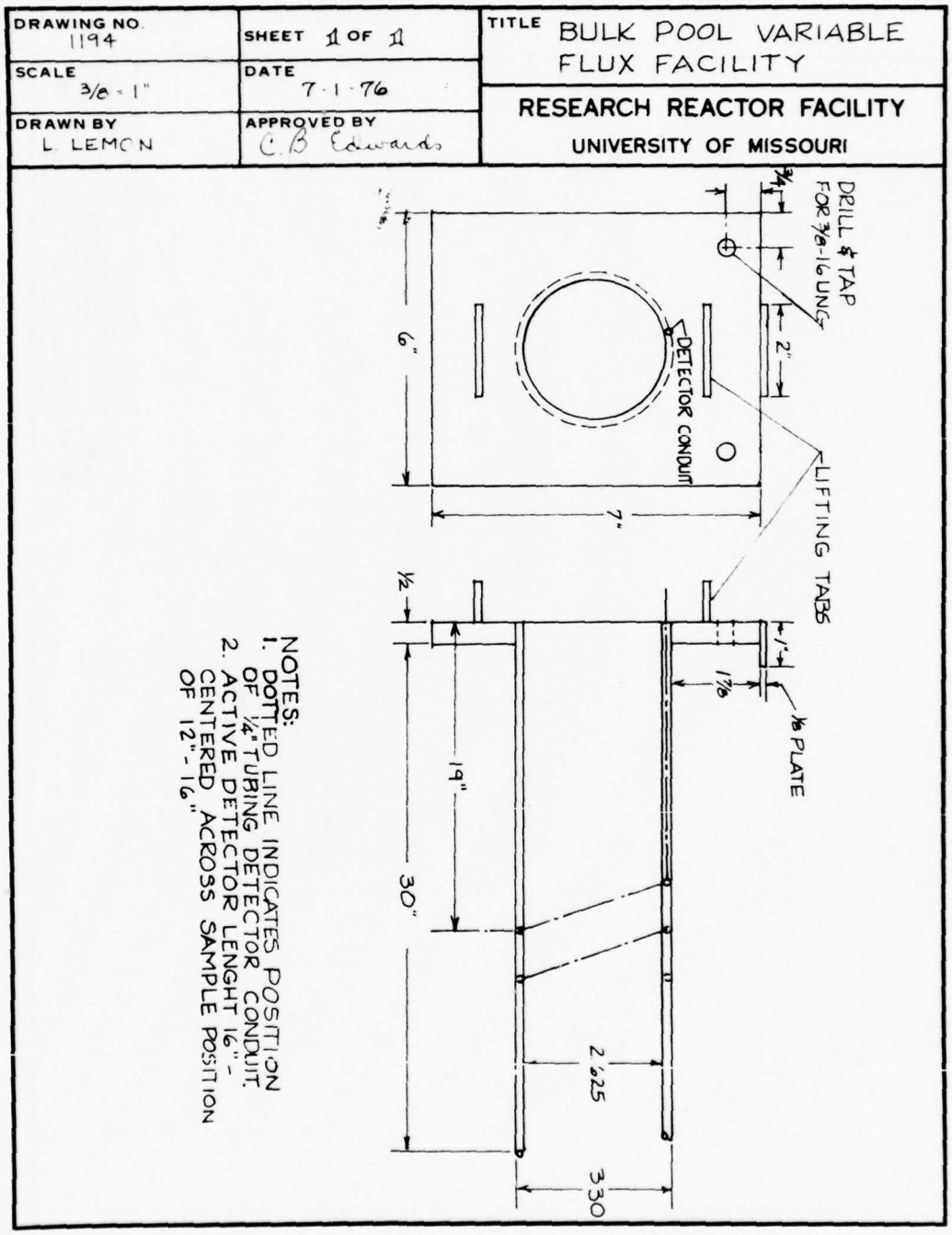

Figure 13. Detector holder for variable flux facility.

Considerable effort has been spent calibrating this system. Flux wires of Co doped Al have been used to measure the flux by the radioactivity generated by a given fluence and compared to the observed counts from the integrator system. Two types of flux wire have been used, N.B.S. and Cohn. Although considerable variation due to flux wire counting statistics and Co concentration are observed, the running mean of the two sets of flux wires agree to an accuracy approaching that of the integration system accuracy ($\pm$0.2%). This is illustrated in Table 4.

TABLE 4. Integrator System Calibration Data.

Irrad. #	Wire	Fluence/Count (n/cm^2/count)	%Deviation from Last Mean	Running Mean
	Cohn			
4	33-34	1.557×10^{12}	- 0.128%	1.557×10^{12}
8	33-34	1.610	+ 3.27	1.594
9	33-34	1.568	+ 0.577	1.578
11	33-34B	1.549	- 0.641	1.576
12	33-34	1.511	- 3.079	1.559
5	NBS	1.553×10^{12}	- 0.830%	1.553×10^{12}
8	NBS	1.482	- 5.364	1.518
11	NBS	1.664	+ 6.258	1.566

$$100 \times \frac{\overline{NBS} - \overline{Cohn}}{(\overline{NBS} + \overline{Cohn})/2} = -0.449\%$$

We believe we have demonstrated that the fluence as determined by the integration system is accurately known and reproducible to about $\pm$0.5%.

D. Neutron Activation Analysis Systems

Existing neutron activation analysis (NAA) facilities were employed for measuring elemental impurities in the silicon ingot starting materials. Two NAA irradiation facilities are available: a pneumatic tube transfer system into a neutron flux of about $8 \times 10^{13} n/cm^2/sec$ which permits the measurement of relatively short-lived activation products; and an outer reflector position at approximately $1 \times 10^{14} n/cm^2/sec$ for long term irradiations. The gamma-ray spectroscopy instrumentation consists of a lead shielded 50 cc, high resolution Ge(Li) detector coupled to a 4096 channel MCA with computer compatible magnetic tape output. An I.B.M. 370 computer is used for data reduction. These facilities provide "state of the art" capability and reliability for neutron activation analysis of trace element impurities in silicon.

E. Four-point and Thermal-Probes

As discussed in Section II, considerable information can be obtained about the nature of the compensation process by measuring resistivity and majority carrier type after typical majority carrier mobility is established for the ingot or wafer.

Thermal probe measurements of majority carrier type are made in a conventional manner using a variable temperature soldering pencil tip for the hot probe and a steel tip cold probe. The temperature gradient generated signal is fed

into a Keithley Model 602 electrometer[5] operated in the center zero current measuring mode usually on a range of 10^{-8} to 10^{-7}A. The hot probe is connected to the electrometer low while the cold probe is connected to the high so that a positive deflection denotes p-type and a negative deflection denotes n-type. The type of the unknown sample is also compared with two standard samples obtained from a multipass zone refined ingot (p-type) and a neutron transmuted and annealed sample (n-type). Agreement of the thermal-probe with Hall effect measurements has been excellent up to resistivities approaching 100,000 Ω-cm once experience is gained with the standard samples. Beyond this resistivity, mixed typing is often encountered suggesting that nonuniform doping is observed before the disappearance of the thermoprobe signal is observed.

Several four-point probe heads of different probe spacing and probe pressure have been tried with excellent results in resistivity ranges usually inaccessible to four-point probe measurement. The system consists of a Keithley Model 225 constant current source[5], a Hewlett Packard Model 3465A digital multimeter[6], and an Alessi Industries ATP-1 Test Probe Fixture[7] which has been modified to have a 12" vertical travel and a sample translation stage. Two types of four-point probe heads have been tried, an Alessi Model A4P-25 with a probe spacing of 0.025", a probe load of 70-180 gm; and a Signatone[8] probe with a spacing of 0.065", a

tip radius of 0.1 mil and a probe load of 180 gms. Both probe heads have tungsten carbide tips. Although both probe heads work well, the larger probe spacing is more forgiving in current selection and care of measurement and has been used except for very small samples where edge effects become a problem. The usual probe correction factors have been applied to obtain the resistivity from the measured resistance.[9-11]

To account for nonuniform probe spacing, the probes were lowered onto an aluminized microscope slide and the spacing measured with a traveling microscope. This procedure was repeated several times and a correction term generated from theory.[9] This correction factor was also checked by measuring the resistivity of a transmutation doped and annealed sample which had been calibrated by the Van der Pauw technique.[12] Agreement was found to be better than 1% for a 5 Ω-cm sample. All samples are measured in a dark box.

Since the A.S.T.M. Standard for resistivities over 2000 Ω-cm suggested that measurements could not be made to an accuracy of better than ± 15%, extreme care was taken to check the probe calibration factor periodically for high resistivity measurements.[11]

An ingot which had been cut into five bulk samples ($\rho \sim 2500$ Ω-cm) and characterized by four-point probes at Rockwell International was measured at MURR. Care was taken to use a current sufficiently low that sample heating did not

affect the measurements. The results of I-V plots for two sides of sample VZ-072-#5 are shown in Figures 14 and 15. The nonlinearity in these measurements at high currents is due to sample heating.

Note that the linear portions of the curves do not go through the origin. This offset voltage can be measured on the voltmeter in the absence of current and is observed to vary with probe pressure, surface condition of the sample and position of the probes on the sample. Although this effect is negligible for 5 Ω-cm material, the offset voltage can become an appreciable part of the signal voltage for high resistivity samples. It was also noticed that the slope near the origin is independent of the offset. This fact allows us to make correct measurements up to very high resistivities if proper data handling is used. The problem is overcome by measuring both the positive and negative voltages resulting from positive and negative supply currents to determine the effective resistance. This resistance is then equal to $[V(+) - V(-)]/[I(+) - I(-)]$. This resistance determines the slope of the lines in Figures 14 and 15 and the product of this slope times the probe factor determines the resistivity.

Results of a series of measurements on the five bulk samples, VZ-072-#1 through #5, are compared to results obtained by Dr. Arst at Rockwell and are shown in Table 5.

It is seen that the agreement between the two laboratories

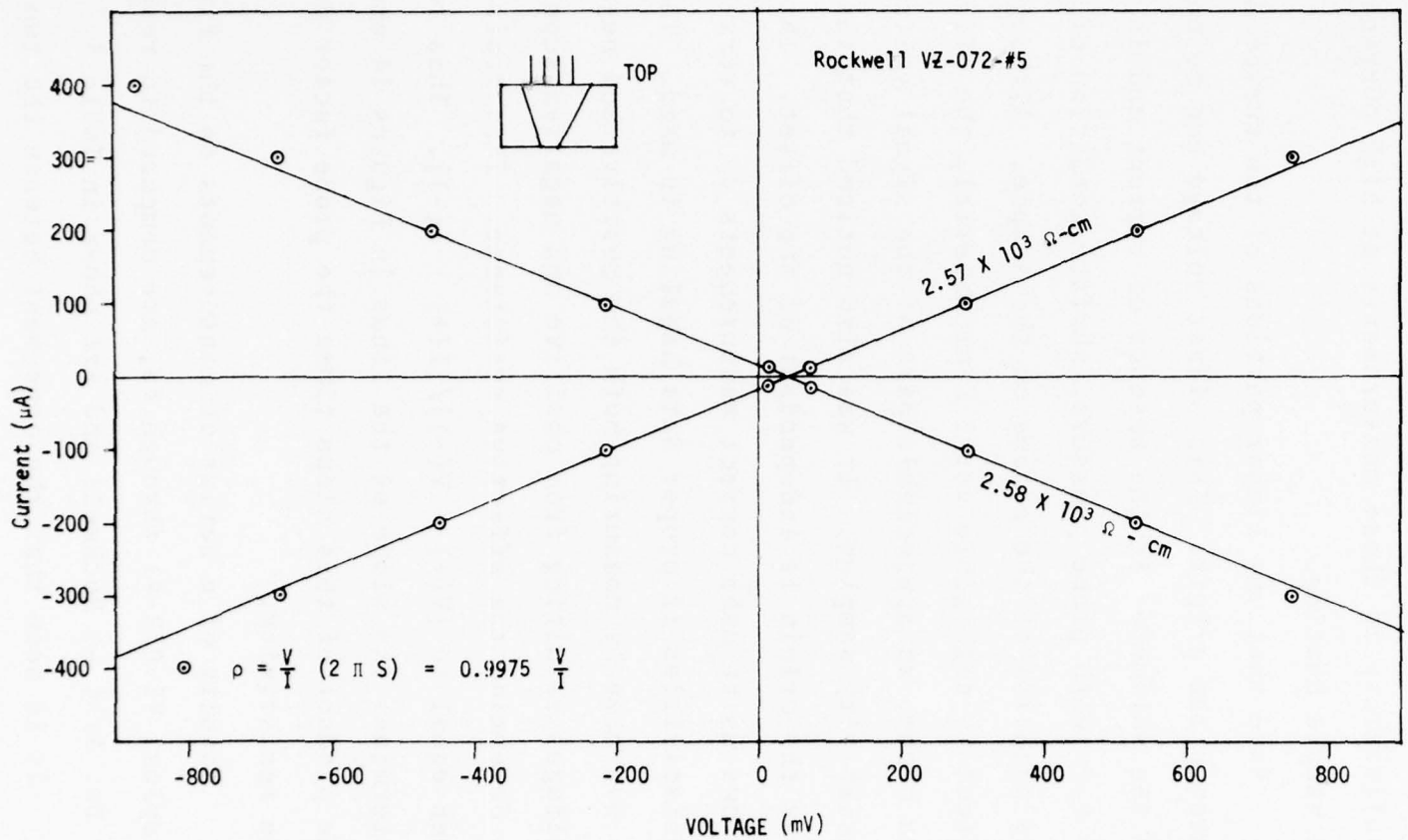

Figure 14. Current vs. voltage for four point probe resistivity measurement (top of VZ-072-#5).

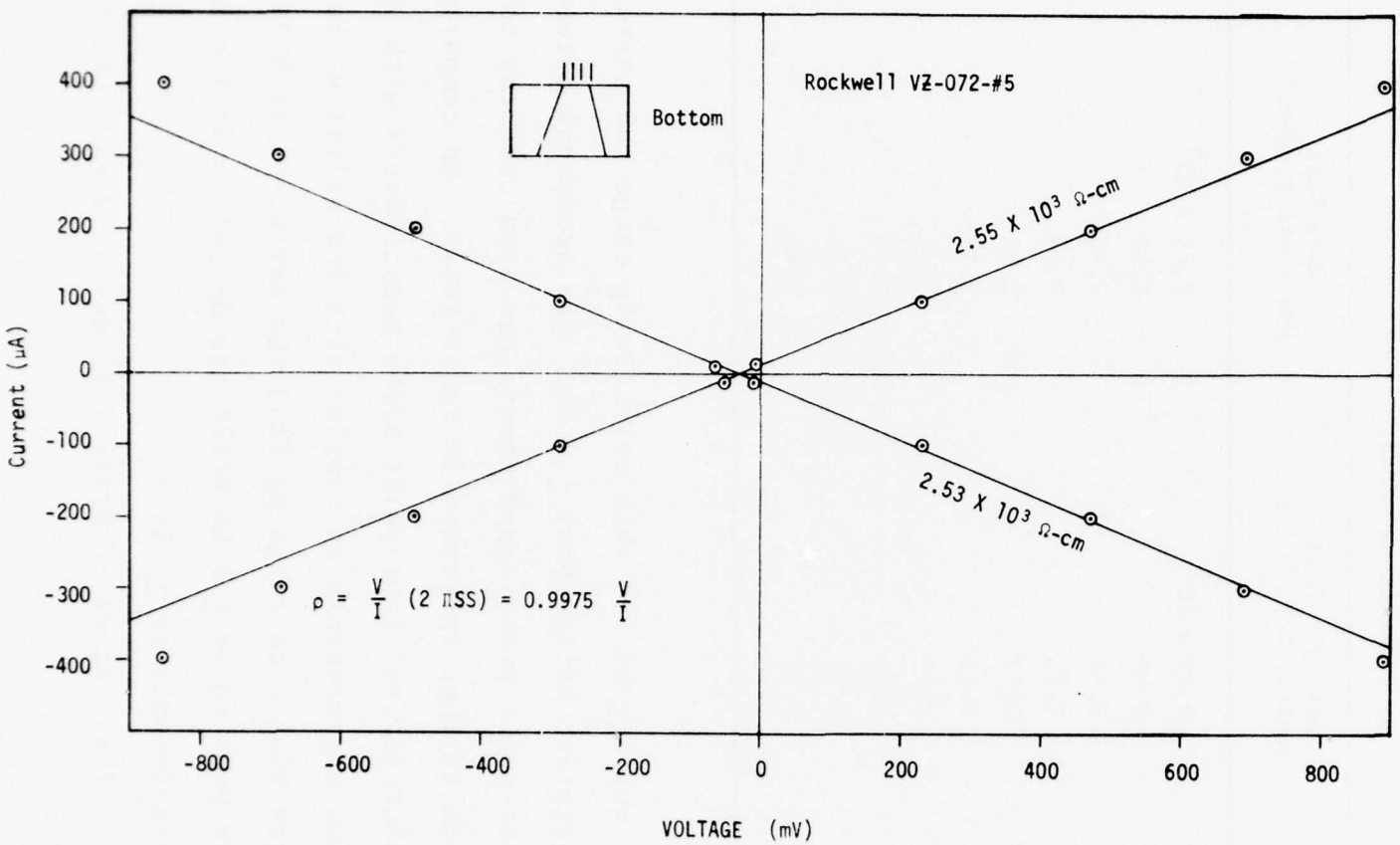

Figure 15. Current vs. voltage for bottom of VZ-072-#5.

TABLE 5. A comparsion of four point probe resistivity measurements made at Rockwell and MURR.

Sample	Rockwell Data Resistivity (Ω-cm)	MURR Data Resistivity (Ω-cm)	$100 \frac{\rho_r - \rho_m}{\rho_m}$
#1(T)	2.29×10^3	2.27×10^3	+0.88
#1(B)	2.42	2.43	-0.41
#2(T)	2.43	2.45	-0.82
#2(B)	2.53	2.53	0.00
#3(T)	2.50	2.52	-0.99
#3(B)	2.57	2.58	-0.39
#4(T)	2.57	2.58	-0.39
#4(B)	2.55	2.56	-0.39
#5(T)	2.55	2.55	0.00
#5(B)	2.53	2.49	+1.61

is quite good for this resistivity range the average deviation being about ± 0.6%. The agreement between the four-point probe measurements has been observed to decrease with further increases in resistivity. On comparing both laboratories' four-point probe measurements with Van der Pauw measurements on samples with resistivities in the 7000-8000 Ω-cm range we find the deviation at MURR from Van der Pauw to be ± 1.5% while the deviation of the Rockwell measurements is ± 5%.

This increased error with resistivity seems to be

following a power law dependence given by the expression

$$100 \frac{\Delta\rho}{\rho} = K\rho^{n} .$$

Although the constant K is smaller for our data than for that given by the A.S.T.M., the value for n is in reasonable agreement. We find the following to hold for the two sets of data:

$$100 \frac{\Delta\rho}{\rho} = 0.1\ \rho^{0.71} \qquad \text{(A.S.T.M.)}$$

$$100 \frac{\Delta\rho}{\rho} = 0.001\ \rho^{0.81} \qquad \text{(MURR).}$$

The physical meaning of these equations is obscure, however, a similar power law is observed for the calibration curves for spreading resistance measurements.[13] The difference between the A.S.T.M. and MURR values for K is not understood, however, the A.S.T.M. data is taken for both n- and p-type Si in various orientations while the MURR data is taken on p-type only on a [111] face. The upper expression is useful for estimating the maximum expected error for intrinsic material at 230,000 Ω-cm. We find an expected error of about ± 22% at this resistivity value. This estimated error is in reasonable agreement with deviations in resistivity for samples neutron irradiated to the same fluence but before annealing (nearly intrinsic but slightly p-type).

F. Minority Carrier Lifetime Apparatus

The minority carrier lifetime of all ingots before irradiation and some after irradiation and annealing has

been measured by the photoconductive decay technique. Ingots are coated with Aquadag solution on each end and held in a small lab vise to which braided copper shielding wire has been flattened and attached to the vise jaws for contacting. The contacting area is shielded from the light to prevent photovoltaic effects from the contacts. This effect can be detected if observed as a linear decay of the junction capacitance of a blocking contact.

A small power supply provides the bias voltage across the sample and a variable series load resistor. This resistor is adjusted for maximum signal before data is taken, an essential procedure for interpretation of the decay.[14] Optical excitation is provided by a General Radio Strobotac model 1531-AB[15] whose pulse time is short compared to the photoconductive decay time constant. The signal is observed with a Tektronix Type 547 oscilloscope with a dual trace plug-in unit.[16]

Typical decay voltages as a function of time are shown in Fig. 16. It can be shown that the voltage signal as a function of time for the condition that R(load) = R(sample) is given by[17]

$$\frac{V(t)}{V_{bias}} = \frac{\left(\frac{\Delta n}{n_o}\right)_o e^{-t/\tau}}{\left\{1 + \left[1 + \left(\frac{\Delta n}{n_o}\right)_o e^{-t/\tau}\right]^{\frac{1}{2}}\right\}^2} \tag{24}$$

where $(\Delta n/n_o)_o$ is the maximum change in minority carrier

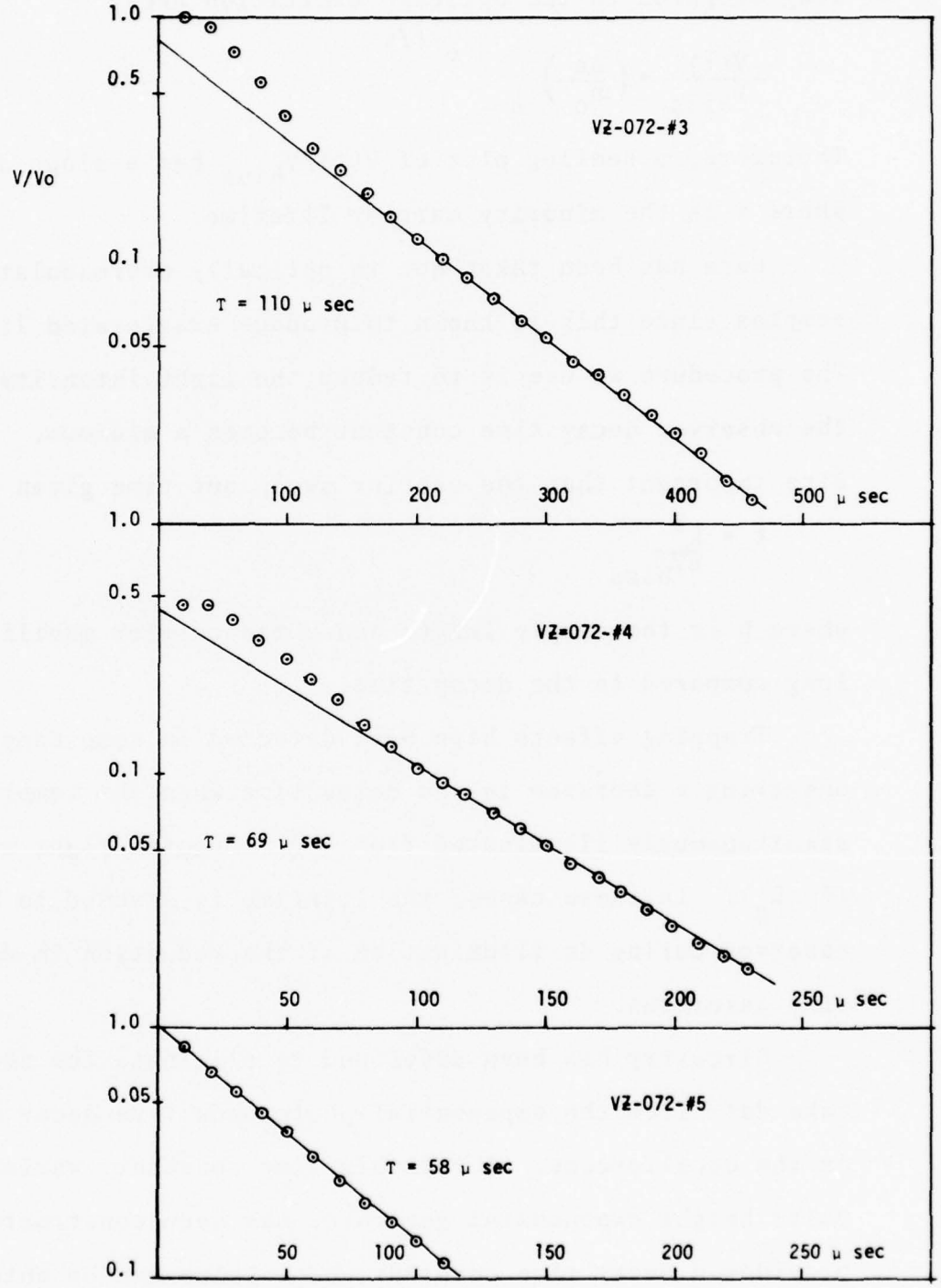

Figure 16. Typical photoconductive decay curves for determining minority carrier lifetime.

concentration and τ is the carrier lifetime. For times long compared to the optical excitation decay

$$\frac{V(t)}{V_{bias}} \rightarrow \left(\frac{\Delta n}{n_o}\right)_o e^{-t/\tau} .$$

Therefore, a semilog plot of $V(t)/V_{bias}$ has a slope of τ^{-1} where τ is the minority carrier lifetime.

Care has been taken not to optically overmodulate the samples since this is known to produce exaggerated lifetimes. The procedure we use is to reduce the light intensity until the observed decay time constant becomes a minimum. It is also important that the carrier sweep out time given by

$$t = \frac{L^2}{\mu V_{bias}}$$

where L is the sample length and μ the carrier mobility, be long compared to the decay time.

Trapping effects have been detected in some samples by observing a decrease in the decay time when the sample is simultaneously illuminated from a dc tungsten light source ($\hbar\omega < E_g$). In these cases, the lifetime is assumed to be that observed during dc illumination if the reduction in decay time saturates.

Circuitry has been developed to eliminate the need to take data from the exponential photoconductive decay displayed on the oscilloscope. A variable time constant, variable pulse height exponential generator has been constructed which provides a decay time constant whose value can be obtained

from the setting of a ten-turn pot. This exponential pulse is triggered from the strobotac, inverted, and added to the photoconductive decay signal. The oscilloscope then functions as a null detector. A straight line signal indicates that the exponential generator has matched the photoconductive signal in both amplitude and time constant. Deviations from non-exponential decays and trapping effects are easily detected with this system. A schematic of the system is shown in Figure 17 while a circuit diagram for the exponential pulse generator is shown in Figure 18.

G. High Impedance Van der Pauw Resistivity and Hall System (Electronics, Vacuum System, and Helitran).

Resistivity and mobility can be determined as a function of temperature from about 8°K to room temperature by this system. Temperature control is obtained from a Helitran[18] and temperature controller. The system is capable of measuring resistances of high impedance samples up to a resistivity of about 10^{12} Ω-cm. A dc guarded lead approach[19] in which each sample lead guard is driven by a separate high input impedance unity gain amplifier (Keithley[5] Model 602) to the voltage on the inner lead reduces leakage currents and improves the system's time constant. The circuitry for this approach is shown in Reference 19. The digital voltmeter and constant current source from the four-point probe system are also used in this system. A switching circuit connecting the appropriate sample leads to the proper

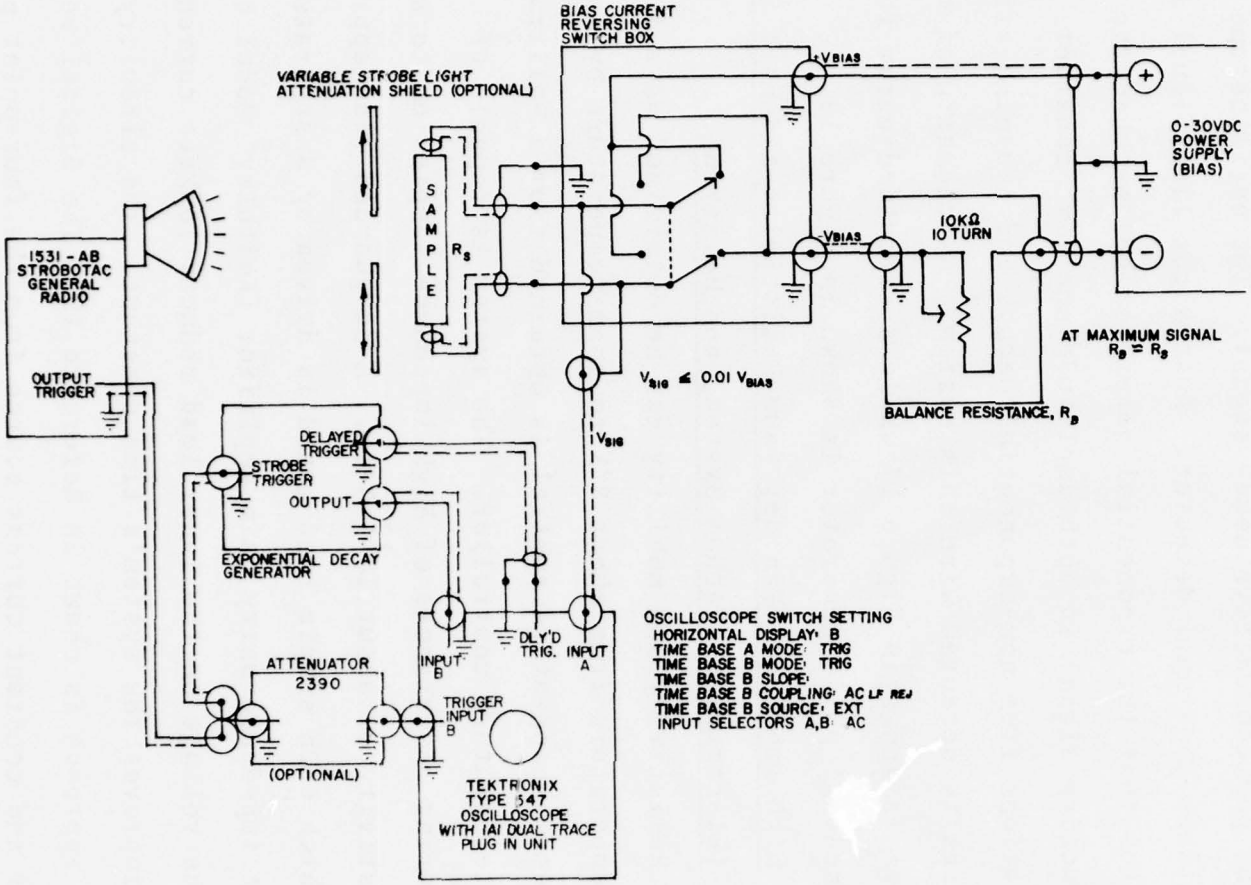

CARRIER LIFETIME MEASUREMENT APPARATUS

Figure 17. Minority carrier lifetime measurement apparatus.

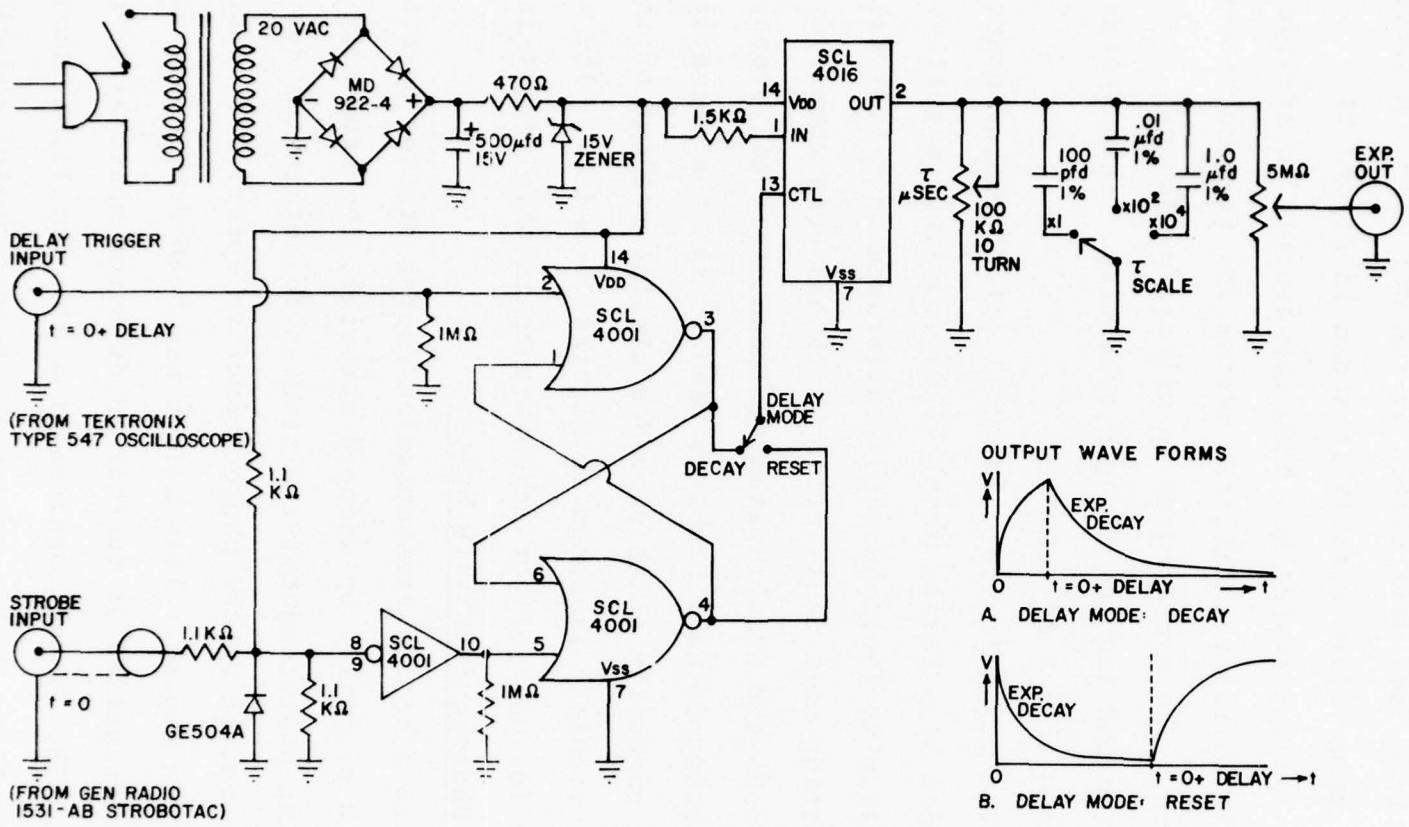

EXPONENTIAL DECAY GENERATOR

Figure 18. Exponential decay generator.

electrometer and current source allows either conventional resistivity and Hall effect or Van der Pauw[12] measurements to be made. This circuit is shown in Figure 19.

A vacuum system has been constructed to provide evacuation for the Helitran system and for the vacuum annealing. The system uses an oil diffusion pump, mechanical forepump and liquid nitrogen cold trap. This system provides a vacuum of 5×10^{-7} torr.

The magnetic field for Hall effect measurements is provided by a Varian Model V4004 four-inch magnet system.[20] The magnetic field has been calibrated to $\pm$ 1.3% using both a rotating coil Gauss meter which has been compared to an NMR probe and a calibrated semiconductor Hall probe. The semiconductor Hall probe is used to set the magnetic field using circuitry which provides digital readout of the field. This circuitry is shown in Figures 20 and 21. The magnetic field for Hall effect measurements in this report is 6.195 kG.

H. Photoconductivity System

Because the transmutation doping studies have been performed primarily on undoped material, the necessity of performing photoconductivity studies to obtain the degree of compensation or the photoconductive spectral responses have not been needed. This system has been developed, however, in anticipation of further IR detector spectral response work. The system consists of a glow bar light source, a Perkin-Elmer double pass prism monochrometer and electronics,

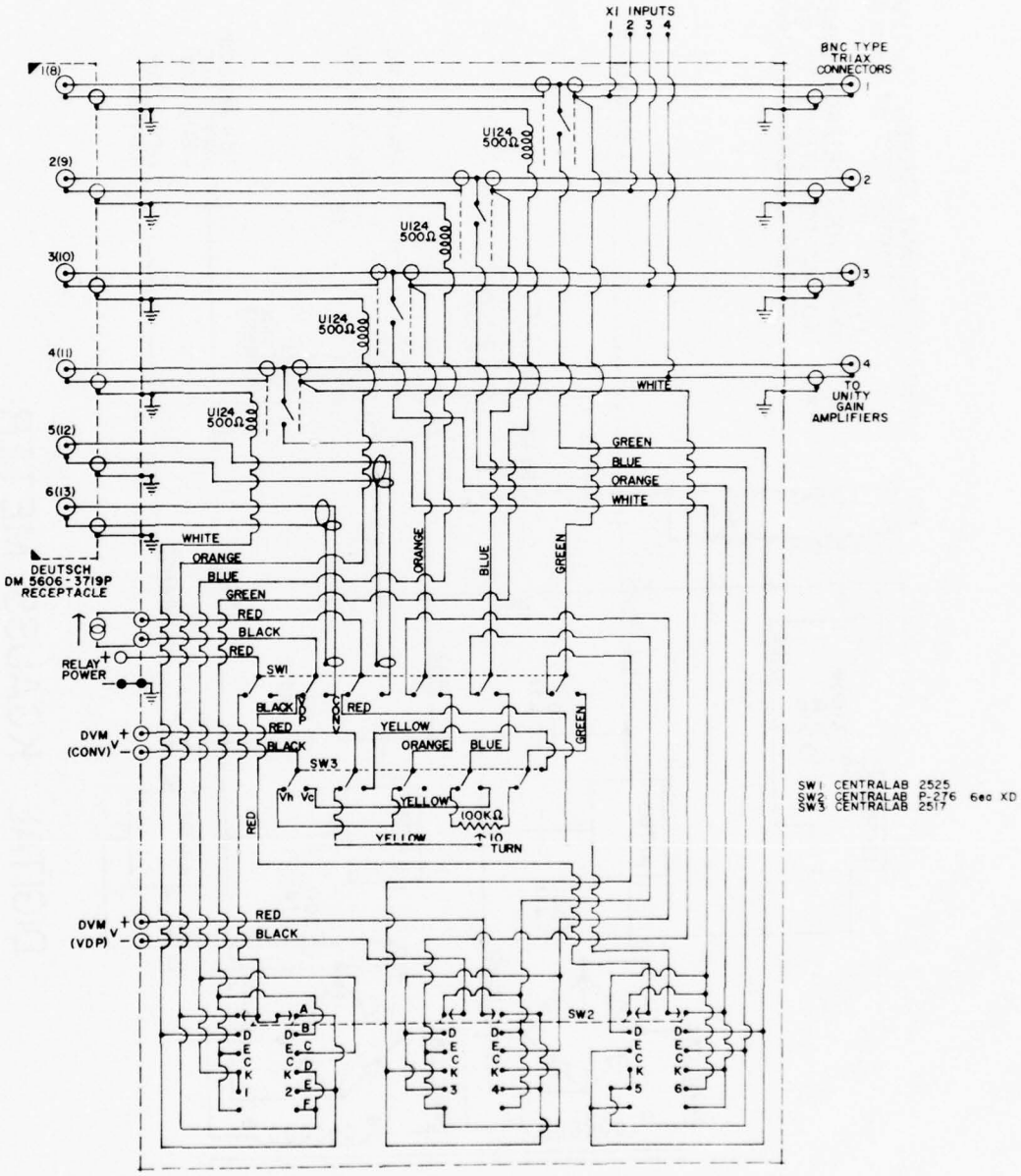

HALL / VAN DER PAUW MEASUREMENT SWITCHBOX

Figure 19. Switching circuit for resistivity and Hall effect measurements.

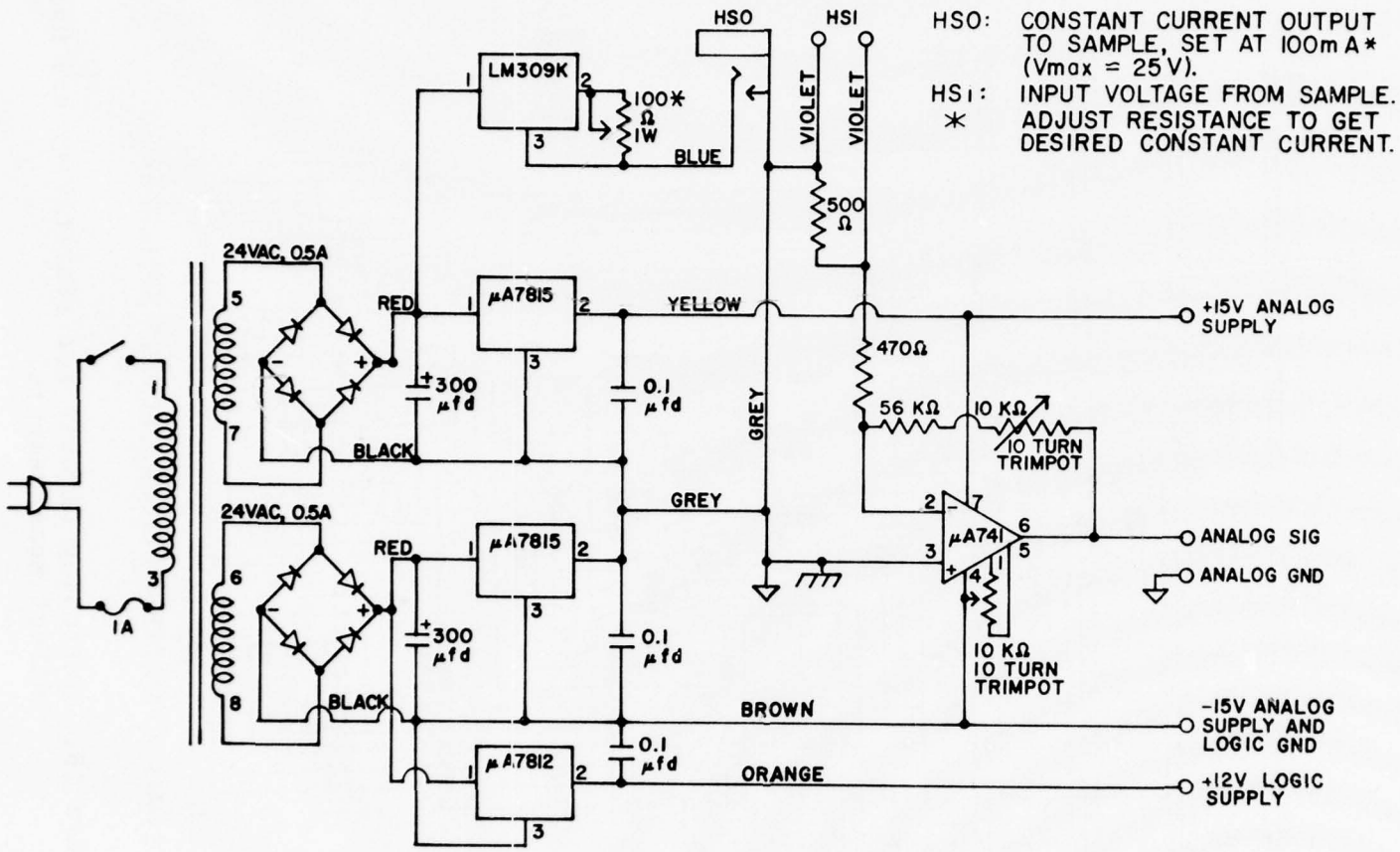

DIGITAL KGAUSS METER

Figure 20. Analog voltage amplifier and current source for digital Gaussmeter.

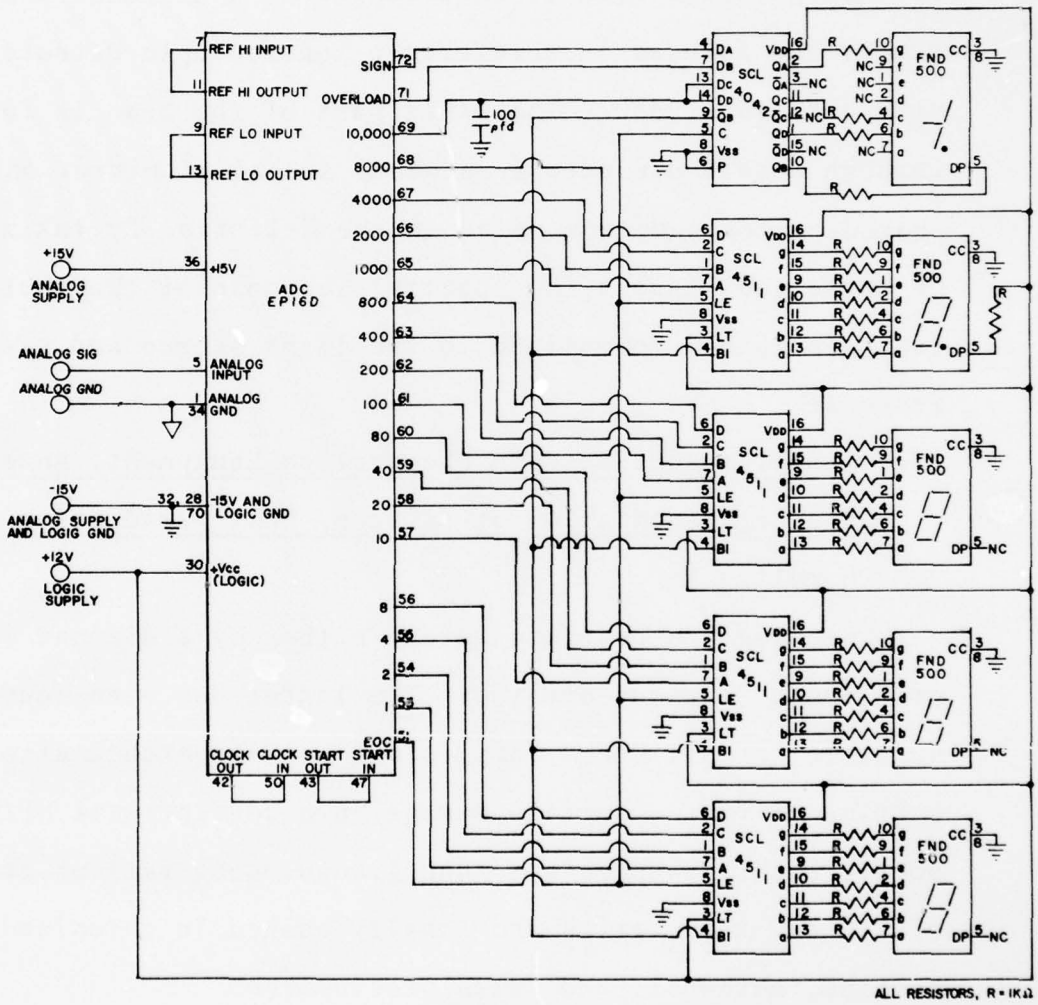

DIGITAL KGAUSS METER

Figure 21. Analog to digital converter circuitry for digital Gaussmeter.

two thermocouple detectors and exit optics. The prism and windows are KRS-5 material (1-50 μm). The exit beam from the monochrometer which is diverging is intercepted by a spherical mirror to produce a parallel beam of light. Part of this parallel beam is interrupted by a diagonal plane mirror and focused on a reference thermocouple detector with a KRS-5 window. The other part of the beam is focused through a second window by another spherical mirror onto the photodetector sample mounted in the Helitran. By taking ratios of these two signals the spectral response of the photodetector can be obtained normalized to the light source and system response.

I. Miscellaneous: Sample Preparation Equipment, Annealing System, Irradiation of Silicon, Post-Irradiation Handling

Samples are cut into wafers either by a diamond wire saw or diamond disk cut-off saw. The latter has been found more suitable for silicon. Samples are heavily etched after cutting to remove surface damage in a conventional HF/HNO_3/ acetic etch. Samples are then ground using various grades of SiC and Al_3O_4 grits and finally washed in deionized water, acetone, methanol, and trichloroethylene.

Samples are annealed in a tube furnace inside a Spectrasil quartz tube. The sample may be annealed in either a vacuum of 5×10^{-7} torr. or in a flowing inert gas atmosphere. Sample surfaces are protected on each side with a wafer of float

zone silicon to prevent contamination by the quartz. The furnace is capable of temperatures of up to 1000°C. The temperature is regulated to ± 0.5°C.

Samples to be irradiated are placed between silicon spacers; the whole stack of samples and spacers is then wrapped in aluminum foil. The flux wires are now wrapped around the foil and the whole package is placed in an aluminum can which is welded shut to protect the silicon from the pool water. Radioactivity is monitored after a cool-off period in the reactor pool. For the very light irradiations in this project, radioactivity decays to background very quickly and has usually been attributed to surface contamination where encountered.

A considerable effort has been spent studying surface contamination after irradiation but before annealing. By careful handling, surface contamination has usually not been detected before annealing except for a Au contamination on one sample from sawing in another laboratory before our saws were operational. A few samples have also shown traces of Na from handling. This has been eliminated by a light HF cleaning after irradiation but before annealing. We are confident that our samples are usually extremely clean prior to annealing based on activation analysis and electrical measurements after annealing.

IV. EXPERIMENTAL RESULTS AND DISCUSSION

In this section, the prior-to-irradiation material evaluation,

irradiation and annealing experiments are discussed. We have noted several differences in our results from previously published work and will discuss these differences in the following subsections. A preliminary activation energy for the thermal ionization of the irradiation produced donors has been measured. We have been able to determine that the best single annealing temperature for NTD-Si is at above 800°C for one hour followed by a very slow cool down. We have also made a preliminary assessment of the effects of fast to thermal neutron ratios.

Although material from a variety of Si producers has been evaluated, we have found that control by compensation on the p-type side of type conversion from 5000 Ω-cm to intrinsic is impossible in the material we have investigated thus far. We will present data which suggests that residual oxygen is the source of difficulty.

We have also demonstrated very good control of resistivity on the n-type side of type conversion. We have shown that the final resistivity can be controlled to at least $\pm$ 2% using only a preliminary check of ingot mobility and four-point probe measurements. We have sound experimental evidence at this point which suggests that it may be possible to achieve this degree of control up to n-type resistivities as high as 100,000 Ω-cm. This corresponds to an excess donor concentration of $\sim 8 \times 10^{-4}$ ppb or about 4×10^{10} donors/cm^3. It may thus be possible to compensate residual boron concentrations of about this order of magnitude or larger.

One of the more exciting possibilities to develop out of the present work is residual oxygen decoration by damage defects. Circumstantial evidence suggests that oxygen detection in Si can be pushed at least three orders of magnitude below present detection limits. If the preliminary results can be substantiated by EPR and optical measurements, considerable progress in Si purification can be made as a result of this technique.

A sound experimental approach has been developed for determining the amount of boron in the samples prior to irradiation, which is available to those IR detector manufacturers who perform their own Ga or In doping. We feel that this can be done successfully with high accuracy only before the optically active impurity is added to the ingot. Although other techniques are available to determine boron concentration after the addition of Ga or In, none rival in accuracy the technique of multizone passes and four-point probing prior to optical activation by Ga or In doping.

We have also been able to establish, both theoretically and experimentally, the resistivity uniformity to be expected as a function of distance across the wafer for various compensation ratios. This is, perhaps, the most important single result of the present work since results clearly show that compensation by nuclear transmutation offers a significant and considerable improvement over conventionally compensated material in the compensation range useful for IR detectors.

We have also been able to relate the final resistivity fluctuatuions observed for various compensation ratios to the

initial boron fluctuations in starting material in a quantative way. It is, therefore, possible for the first time to place criteria on the boron fluctuations as determined by the desired final wafer uniformity and compensation ratio. The theoretical and experimental results we have obtained indicate that nuclear transmutation compensation will be a necessary technique for uniformity criteria now envisioned for Si IR detector array integration.

A. Materials Evaluation Before Irradiation

All the material investigated has been multizone refined float zone silicon with resistivities from 2500 Ω-cm up to 25000 Ω-cm. The material is p-type and not intentionally doped. The dominant acceptor is undoubtedly boron. All of the material is nominally dislocation free and pulled in a [111] direction except the Rockwell material which is dislocated and pulled in a [100] direction. Some preliminary electrical data on a Wacker's [100] pulled Ga doped sample have been taken. Neutron reflection rocking curves show reflection line widths of about 1 sec of arc for the dislocation free material and about 1 min of arc for the dislocated material. Material investigated has come from Dr. Arst, Rockwell; Topsil, Wackers, Monsanto, Hughes, and a Texas Instruments Lopex sample supplied by Dr. Spry of AFML. We have added an in-house number to each ingot or wafer (MURR #) and have cross-referenced these numbers with whatever sample designations have been assigned to the samples by the suppliers.

Much effort has been expended in trying to purchase float zone silicon which is doped with either In or Ga.

Approximately thirty manufacturers of silicon were contacted by phone and requests for bids sent out to ten, however, no bids were received for this type of material. We have, however, received free, doped samples from a number of sources and greatfully acknowledge their help. We have received Czochralski grown Si:Ga doped to a variety of levels in the range of 10^{16} to 10^{18} cm^{-3} from Drs. M. Bressler and C. M. Parry, Aerojet ElectroSystems Co. We have also received a supply of Wacker's Ga doped vacuum float zone material from Dr. M. Schlacter, Aeronutronic Ford. Dr. Arst of Rockwell has also supplied us with Ga doped float zone.

Table 6 summarizes sample characterization before irradiation. As discussed in a previous section, four-point resistivity measurements have been compared with Van der Pauw resistivity measurements for calibration purposes. Mobility measurements have been taken from one slice of each ingot and the values are very near average values given in Table 3. Note, however, that the mobility in the Wacker's sample is some 13% too low. This is probably due to the effect of mixed conduction in this very high resistivity sample.

Figure 22 shows the axial resistivity and minority carrier lifetime of ingot VZ-072 after cutting it into slices of approximately 1" thickness. Figures 23 through 28 show the radial uniformity of these samples as obtained from four-point measurements. Figure 29 shows the uniformity of

TABLE 6. Summary of Undoped Sample Characterization Before Irradiation.

MURR #	Source	ρ(4 pt) (Ω-cm)	ρ (V.d.P.) (Ω-cm)	μ_D (cm^2/V-sec)	Type T.P.	Type Hall	τ (μsec)
0	Monsanto FZ	749.0			P		-
1	Rockwell VZ-072-3	2560.			P		110
2	VZ-072-3	2953.			P		110
3	VZ-072-3	3156.			P		110
4	VZ-072-3		2721.	464.75	P	P	110
5	Monsanto FZ		1690.	1383.4	N	N	-
6	Monsanto FZ		1037.5	1404.5	N	N	-
7	Rockwell VZ-072-2	2450-2530 (ingot)			P		112
8	Rockwell VZ-083-4	7630.	7729.	524.8	P	P	-
9	Rockwell VZ-083-5	8189.	8067.	527.8	P		-
10	Monsanto CZ	(after irrad & anneal)	3.222	1267.0	N	N	-
11	Monsanto FZ		1376.2	1473.5	N	N	-
14	Topsil 36-520-0-III				P		1200
15	Topsil 36-520-0-III	4710-6467	(1" ingot)		P		1200
16	Topsil 36-520-0-III	4742.			P		1200
17	Wackers 30661-6	66512. ?			P		530
18	T.I. Lopex L1092	4607			P		250
19	Topsil 36-520-0-III		4942.	460.	P	P	1200
20	T.I. Lopex L1092		5195.9	443.86	P	P	250
21	Wacker 30661-6	19370.			P		530 (trappin
22	Wacker 30661-6	20420.		427.0	P	P	530

TABLE 6. Summary of Undoped Sample Characterization Before Irradiation (Cont.).

MURR #	Source	ρ (4 pt) (Ω-cm)	ρ(V.d.P.) (Ω-cm)	μ_D (cm^2/V-sec)	Type T.P.	Type Hall	τ (μsec)
23	Similar to MURR	10			N		-
24	Wacker 30661-6	For NAA			P		530
25	T.I. Lopex L1092	For NAA			P		250
26	Topsil 36-520-0-III	For NAA			P		1200
27	Topsil 36-520-0-III	5248			P		1200
28	Monsanto FZ	1540			N		-
29	Rockwell VZ-083-17	12509.			P		-
30	Rockwell VZ-083-18	12796			P		-
31	Rockwell VZ-083-19	13326			P		-
32	Rockwell VZ-083-20	13687			P		-
33	Rockwell VZ-083-21	14160			P		-
34	Rockwell VZ-083-22	14382			P		-
35	T.I. Lopex L1092	5895			P		-
36	T.I. Lopex L1092	5587.6			P		-
37	Rockwell VZ-065-1	For NAA			P		
38	Rockwell VZ-065-2	For NAA			P		
38-45	Rockwell VZ-065 wafers	(not used)			P		
46	Hughes FO-1770602	6183-6776 (ingot)			p		1200
47	Hughes FO-1771101	5610-8360 (ingot)			P		2000

TABLE 6. Summary of Undoped Sample Characterization Before Irradiation (Cont.).

MURR #	Source	ρ(4 pt) (Ω-cm)	ρ (V.d.P.) (Ω-cm)	μ_D (cm^2/V-sec)	Type T.P.	Type Hall	τ (μsec)
48	Hughes FO-1770602	5785 (fast neutron irrad.)			P		
49	Hughes FO-1770602	5675 (isochronal anneal)			P		
50-64	Rockwell Ga doped detector material GZ-156-6 to GZ-156-20 from VZ 107	0.431-0.450, [B] = 5.42 x 10^{12} cm^{-3}			P before Ga added		
65	Rockwell GZ-156-G	For NAA Fig. 52	ρ(x) in Ga doped		P		
66	Rockwell VZ-083-50-1	17510	ρ(x) for [P]/[B] = 10				
67-68	T.I. Lopex L1092	Irradiated and sent to Ramdas, Purdue for optical measurements					
69	Rockwell VZ-083-50-2	Fig. 53	ρ(x) in half wafer vs whole wafer				
70	Rockwell VZ-083-50-3	18970	ρ(x) for [P]/[B] = 1.12				
71	Rockwell GZ-141-2	ρ(x) in conventionally compensated sample					
72	Rockwell GZ-141-3	ρ(x) in conventionally compensated sample					
73	Rockwell GZ-156-23	For NAA in Ga-doped (not completed)					
74	Hughes FO-177062	For NAA (not completed)					
77	Wackers 102531-II<100>	p vs 1/T (Ga doped) Fig. 32					
78	Rockwell GZ-156-H	ρ(x) in Ga doped					
79	Rockwell VZ-083-50-4	19460	ρ(x) for [P]/[B] = 2.04				
80	Rockwell VZ-083-50-5	19480	ρ(x) for [P]/[B] = 3.52				
81	Rockwell VZ-083-50-6	19380	ρ(x) for [P]/[B] = 4.45				
85	Rockwell GZ-156-21	p vs. 1/T (Ga-doped) Fig. 33					
86	Hughes FO-1770602	ρ(x) Fig. 30					

TABLE 6. Summary of Undoped Sample Characterization Before Irradiation (Cont.).

MURR #	Source	ρ(4 pt) (Ω-cm)	ρ (V.d.P.) (Ω-cm)	μ_D (cm^2/V-sec)	Type T.P.	Type Hall	τ (μsec)
To Check Uniformity	VZ-072-1	2270-2430	ρ(x) Figs. 23-28				
	VZ-072-2	2450-2530					
	VZ-072-3	2520-2580					
	VZ-072-4	2580-2560					
	VZ-072-5	2550-2490					

VZ-083, while Figure 30 shows the uniformity of a Hughes sample. The rise in resistivity near the ends of these wafers is due to edge effects and is not real.[9]

Table 7 summarizes the minority carrier lifetime for the various ingots which have been measured.

TABLE 7. Summary of Minority Carrier Lifetimes.

Source	Ingot No.	τ Measured	τ Specified by Manuf.
Rockwell	VZ-072	100 μsec	100 μsec
Topsil	36-520-0-III	1200 (trapping)	1700
T.I. Lopex	L 1092	250	500
Wacker	30661-6	530	3200
Hughes	FO-1770602	1200	900

We believe that the lifetimes in this resistivity range are probably over exaggerated by the suppliers because of over-modulation in experimental set ups designed in general for lower resistivity material. It should be noted that our observed lifetimes for the Rockwell material are in general agreement with their measurements. The lifetime of the Topsil material indicates some evidence of trapping that does not saturate. It is, therefore, possible that the real lifetime is shorter. We would estimate, however, that it is probably not shorter than 500 μsec. The lifetime of the Hughes sample was the largest found and was free of trapping. This sample is a [111] pull, however.

Table 8 summarizes the drift mobilities observed for the various ingots obtained from Hall mobilities using the relationship for the Hall factor shown in the table.

TABLE 8. Summary of Drift Mobilities.

Source	Ingot No.	Type	μ_D (cm^2/V-sec)
Rockwell	VZ-072	P	465
Rockwell	VZ-083	P	525-528
Topsil	36-520-0-III	P	460
T. I. Lopex	L1092	P	444
Wacker	30661-6	P	427
Monsanto FZ	-	N	1383-1473
Typical (from Table 3 and p. 3)		P	494
		N	1396

$r_p = \mu_H/\mu_D = 0.77$

$r_n = 1.3$

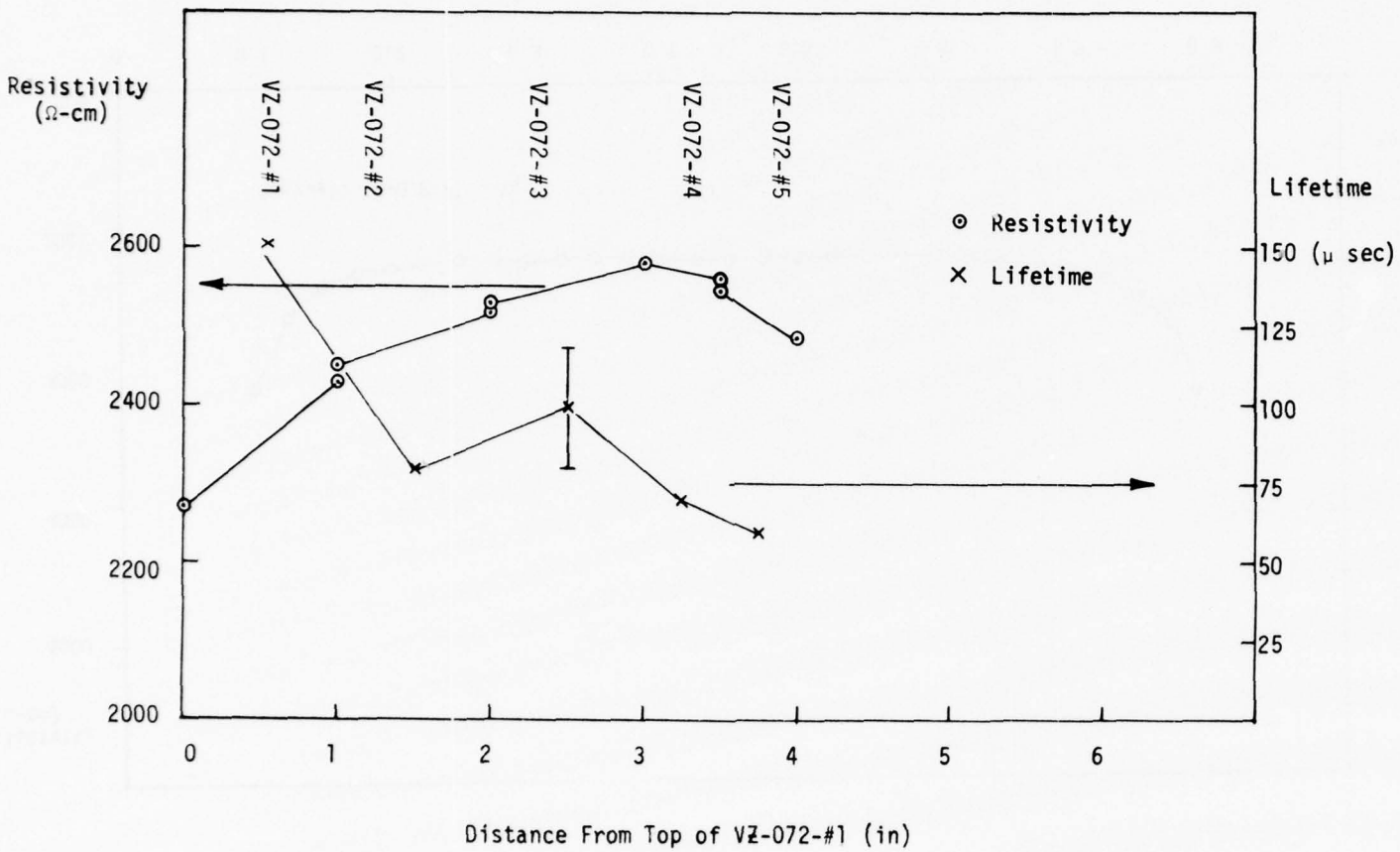

Figure 22. Axial resistivity and axial lifetime of 1 in. or 1/2 in. pieces from VZ-072.

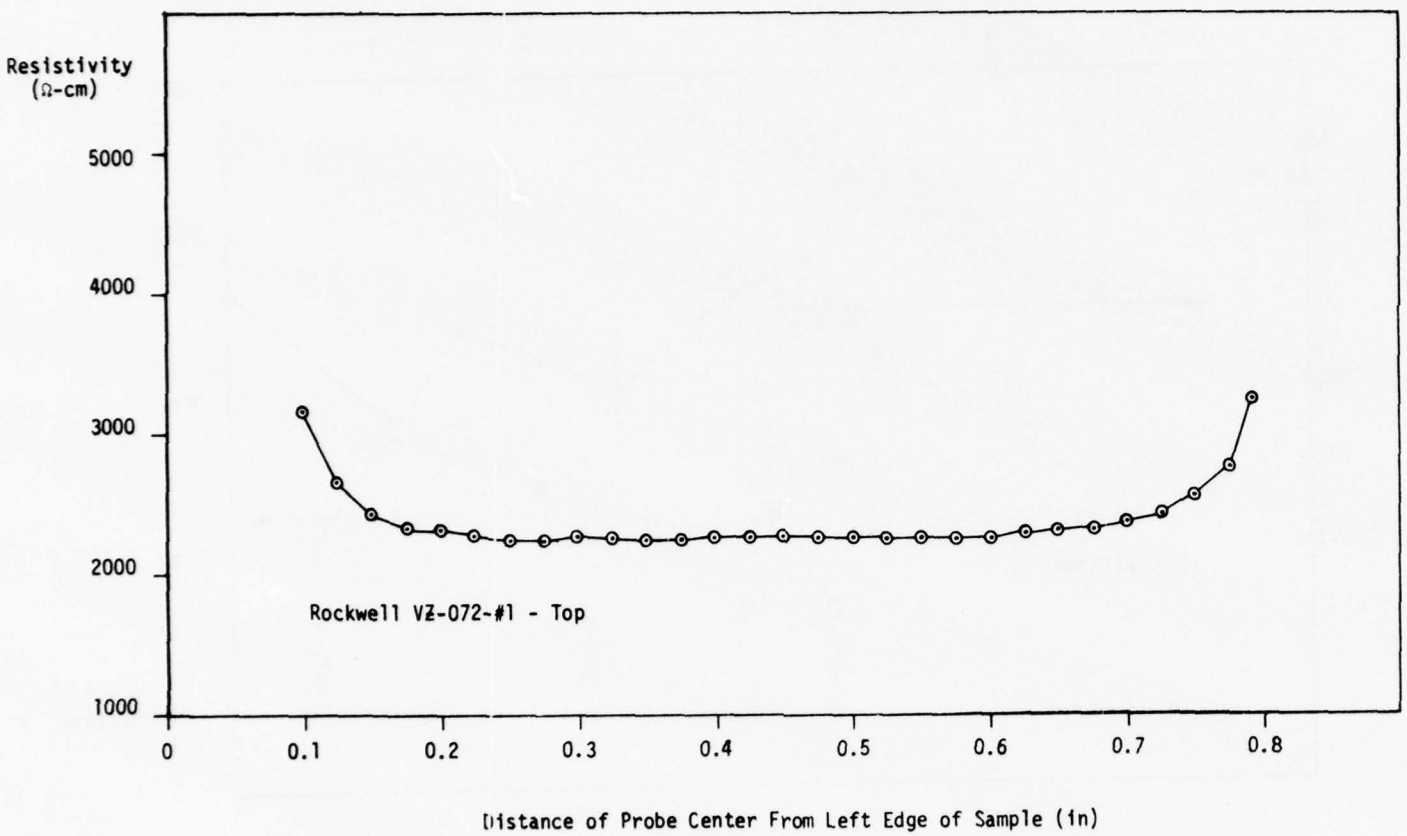

Figure 23. Radial resistivity of VZ-072-1-top.

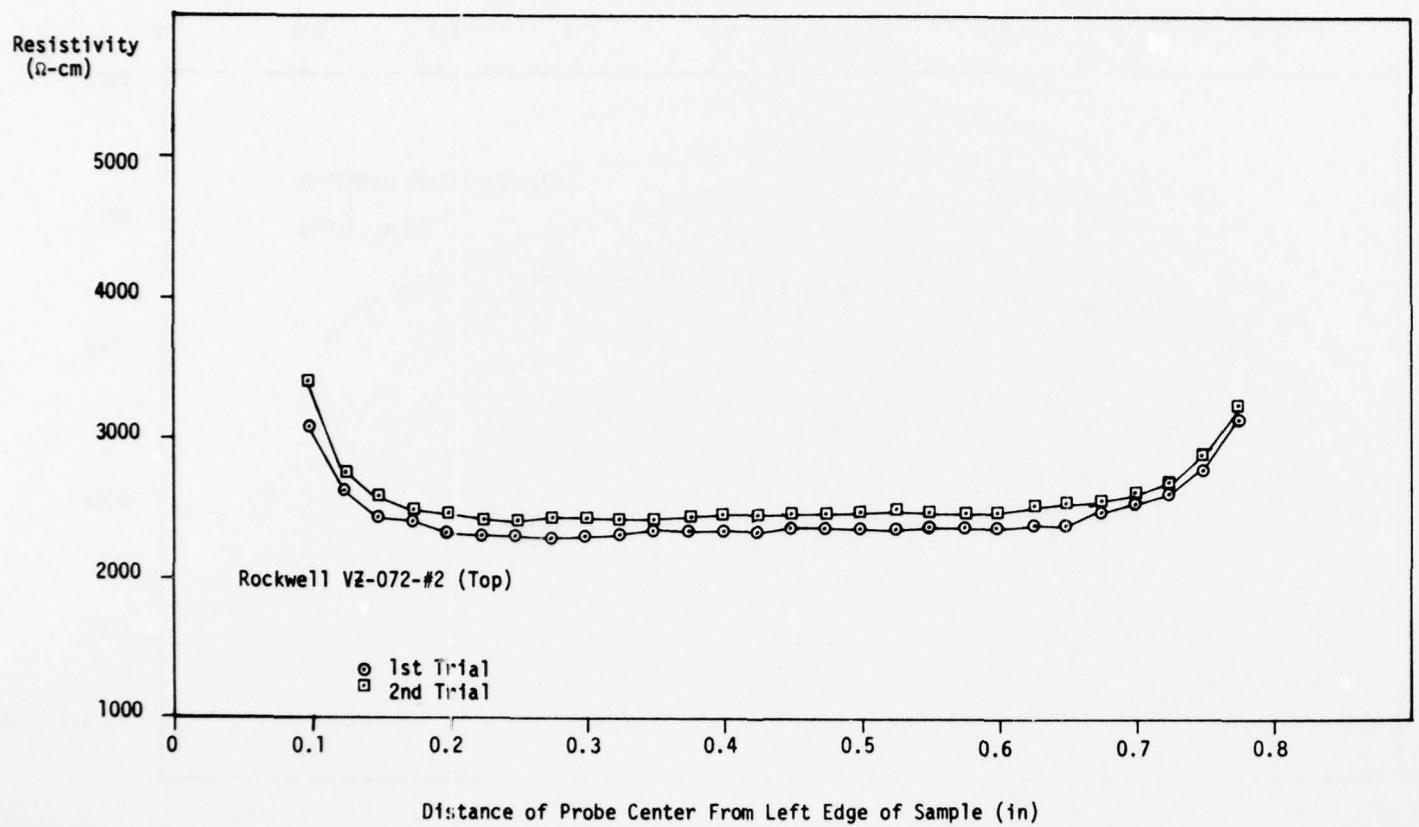

Figure 24. Radial resistivity of VZ-072-2-top.

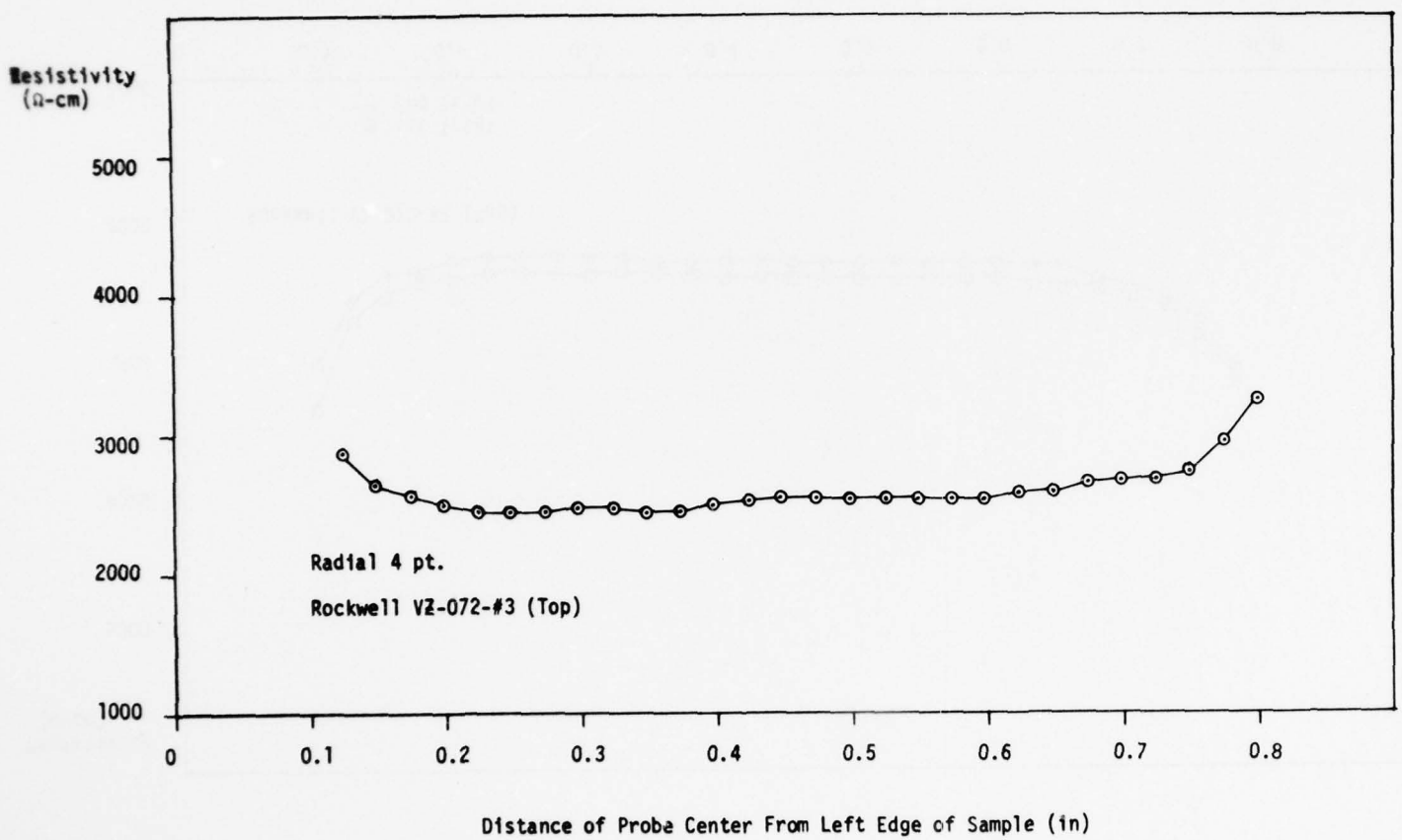

Figure 25. Radial resistivity of VZ-072-3-top.

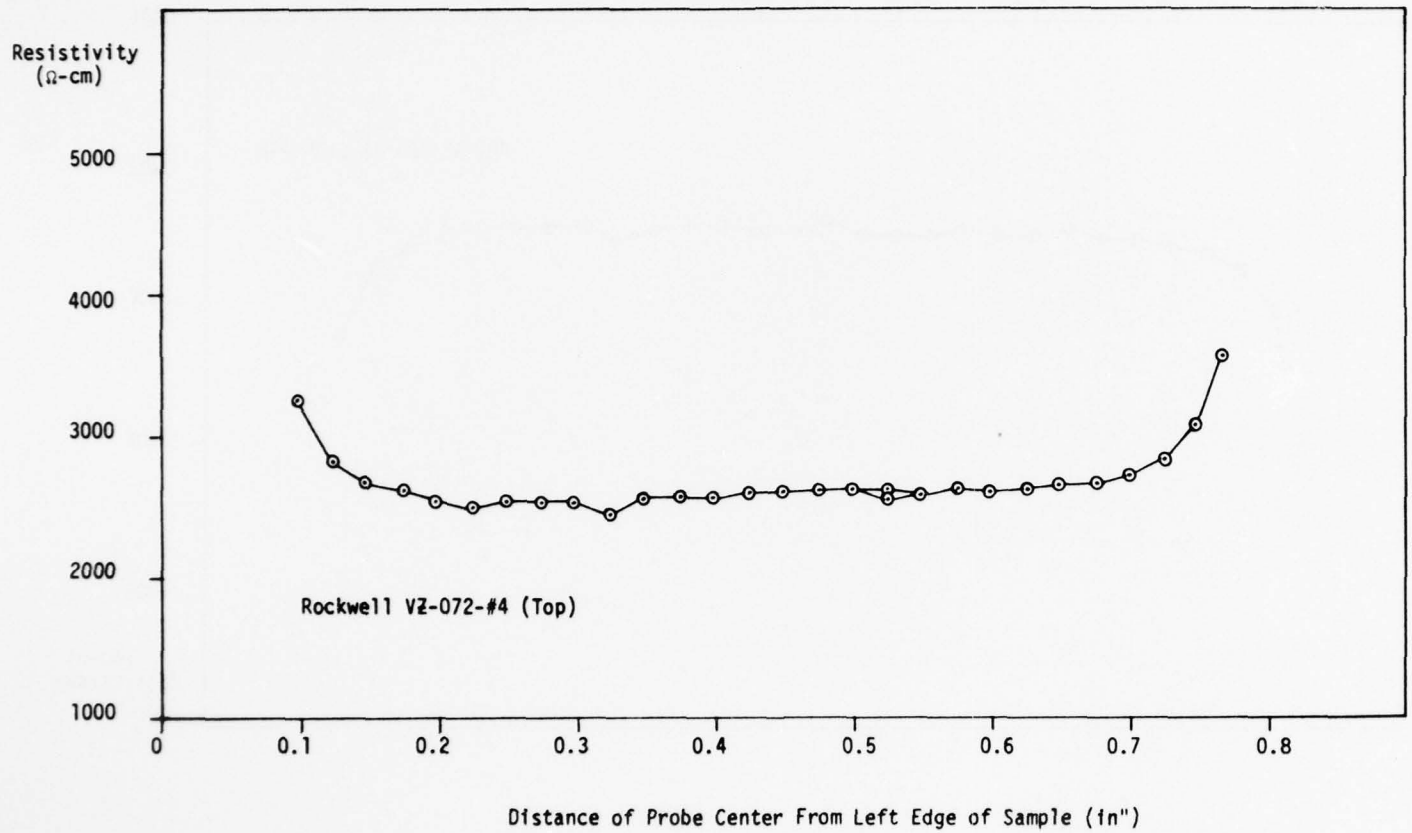

Figure 26. Radial resistivity of VZ-072-4-top.

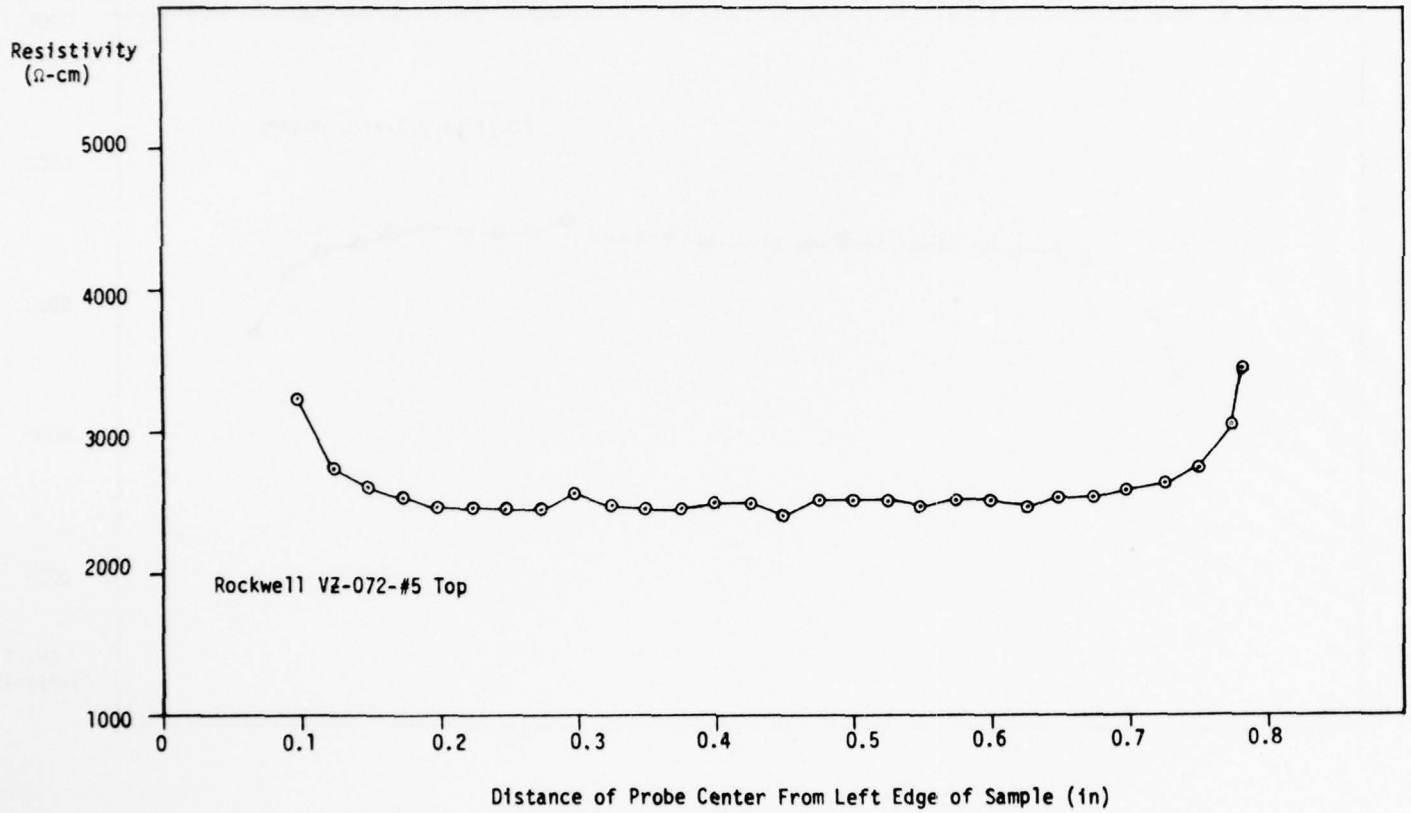

Figure 27. Radial resistivity of VZ-072-5-top.

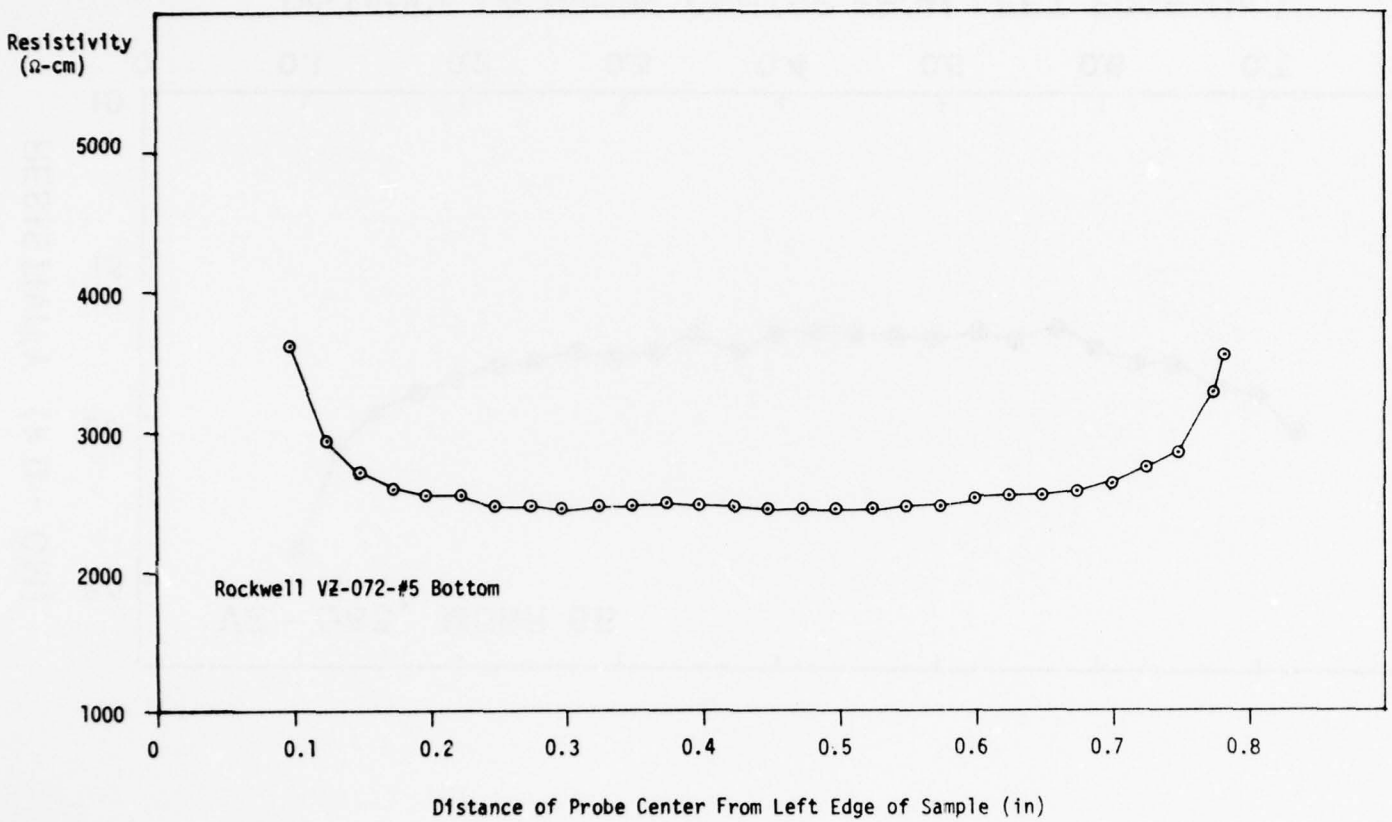

Figure 28. Radial resistivity of VZ-072-5-bottom.

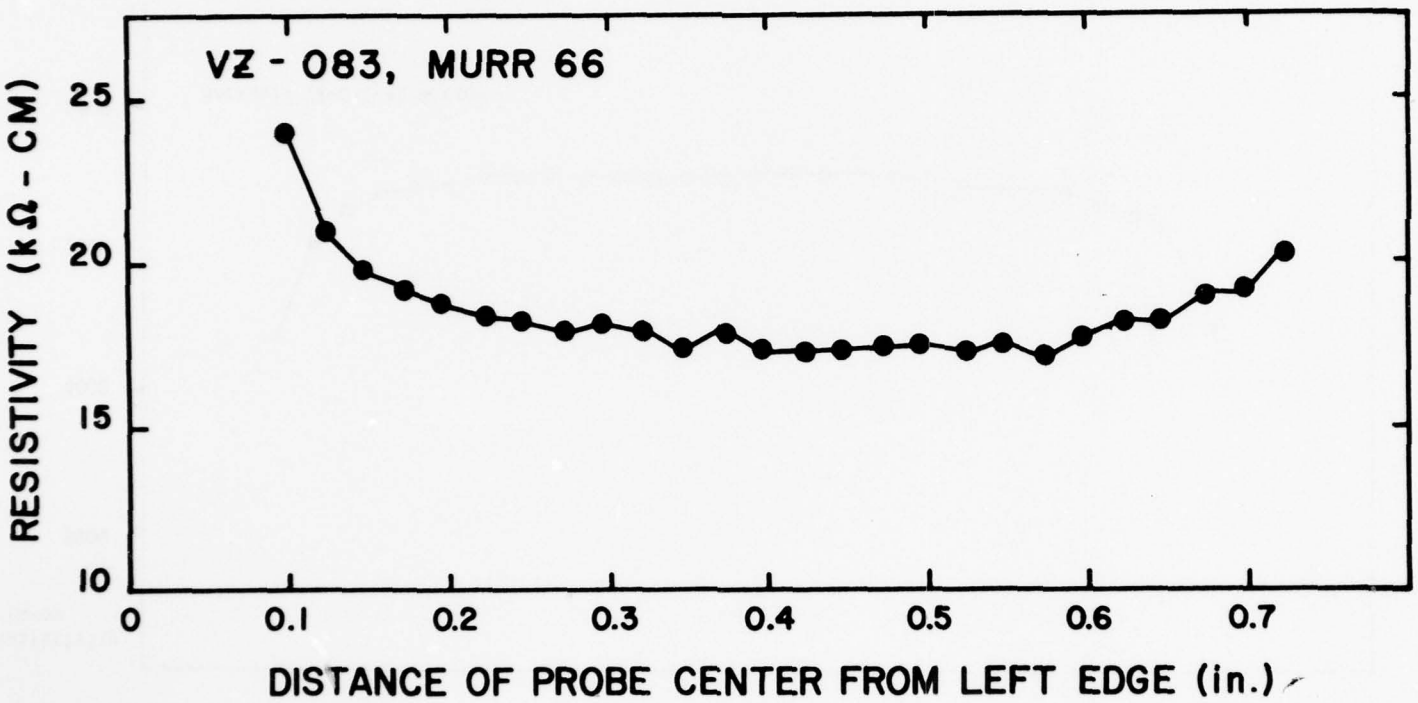

Figure 29. Radial resistivity of a typical VZ-083 sample.

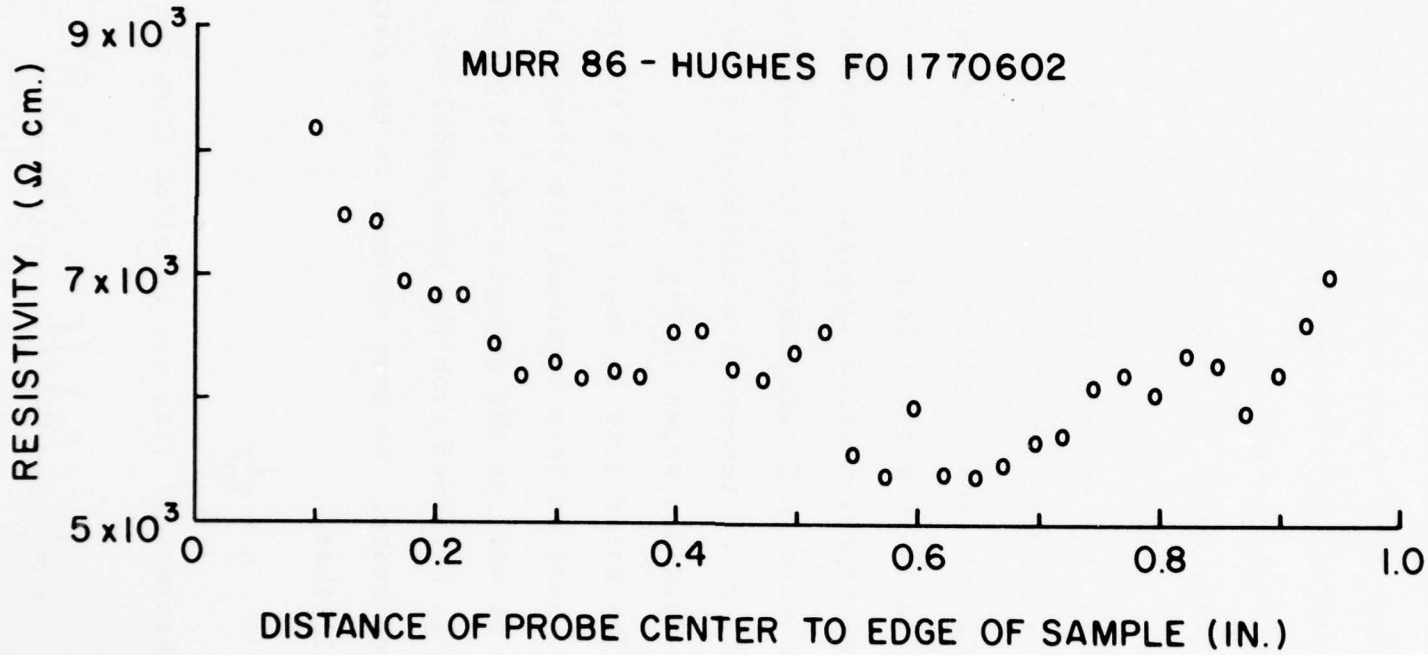

Figure 30. Radial resistivity of a typical Hughes wafer.

We conclude, based on the data in Tables 7 and 8 that the materials from these sources are of comparable crystal quality. The Rockwell material exhibits inferior lifetime and crystal perfection; however, the material was pulled in a [100] direction, which is more difficult. Apparently, a [111] Rockwell pull would be of comparable crystal quality. In addition, the Rockwell material has the advantage of extremely uniform boron distribution as evidenced by Figures 23-28.

Carrier concentration from Hall effect measurements as a function of reciprocal temperature have been measured for several representative samples. A Monsanto Czochralski sample which had been heavily transmutation doped was first used to check temperature calibration and system operation. These data are shown in Fig. 31.

The solid line in Fig. 31 is a theoretical fit to these data, where we have included the effects of the first excited state as well as the ground state of phosphorus.[21] The dotted curve is obtained from the same model but neglecting the first excited state. We have assumed in the data represented in Fig. 31 that

$$n = \frac{1}{R_H e} \quad .$$

The theoretical fits are obtained from the relation

$$n = \left(\frac{\kappa + N_A}{2}\right) \left\{\left[1 + \frac{\kappa (N_D - N_A)}{\left(\frac{\kappa + N_A}{2}\right)^2}\right]^{\frac{1}{2}} - 1\right\} \tag{25}$$

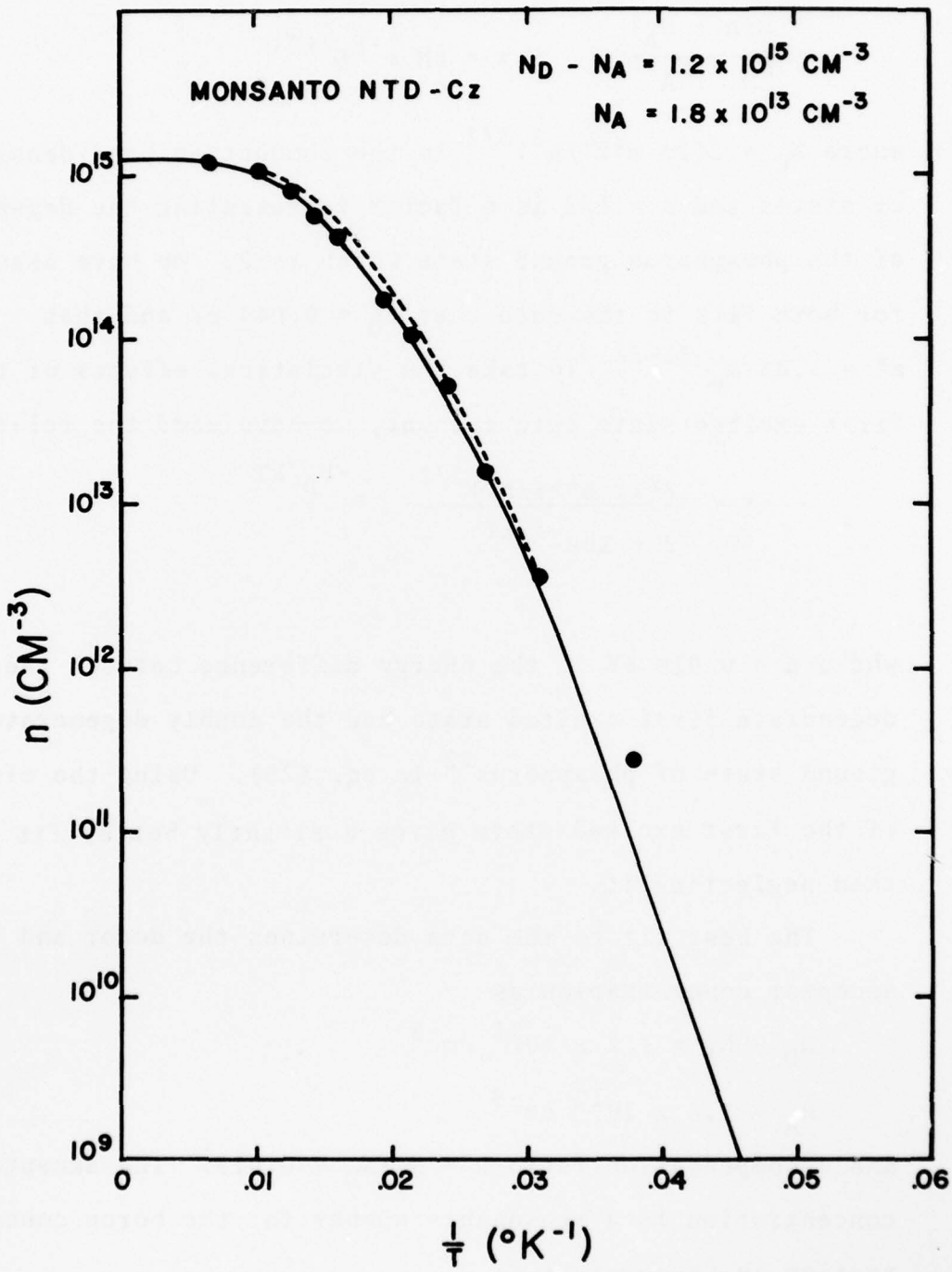

Figure 31. Carrier concentration vs. reciprocal temperature for a neutron transmutation doped Czochralski wafer.

which is equivalent to the more usual relationship[22]

$$\frac{n(n + N_A)}{N_D - N_A - n} = \kappa = \beta N_C e^{-E_D/kT}$$

where $N_C = 2(2\pi\ m^*kT/h^2)^{3/2}$ is the conduction band density of states and $\beta = 1/2$ is a factor representing the degeneracy of the phosphorus ground state which is 2. We have assumed for both fits to the data that $E_D = 0.044$ eV and that $m^* = 1.08\ m_e$.[22-26] To take the statistical effects of the first excited state into account, we have used the relation

$$\kappa = \frac{2(2\pi\ m^*kT/h^2)^{3/2}}{2 + 10e^{-\Delta/kT}}\ e^{-E_D/kT}$$

where $\Delta = 0.010$ eV is the energy difference between the tenfold degenerate first excited state and the doubly degenerate ground state of phosphorus[22] in Eq. (25). Using the effect of the first excited state gives a slightly better fit than neglecting it.

The best fit to the data determines the donor and acceptor concentration as

$$N_D - N_A = 1.2 \times 10^{15}\ cm^{-3}$$

$$N_A = 1.8 \times 10^{13}\ cm^{-3}$$

and a compensation ratio $k = N_A/N_D = 0.015$. The acceptor concentration is a reasonable number for the boron concentration in Czochralski Si.

The deviation from the fit at low temperature ($\frac{1}{T} > 0.035$) is due to impurity conduction. This effect is usually seen in compensated material[27-29] and is caused in Fig. 31 by a carrier tunneling from an occupied donor level to an unoccupied donor level. Although several models for explaining the change in activation energy at low temperatures as a function of compensation exist for resistivity data,[27-29] no adequate model has been proposed to explain the Hall coefficient data.[27,29] It is not clear in Figure 31 whether the carrier concentration goes through a minimum between the last two data points or whether the minimum is at still lower temperature. Since the effect of impurity conduction occurs at higher temperatures in Si than in Ge, because of the relative depths of similar impurities, it is doubtful that low boron concentration in a gallium doped sample can be determined with any high degree of accuracy because of interference from impurity hopping conduction induced by the always present compensation.

The above model for n-type material with a single donor level and acceptor levels far removed from the Fermi level can be extended to the case of Ga doped Si. In this p-type material, two acceptor levels dominate the position of the Fermi level and the donor levels are far removed from it. To describe this situation, we use the same model as the Hughes group.[30]

Using charge conservation

$$p + N_D = N_1 f'(E_1) + N_2 f'(E_2)$$

where N_1 is the concentration of gallium atoms, N_2 the concentration of boron, $f'(E)$ the Fermi function for hole occupation of an energy level at energy E above the valence band, and E_1 and E_2 are the gallium and boron ground state ionization energies respectively. Then, using the Boltzman approximation

$$p = N_V e^{E_f/kT}$$

to eliminate the Fermi energy from the above equation, we find that

$$p + N_D = \frac{N_1}{\left(1 + \frac{p}{K_1}\right)} + \frac{N_2}{\left(1 + \frac{p}{K_2}\right)}$$

and rearranging, we arrive at the cubic equation for the hole concentration, p,

$$(p + N_D)(p + K_1)(p + K_2) - N_1K_1(p + K_2) - N_2K_2(p + K_1) = 0$$

where

$$K_1 = \frac{N_V}{\beta} e^{-E_1/kT}$$

$$K_2 = \frac{N_V}{\beta} e^{-E_2/kT}$$

$$N_V = 2(2\pi m^* kT/h^2)^{3/2}.$$

We have used the following parameters to obtain fits to the experimental data:

E_1 (gallium) = 0.065 eV

E_2 (boron) = 0.045 eV

$m^* = 0.59\ m_o$

$\beta = 4$.

The temperature dependence of the effective mass and the acceptor excited states have been neglected.

A computer code to solve the cubic equation for each value of 1/T has been completed. This code uses the "Half Interval Search" method to find the positive real root of the cubic equation for p given above.

The data for a Ga doped wafer from Wacker are shown in Fig. 32 along with several theoretical fits calculated from the above model. The curves are not particularly sensitive to N_2 and N_D. Our best estimates for these concentrations are

$$N_1 = N(Ga) = 1.78 \times 10^{16} cm^{-3}$$

$$N_2 = N(B) = (1.25 \pm 0.25) \times 10^{13} \ cm^{-3}$$

$$1 \times 10^{12} \simeq N_D << 1 \times 10^{13} \ cm^{-3} .$$

Also included are curves for $N_B/N_D = 1.5$ (curve 3). $N_B/N_D = 1.0$ for exact compensation (curve 4), and $N_D/N_B = 3.0$ for over compensation (curve 5). It is clear that some information about compensation can be obtained from this type of data, however, the sensitivity to changes in N_D is not very good for cases of interest.

Figure 33 is a similar carrier concentration plot vs. reciprocal temperature for a Ga doped Rockwell sample, GZ-156-21. These data have not been analysed in detail yet since they are recently taken.

B. Neutron Activation Analysis

An instrumental neutron activation analysis (INAA) procedure for measuring trace element impurities in high

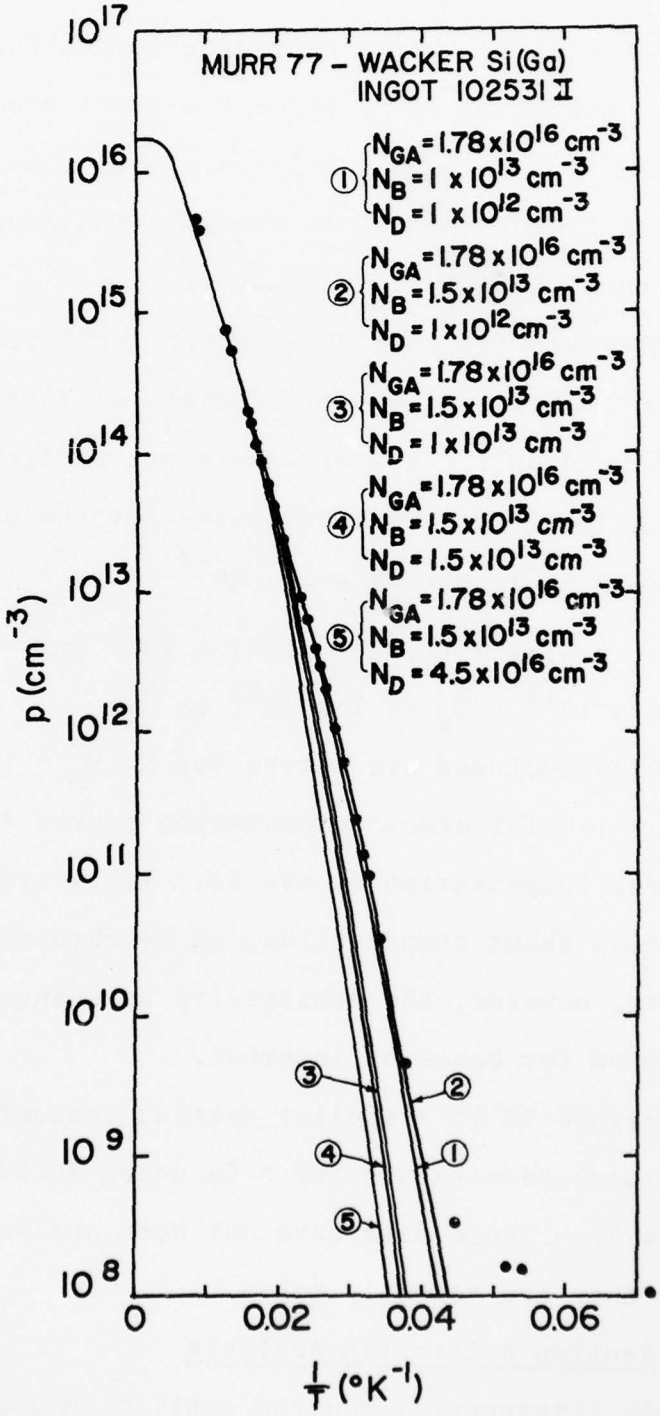

Figure 32. Carrier concentration vs. reciprocal temperature for a Wacker Ga doped float zone wafer 102531-II (MURR-77).

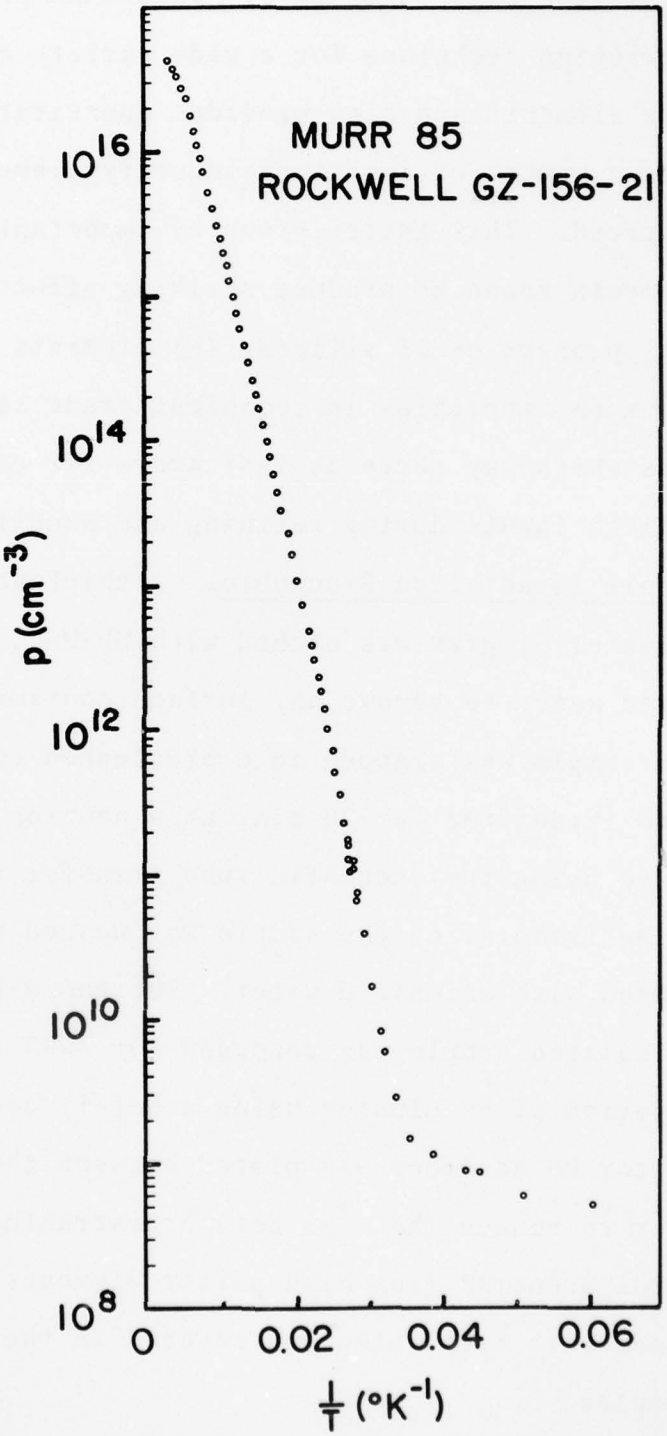

Figure 33. Carrier concentration vs. reciprocal temperature for a Rockwell Ga doped float zone wafer GZ-156-21 (MURR-85).

AD-A057 786 MISSOURI UNIV-COLUMBIA RESEARCH REACTOR FACILITY F/G 20/12
SILICON DETECTOR COMPENSATION BY NUCLEAR TRANSMUTATION.(U)
FEB 78 J M MEESE F33615-76-C-5230

UNCLASSIFIED AFML-TR-77-178 NL

2 OF 2
AD
A057786

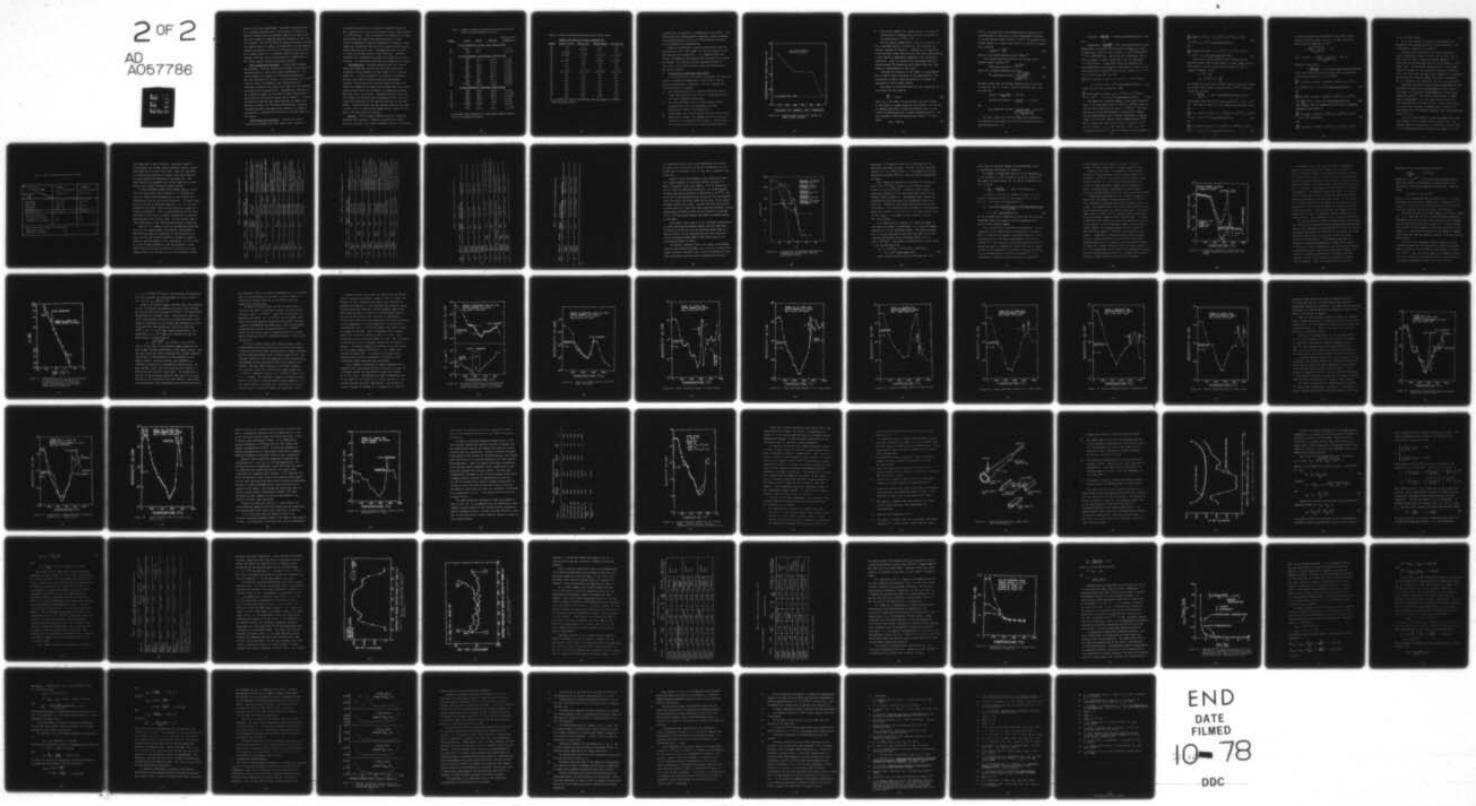

END
DATE
FILMED
10-78
DDC

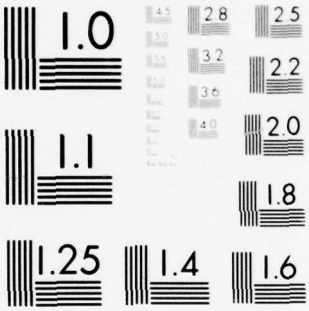

MICROCOPY RESOLUTION TEST CHART
NATIONAL BUREAU OF STANDARDS 1963-A

purity silicon was established. This INAA procedure serves as a screening technique for a wide variety of unexpected impurity elements and also provides quantitative upper limit data for a number of important impurity elements if they are not observed. This latter group of important elements include (a) elements known to produce striking effects on the physico-chemical properties of silicon, (b) elements which are known to be common impurities in technical grade silicon, and (c) elements which may serve as indicators for contamination of the silicon ingots during refining and handling.

Short Irradiation Procedure. A thick wafer weighing approximately 1 gram was etched with HF-HNO_3 and rinsed with deionized water to remove any surface contamination. The cleaned sample was wrapped in a precleaned polyethylene bag, and irradiated for 20 min. at a neutron flux of 8×10^{13} $n/cm^2/sec$ using the pneumatic tube transfer facility. Following irradiation the sample was washed with hot 8N HNO_3 and rinsed with deionized water. The gamma-ray spectrum of the irradiated sample was recorded for 2000 seconds after a decay period of 60 minutes using a Ge(Li) detector. A three millimeter Pb absorber was placed between the sample and detector to reduce the ^{31}Si beta bremstrahlung. Elemental standards prepared from high purity elements or weighable compounds were irradiated and counted in the same manner as the samples.

Long Irradiation Procedure. Following the short irradiation procedure, the same samples were wrapped in

aluminum foil, placed in a reflector irradiation canister, and irradiated for 40 hours at a neutron flux of approximately $1 \times 10^{14} n/cm^2/sec$. After irradiation the samples were etched with $HF-HNO_3$ and rinsed with deionized water to remove surface contamination from the aluminum foil wrapping. Each sample was counted for 2000 sec after decay periods of approximately 40 hours and 5 days. The gamma-ray spectra from 0 to 4 MeV was recorded using a Ge(Li) detector. Elemental standards were irradiated and counted according to the same schedule. The analytical conditions are summarized in Table 9.

Data Reduction. Existing computer codes were used to reduce the gamma-ray spectral data for both samples and standards to peak energies and peak areas for all observed gamma-rays. Isotope assignments were based on calculated energies and, where necessary, half-life measurements. Elemental concentrations for observed impurities were calculated by comparison of sample and standard peak areas after proper normalization of differences in irradiation exposure and decay time, if necessary. Minimum detectable peak areas for isotopes not observed were estimated as three times the statistical deviation of the spectral base line in the peak region. Detection limits for the elements measured are given in Table 9 for a 1 gram silicon sample using a value of 2.34 gm/c.c. for the density of silicon.

Results. Silicon ingots obtained from four different suppliers were analyzed. Elemental concentration values are given in Table 10 as atoms of impurity per c.c. of silicon

TABLE 9. Summary of Analytical Conditions and Detection Limits for Neutron Activation Analysis of Silicon.

Element	Isotope	Eγ(keV)	Half-Life	Detection Limit* (atoms/cc)
	20 min. Irradiation - 60 min. Decay - 2000 sec Count			
In	^{116m}In	1293.1		1×10^{11}
Mn	^{56}Mn	1812		1.5×10^{12}
	40 hour Irradiation - 40 hour Decay - 2000 sec Count			
Mo	^{99}Mo	140.6	66.6 h	4×10^{12}
Cu	^{64}Cu	511	12.75 h	7×10^{11}
Ga	^{72}Ga	834.1	14.1 h	3×10^{11}
Au	^{198}Au	411.8	64.7 h	2×10^{9}
W	^{187}W	685.7	23.9 h	1×10^{11}
As	^{76}As	559.2	26.4 h	1×10^{11}
Sb	^{122}Sb	564	65.8 h	6×10^{10}
Yb	^{175}Yb	396.1	101 h	8×10^{10}
Na	^{24}Na	1368.4	15.0 h	2×10^{12}
Eu	^{152m}Eu	841.6	9.3 h	5×10^{10}
	40 hour Irradiation - 5 day decay - 2000 sec Count			
Cr	^{51}Cr	320.0	27.8 d	9×10^{12}
Th	^{233}Pa	311.8	27.0 d	1.5×10^{11}
Sc	^{46}Sc	889.4	83.8 d	1.5×10^{11}
Hf	^{181}Hf	482.0	42.4 d	3×10^{11}
Co	^{60}Co	1173.1	5.25 y	8×10^{12}
Ag	^{110m}Ag	657.8	253 d	3×10^{12}
Ta	^{182}Ta	1121.2	115 d	1.5×10^{12}

*3 σ detection limit estimated for a 1 gram sample assuming a density value of 2.34 grams/cc for silicon.

TABLE 10. Elemental Concentrations Measured in Four Silicon Ingots.

Element	Impurity level measured in atoms of impurity/c.c.*			
	Rockwell VZ-072	Topsil 36-520	Wackers 30661-6	TI Lopex L1092
In	n.d.	n.d.	n.d.	n.d
Mn	n.d.	$\sim 2 \times 10^{12}$	n.d.	n.d.
Mo	$\sim 4 \times 10^{12}$	n.d.	n.d.	n.d.
Cu	2.9×10^{12}	$\sim 7 \times 10^{11}$	1.1×10^{12}	1.3×10^{12}
Ga	n.d.	n.d.	n.d.	n.d.
Au	4.7×10^{9}	n.d.	5.3×10^{9}	$\sim 3 \times 10^{9}$
As	n.d.	n.d.	n.d.	n.d.
Sb	n.d.	n.d.	n.d.	n.d.
Yb	n.d.	n.d.	n.d.	n.d.
Na	8.9×10^{13}	2.0×10^{13}	1.8×10^{13}	1.9×10^{13}
Eu	n.d.	n.d.	n.d.	n.d.
Cr	n.d.	n.d.	n.d.	n.d.
Th	n.d.	n.d.	n.d.	n.d.
Sc	n.d.	n.d.	n.d.	n.d.
Hf	n.d.	n.d.	n.d.	n.d.
Co	n.d.	n.d.	n.d.	n.d.
Ag	n.d.	n.d.	n.d.	n.d.
Ta	n.d.	n.d.	n.d.	n.d.
W	n.d.	n.d.	n.d.	n.d.

*n.d. indicates not detected concentrations above the background. Detection limits are given in Table 9.

assuming that the impurity is homogeneous in the matrix. The values given for sodium probably represent surface contamination derived from the ^{27}Al (n, α) ^{24}Na reaction occurring in the aluminum foil encapsulation.

Figure 34 illustrates a sawing contamination which was detected on VZ-072. This sample was cut on a glass cut-off tool outside our laboratories. It is apparent that gold surface contamination was present and was difficult to remove by etching. The etching procedure apparently tends to selectively etch around the gold spots and undercut until the gold is removed.

C. Irradiation and Annealing Experiments

It is instructive at this point to consider the types and amounts of radiation damage which result from a typical neutron transmutation irradiation. We will consider the following sources of damage:

- Fast neutron damage for a graphite moderated neutron energy spectrum (this case will be an approximation to our sample irradiation position).
- Fast neutron damage from a fission neutron energy spectrum (this case will approximate in-pile irradiations found in the literature).
- Gamma damage from fission gammas from the reactor pile.
- Gamma recoil damage (this damage occurs as a result of conservation of momentum when a gamma is emitted from an excited Si nucleus after thermal neutron capture).

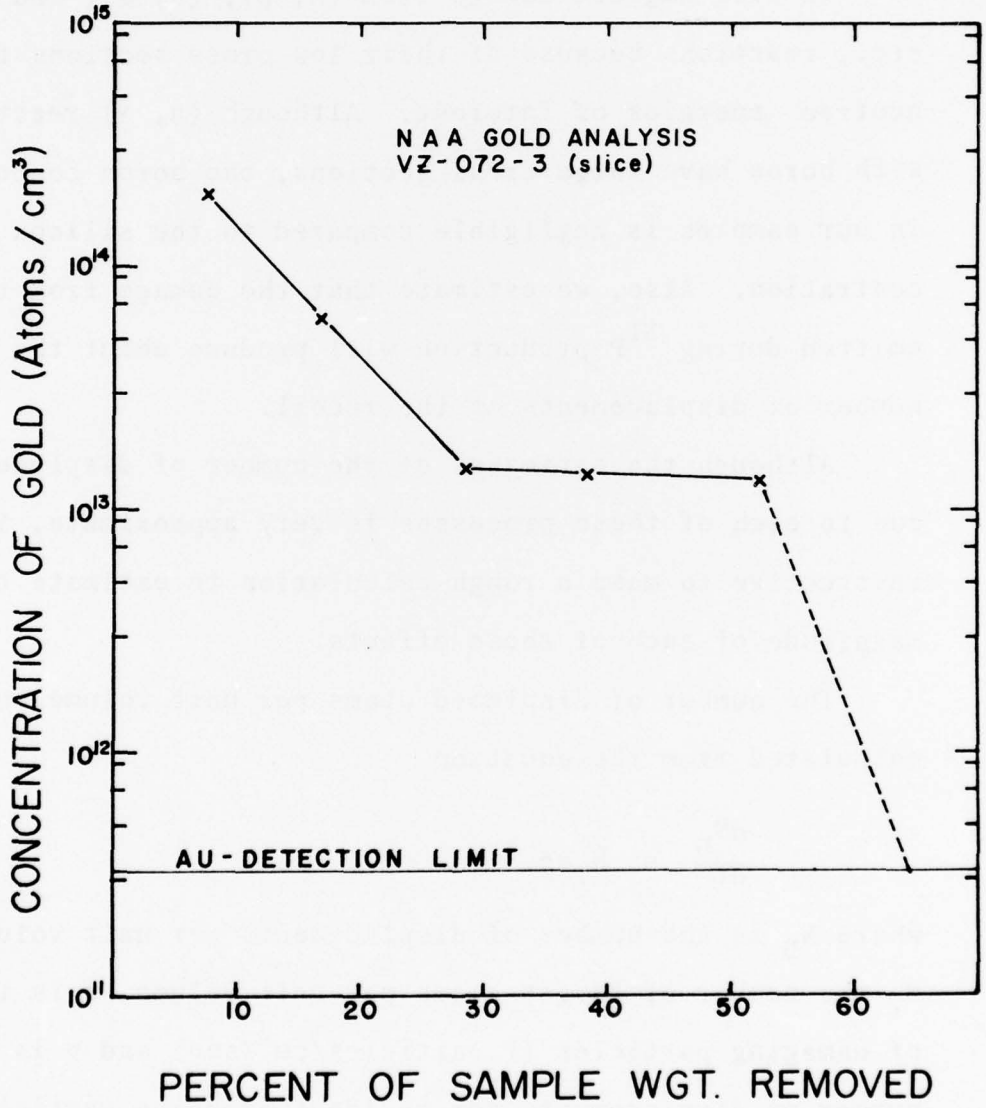

Figure 34. Concentration of gold vs. percent of sample weight removed.

- Beta recoil damage (this damage occurs as a result of conservation of momentum when the beta is emitted in the deexcitation of $^{30}Si \rightarrow {}^{31}P + \beta^-$.

We will neglect damage from (n, p), (n, α), and (γ, n) etc., reactions because of their low cross sections for neutron energies of interest. Although (n, γ) reactions with boron have large cross sections, the boron concentration in our samples is negligible compared to the silicon concentration. Also, we estimate that the damage from the β^- emitted during ^{31}P production will produce about the same number of displacements as the recoil.

Although the estimates of the number of displacements due to each of these processes is very approximate, it is instructive to make a rough calculation to estimate the magnitude of each of these effects.

The number of displaced atoms per unit volume per sec is calculated from the equation

$$\frac{dN_D}{dt} = N_T \sigma \phi \nu \tag{26}$$

where N_D is the number of displacements per unit volume, N_T the number of target atoms per unit volume, ϕ is the flux of damaging particles (# particles/cm^2/sec) and ν is the number of displacements per incident damaging particle. We will estimate ν from the Kinchin-Pease model.[31] In this model

$$\nu(E_R) = \bar{E}_R/2E_d \tag{27}$$

for $\bar{E}_R \gg 2E_d$ where $\bar{E}_R$ is the average kinetic energy of the recoiling lattice atom and E_d is the displacement threshold in silicon which we take as about 12 eV.[32] The maximum recoil kinetic energy of a target atom struck by a neutron of energy E_n is given by

$$E_R(\max) \cong \frac{4E_n}{A} \tag{28}$$

when A is the target material atomic weight.[33]

For a fission neutron spectrum, the average recoil kinetic energy is given by[33]

$$\bar{E}_{R(\text{fission neutron})} = \frac{E_R\ (\max)}{2} \tag{29}$$

while for a graphite moderated spectrum

$$\bar{E}_R\ (\text{moderated neutron}) = \frac{1/2\ E_R(\max)}{\ln\left[\frac{E_R(\max)}{E_d}\right]} . \tag{30}$$

We shall assume that the average neutron energy to be used in equation (28) is 1.5 MeV. Then we find from (28), (29), and (30) that

$$E_R(\max) = \frac{4(1.5\ \text{MeV})}{28} = 214\ \text{keV},$$

$$\bar{E}_R(\text{fission neutron}) = \frac{214\ \text{keV}}{2} = 107\ \text{keV}$$

and

$$\bar{E}_R\ (\text{moderated neutron}) = \frac{1/2(214\ \text{keV})}{\ln\left[\frac{214 \times 10^3\ \text{eV}}{12\ \text{eV}}\right]} = 10.9\ \text{keV}.$$

We find, using (27), that the number of displacements per neutron is much higher for a fission spectrum than for a moderated spectrum, i.e.,

$$\nu(\text{fission}) = \frac{107\ \text{keV}}{2(12\ \text{eV})} = 4458\ \text{displacements/neutron} \quad (31)$$

and

$$\nu(\text{moderated}) = \frac{10.9\ \text{keV}}{2(2\ \text{eV})} = 455\ \text{displacements/neutron.} \quad (32)$$

Furthermore, in our bulk pool facility, assuming a Cd ratio of about 30:1, the fast flux is about $(5 \times 10^{11} n/cm^2/sec)/30 = 1.67 \times 10^{10} n/cm^2/sec$. For an in-core irradiation, the Cd ratio is about 1:1 and a typical fast flux is, therefore, $5 \times 10^{13} n/cm^2/sec$. Using these fluxes and assuming that the displacement cross section is approximately equal to the scattering cross section,[33] which we will assume is 3×10^{-24} cm^2, we find using (26) and (31)

$$\frac{dN_D}{dt}\ (\text{fast neutron in-core}) = (5 \times 10^{22})(3 \times 10^{-24})(4458) \times (5 \times 10^{13}) = 3.35 \times 10^{16}\ \text{displacements/cm}^3\text{/sec.} \quad (33)$$

Using (26) and (32) we find also that

$$\frac{dN_D}{dt}\ (\text{fast neutron in-pool}) = (5 \times 10^{22})(3 \times 10^{-24})(455) \times (1.67 \times 10^{10}) = 1.14 \times 10^{12}\ \text{displacements/cm}^3\text{/sec.} \quad (34)$$

The gamma flux radiation damage is also quite different since in core the photon flux is about 3×10^6 R/sec while in our bulk pool facility it is about 3×10^2 R/sec. The cross section, $\sigma(\gamma)$, for displacements is dominated by Compton electron displacements and is nearly independent of photon energy in silicon for typical fission gamma energies.[33,34] We will assume that this cross section is about 1×10^{-25} cm^2 for 100 keV < E_γ < 2 MeV and that 1 R/sec = 2×10^9 1 MeV photons/cm^2/sec.[35] Then the number of displacements is

$$\frac{dN_D}{dt} \text{ (gamma in pile)} = (5 \times 10^{22})(1 \times 10^{-25})(3 \times 10^{6}) \times (2 \times 10^{9}) = 3 \times 10^{13} \text{ displacements/cm}^3\text{/sec} \quad (35)$$

and

$$\frac{dN_D}{dt} \text{ (gamma bulk pool)} = (5 \times 10^{22})(1 \times 10^{-25})(3 \times 10^{2}) \times (2 \times 10^{9}) = 3 \times 10^{9} \text{ displacements/cm}^3\text{/sec.} \quad (36)$$

The various silicon isotopes after thermal neutron absorption relax from excited states by prompt gamma emission. This imparts a recoil to the silicon isotope in order to conserve momentum. Since

$$p = \frac{E_\gamma}{c} \equiv MV,$$

$$E_R = (1/2)MV^2 = 1/2 \; \frac{E_\gamma^{\;2}}{Mc^2} \; .$$

An average over all silicon isotopes and cross sections yields an average recoil kinetic energy of 780 eV.[37,38] Therefore, using (27), we find

$$\bar{\nu} = \frac{780 \text{ eV}}{2(12 \text{ eV})} = 32.5 \text{ displacements/thermal neutron.}$$

The average cross section for these processes[37] is 1.3×10^{-25} cm^2. The flux of interest is the thermal neutron flux, therefore

$$\frac{dN_D}{dt} (\gamma \text{ - recoil in core}) = (5 \times 10^{22})(1.3 \times 10^{-25})(5 \times 10^{13}) \times (32.5) = 1.06 \times 10^{13} \text{ displacements/cm}^3\text{/sec} \quad (37)$$

and

$$\frac{dN_D}{dt} (\gamma\text{-recoil in pool}) = (5 \times 10^{22})(1.3 \times 10^{-25})(5 \times 10^{11}) \times (32.5) = 1.06 \times 10^{11} \text{ displacements/cm}^3\text{/sec.} \quad (38)$$

A similar procedure can be applied to beta decay recoil. Assuming the beta energy to be $E_\beta = 1.5$ MeV, and using conservation of momentum, we find

$$P = \frac{\sqrt{E_\beta^{\,2} - (m_o c^2)^2}}{c} = MV$$

$$\overline{E}_R = (1/2)MV^2 = 1/2\left[\frac{E_\beta^{\,2} - (m_o c^2)^2}{Mc^2}\right] = 33.2 \text{ eV.}$$

Therefore, using (27),

$$\nu = \frac{33.2 \text{ eV}}{2(12 \text{ eV})} = 2.76 \text{ displacements/neutron absorbed.}$$

Since this occurs for only 3% of the total silicon atoms, with a cross section of $1.1 \times 10^{-25} \text{cm}^2$,

$$\frac{dN_D}{dt} (\beta \text{ recoil in core}) = (0.03)(5 \times 10^{22})(1.1 \times 10^{-25}) \times (5 \times 10^{13})(2.76) = 2.3 \times 10^{10} \text{ displacements/cm}^3\text{/sec} \tag{39}$$

and

$$\frac{dN_D}{dt} (\beta \text{ recoil in pool}) = (0.03)(5 \times 10^{22})(1.1 \times 10^{-25}) \times (5 \times 10^{11})(2.76) = 2.3 \times 10^{8} \text{ displacements/cm}^3\text{/sec.} \tag{40}$$

These numbers must be compared with the rate of producing phosphorus atoms which is

$$\frac{dN_P}{dt} (\text{in core}) = (0.03)(5 \times 10^{22})(1.1 \times 10^{-25})(5 \times 10^{13}) = 8.25 \times 10^{9} \text{ [P]/cm}^3\text{/sec.} \tag{41}$$

and

$$\frac{dN_P}{dt} (\text{in pool}) = (0.03)(5 \times 10^{22})(1.1 \times 10^{-25})(5 \times 10^{11})$$

$$= 8.25 \times 10^7 [P]/cm^3/sec. \quad (42)$$

We can now compare the number of displacements per phosphorus atom produced by each of these mechanisms. This information is summarized in Table 11.

Although these calculations are quite speculative, several differences between in-core (low Cd ratio) and in-pool (high Cd ratio) irradiations become apparent. It is clear that the fission gamma and beta recoil damage is point-defect like. The annealing characteristics of this damage should be similar to 1 MeV electron irradiation annealing. It is also clear that the gamma recoil damage is a significant fraction of the radiation damage for in-pool irradiations but is relatively less significant for in-core irradiations.

Chukichev and Vavilov have estimated experimentally that the number of gamma recoil displacements is about equal to the number of fast neutron displacements in a heavy water moderated reactor.[37] Our ratio of fast neutron to gamma recoil displacements is of the order of 10:1 for an in-pool position with a Cd ratio of 30:1. Since the Cd ratio in a heavy water reactor is between 100:1 to 1000:1, our calculations are in reasonable agreement with the experimental data in Ref. 37.

It is not clear whether to treat the gamma recoil radiation damage as point defect like or cluster like. The average number of displacements per neutron is rather large (32.5 displacements/thermal neutron) and suggests at least

TABLE 11. Number of Displacements per Phosphorus Produced.

Position → / Damage Particle ↓	In Core $\phi_{th} = 5 \times 10^{13} n/cm^2/sec$ Cd ratio = 1:1	In Pool $\phi_{th} = 5 \times 10^{11} n/cm^2/sec$ Cd ratio = 30:1
Fast Neutron	4.06×10^6	1.38×10^4
Fission Gamma	3.64×10^3	36.4
Gamma Recoil	1.29×10^3	1.29×10^3
Beta Recoil	2.76	2.76
Total Disp./ [P]	4.06×10^6	1.51×10^4
Cluster/Pt. Defect Ratio:		
(If gamma recoil = cluster)	1115	385
(If gamma recoil = pt. defect)	823	10.4

Ratio of Core to Pool Cluster to Pt. Defect Ratios:	
(Gamma recoil = cluster)	2.9
(Gamma recoil = pt. defect)	79.1

the production of small clusters. The actual number of displacements per thermal neutron absorbed, however, ranges from about 10 or 20 up to 80 to 160. There is, therefore, a continuous distribution of cluster sizes which approach the point defect distributions at the lower end. The same cluster size arguments can be made about fast neutron damage from a highly moderated energy spectrum.

We have considered gamma recoil damage both as cluster like and point defect like in Table 11, to calculate the ratio of cluster like displacements to point defect like displacements for our two cases of interest. It seems likely that the in-core irradiations deposit 3 to 80 more displacements in clusters than in point defects as compared to in-pool irradiations. Such a large difference in the defect spectrum is very likely to produce differences in annealing characteristics for the two cases. We will discuss some of these differences in the following discussion on annealing.

Table 12 is a summary of all the irradiations performed thus far, the sample number, the fluence, the phosphorus concentration added by irradiation as calculated from the cross section, and initial resistivity assuming a typical mobility, and the purpose of the irradiation. In this table, Φ_c is the fluence required to take the particular p-type sample from its initial resistivity to intrinsic (or exact compensation of the residual boron by the phosphorus added).

TABLE 12. Summary of Irradiations (undoped material).

Irrad. No.	Sample No.	Position	Integrator Counts	Fluence (n/cm^2) Theoretical [P] Added	Purpose/Result
1	Monsanto FZ ρ_o = 749Ω-cm p-type	RSAF 12-16	Counts not recorded (operator error)	$\sim 1.26 \times 10^{16}$ [0.042 ppb]	Calibration of integrator/30 min anneal at 745°C, ρ_f = 763.5 Ω-cm p-type
1A	"	I-2 (wrong position, operator error)			2nd irradiation of previous sample
2A	MURR 1 Rockwell	RSAF 12-16	7000	1.298×10^{16} (fluxwire) [0.0435 ppb]	$\Phi = 0.54\ \Phi_c$ (Φ_c = fluence needed to intrinsic) Argon isochronal anneal - type converted
2B	MURR 2 Rockwell	"	7000	1.315×10^{16} (fluxwire) [0.0441 ppb]	$\Phi = 0.5\ \Phi_c$ Vacuum isochronal anneal type converted
3	MURR 7 Rockwell	"	? can floated	0.931×10^{16} (fluxwire) [0.0313 ppb]	$\Phi \cong 0.5\ \Phi_c$, argon isochronal anneal to measure minority carrier lifetime
4	MURR 8 Rockwell	"	2181	4.004×10^{15} [0.0134 ppb]	$\Phi \cong 0.4\ \Phi_c$, argon anneal type converted
5	MURR 9 Rockwell	"	2144	3.363×10^{15} [0.0113 ppb]	$\Phi = 0.366\ \Phi_c$, activation analysis
7	Fluxwires	"	2000	3.733×10^{15}	Comparison of NBS and Cohn flux wires
8A	MURR 16 Topsil	"	3899	6.116×10^{15} [0.0205 ppb]	$\Phi = 0.384\ \Phi_c$, argon anneal type converted
8B	MURR 18 T.I.	"	3899	6.116×10^{15} [0.0205 ppb]	$\Phi = 0.373\ \Phi_c$, argon anneal type converted

TABLE 12. Summary of Irradiations (undoped material) Cont.

Irrad. No.	Sample No.	Position	Integrator Counts	Fluence (n/cm^2) Theoretical [P] Added	Purpose/Result
9A	MURR 19 Topsil	"	3899	6.116×10^{15} [0.0205 ppb]	$\Phi = 0.400\ \Phi_c$, vacuum anneal type converted
9B	MURR 20 T.I.	RSAF 12-16	3899	6.116×10^{15} [0.0205 ppb]	$\Phi = 0.421\ \Phi_c$, vacuum anneal type converted
10A	MURR 16 Topsil	I-2	6880	[0.7893 ppb]	2nd irradiation to produce 114.06 Ω-cm argon anneal, final observed value = 115.64 Ω-cm
10B	MURR 3 Rockwell	I-2	6880	[0.7893 ppb]	2nd irradiation to produce 122.84 Ω-cm argon anneal, final observed value = 134.03 Ω-cm
11	MURR 22 Wacker	RSAF 12-16	1266	1.986×10^{15} [0.00666 ppb]	$\Phi = 0.538\ \Phi_c$, vacuum annealed type converted
12	MURR 27 Topsil	"	10085	1.582×10^{16} [0.0531 ppb]	$\Phi = 1.02\ \Phi_c$, argon anneal, expected and final resistivities are equal
13	MURR-28 Monsanto FZ	I-2		Approx 20 Ω-cm(N)	n-type wafer; to check type after irradiation. (not completed)
14	MURR-30 Rockwell	RSAF 12-16	19530	Approx 1000 Ω-cm(N)	To establish limits on n-type side
15	MURR 29	"	6955	Approx 5000 Ω-cm(N)	To establish limits on n-type side

TABLE 12. Summary of Irradiations (undoped material) Cont.

Irrad. No.	Sample No.	Position	Integrator Counts	Fluence (n/cm^2) Theoretical [P] Added	Purpose/Result
16	MURR-31 Rockwell	"	3651	5.75×10^{15}	Furnace test
17	MURR-32 Rockwell	"	3555	5.681×10^{15}	Furnace test
18	MURR-33 Rockwell	"	3436	5.390×10^{15}	Furnace test
19	MURR-34 Rockwell	"	3383	5.381×10^{15}	Furnace test
20	MURR-35 TI	RSAF 12-16	10000	7.791×10^{14} (fast)	Fast neutron radiation damage annealing
21	MURR-36 TI	"	30000	1.194×10^{15} (fast)	Fast neutron radiation damage annealing
23-28	MURR 50-64	Irradiation of Ga doped material, see Table 15			Detector fabrication
31	MURR-66 Rockwell	RSAF 12-16	27790	4.234×10^{16}	[P]/[B] = 10, $\rho(x)$
34	MURR-70 Rockwell	RSAF 12-16	2565	3.975×10^{15} estimated	[P]/[B] = 1.12, $\rho(x)$

TABLE 12. Summary of Irradiations (undoped material) Cont.

Irrad. No.	Sample No.	Position	Integrator Counts	Fluence (n/cm^2) Theoretical [P] Added	Purpose/Result
36	MURR-79 Rockwell	"	5000	7.75×10^{15} estimated	[P]/[B] = 2.04, ρ(x)
37	MURR-80 Rockwell	"	7493	1.161×10^{16} estimated	[P]/[B] = 3.52, ρ(x)
38	MURR-81 Rockwell	"	12552	1.946×10^{16} estimated	[P]/[B] = 4.45, ρ(x)

An inspection of this table shows immediately the failure to control the resistivity for partial compensation on the p-type side of intrinsic (i.e. $\Phi < \Phi_c$) due to premature type conversion.

Figure 35 shows this premature type conversion effect. This figure compares an isochronal anneal in argon of a wafer of Rockwell float zone, MURR 1, with the annealing in air of a piece of Monsanto Czochralski, and vacuum anneals of float zone and Czochralski by Kharchenko et al.[38,39] The solid bar is the expected p-type resistivity for the Rockwell float zone after the final anneal on the basis of the number of donors added [0.042 ppb]. Instead the final resistivity is about 400 Ω-cm n-type (the type conversion probably occurred between 600 and 800°C) a gain of extra donors of 0.282 ppb (1.41×10^{13} atoms/cm^3) beyond that added by neutron doping [0.042 ppb].

Also shown on this figure is the isochronal annealing of a second unirradiated Rockwell sample from the same wafer. It should be noted that the unirradiated sample shows no adverse effects of the annealing and that the resistivity of the irradiated sample MURR 1 drops below that of the unirradiated sample at 300°C.

The heavily irradiated float zone sample by Kharchenko shows no type conversion peaks, i.e., no rise in resistivity toward intrinsic (230,000 Ω-cm). This is confirmed by their Hall measurements directly after irradiation but before

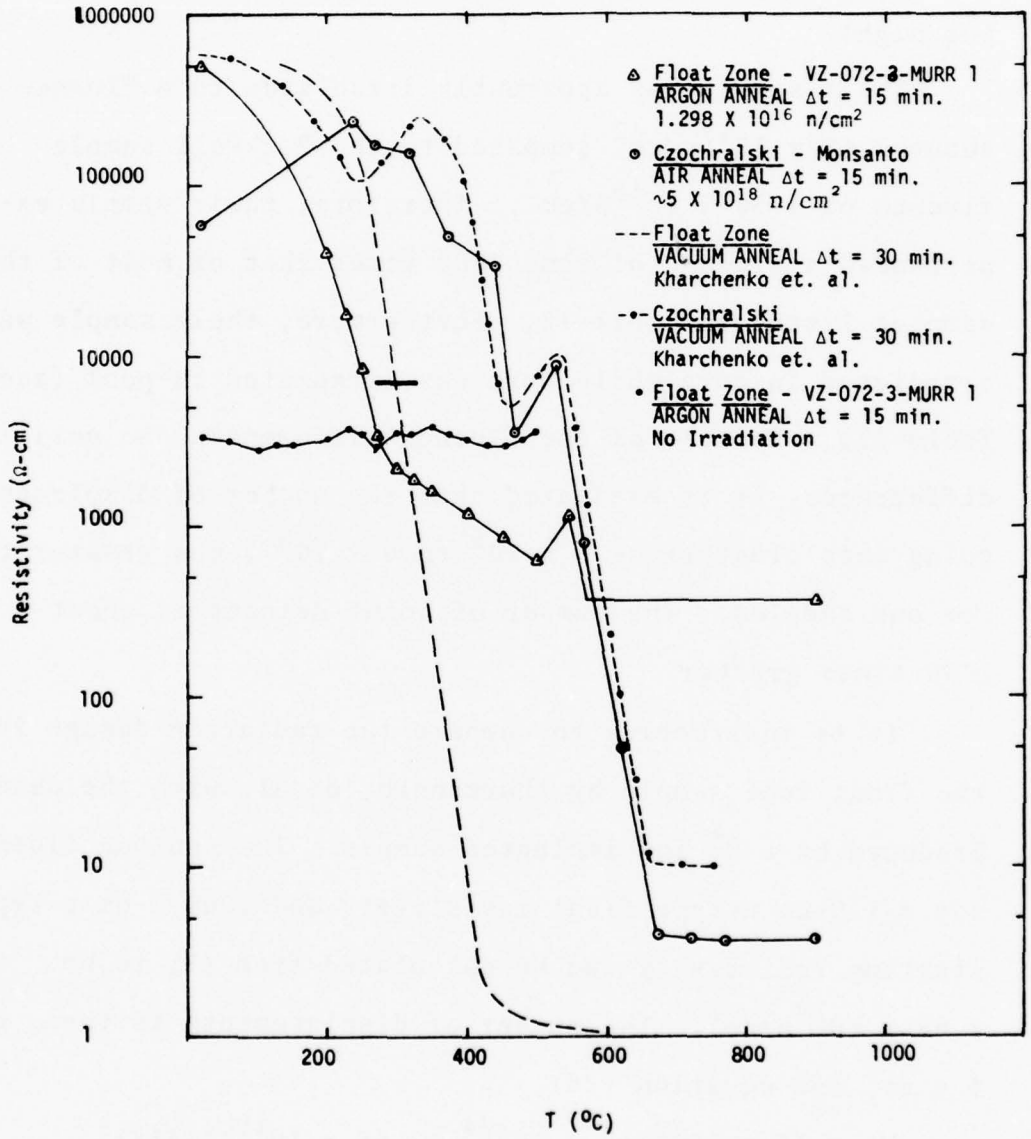

Figure 35. A comparison of isochronal annealing of transmutation doped float zone and Czochralski silicon.

annealing. It should be noted that a drafting error has apparently been made in Figure 1 of Ref. 39 since the final values of $n = 5 \times 10^{13} cm^{-3}$ and $\rho = 1\ \Omega$-cm imply an electron mobility of 125,000 cm^2/V-sec, some two orders of magnitude too high!

Their sample was apparently irradiated to a fluence of about $2.68 \times 10^{19} n/cm^2$ compared to the Rockwell sample fluence of $1.30 \times 10^{16} n/cm^2$. Therefore, their sample experienced a fluence of some 2000 times that of most of the samples listed in Table 12. Furthermore, their sample was irradiated in-core while ours was irradiated in-pool (see Table 11). Because of the fluence differences and position differences, it is estimated that the number of displacements going into clusters is 6×10^5 to 6×10^6 times greater than for our samples. The number of point defects is about 2000 times greater.

It is instructive to compare the radiation damage in the float zone sample by Kharchenko, et al. with the damage produced by a P^+ ion implanted sample. The neutron fluence for a 1 Ω-cm n-type final resistivity and 1000 Ω-cm p-type starting resistivity can be calculated from (7) to be $2.68 \times 10^{19} n/cm^2$. The number of displacements is then, using $\Phi = \phi t$, and equation (26),

$$N_D = (5 \times 10^{22})(3 \times 10^{-24})(2.68 \times 10^{19})(4458)$$
$$= 1.79 \times 10^{22} \text{ displacements/cm}^3. \qquad (43)$$

Since silicon contains only 5×10^{22} atoms/cm^3, it is

clear that the radiation damage in the Kharchenko sample is approaching the amorphorus condition.

To produce an amorphorus layer by P^+ ion implantation, a dose of about 5×10^{14} ions/cm^2 at 40 keV is required.[40] The number of displacements per ion can be calculated from (27) to yield

$$\nu = \frac{E}{2E_d} = \frac{40 \text{ keV}}{2(12 \text{ eV})} = 1.666 \times 10^3 \text{ disp./ion.}$$

The depth of a 40 keV P^+ implant is about 2×10^{-5}cm because of enhanced diffusion (see Figure 2.27, p. 56 in Ref. 40). The number of displacements is

$$N_d = \frac{(5 \times 10^{14} \text{ ions/cm}^2)(1.667 \times 10^3 \text{ displacements/ion})}{2 \times 10^{-5}\text{cm}}$$

$$= 4 \times 10^{22} \text{ displacements/cm}^3. \qquad (44)$$

We can conclude from a comparison of (43) and (44) that the Kharchenko float zone sample is nearly amorphorus as a result of fast neutron damage.

This conclusion has interesting consequences. In ion-implanted silicon, annealing up to temperatures of about 800°C is required for complete electrical activity of the implanted ion in cases where an amorphorus layer is not formed.[41,42] The recovery of the electrical activity of an amorphorus layer is completed by about 600°C and is closely related to the formation of crystalline films of Si during vacuum evaporation and to epitaxial regrowth.[43] It is reasonable to hypothesize that an epitaxial regrowth of

cluster damage could be completed by 600°C. Further evidence for this hyphothesis will become apparent later.

Figure 35 also shows, for comparison, the isochronal annealing of two Czochralski silicon samples (oxygen concentration $\sim 10^{18} cm^{-3}$). The data for the Kharchenko sample is taken from Ref. 39. The reverse annealing peaks are evident in both Czochralski samples and are apparently related to the high oxygen concentration in these samples and not to neutron fluence since the final resistivities differ.

Evidence for this point of view is shown in Figure 36. These float zone samples (oxygen concentration $\sim 10^{15} cm^{-3}$) were irradiated to a fluence sufficient to produce $\sim$100 Ω-cm n-type. The expected final resistivity values calculated from the starting resistivity are shown on the figure. The Topsil sample came to within 1% of the expected donor concentration while the Rockwell sample was only slightly worse. It should be noted that the fluences for these two samples are similar to the fluences for the Czochralski samples in the previous figure; however, the annealing peaks and dips between 200 and 500°C do not appear in the float zone material at this fluence. Furthermore, dislocation density does not appear to have a direct correlation with the lack of the reverse annealing peaks shown in Figure 35 since the Rockwell sample in Figure 36 is highly dislocated while the Topsil sample is not. We conclude then, on the basis of circumstantial evidence, that the reverse annealing peaks are a result of the concentration of oxygen relative to the level of phosphorus.

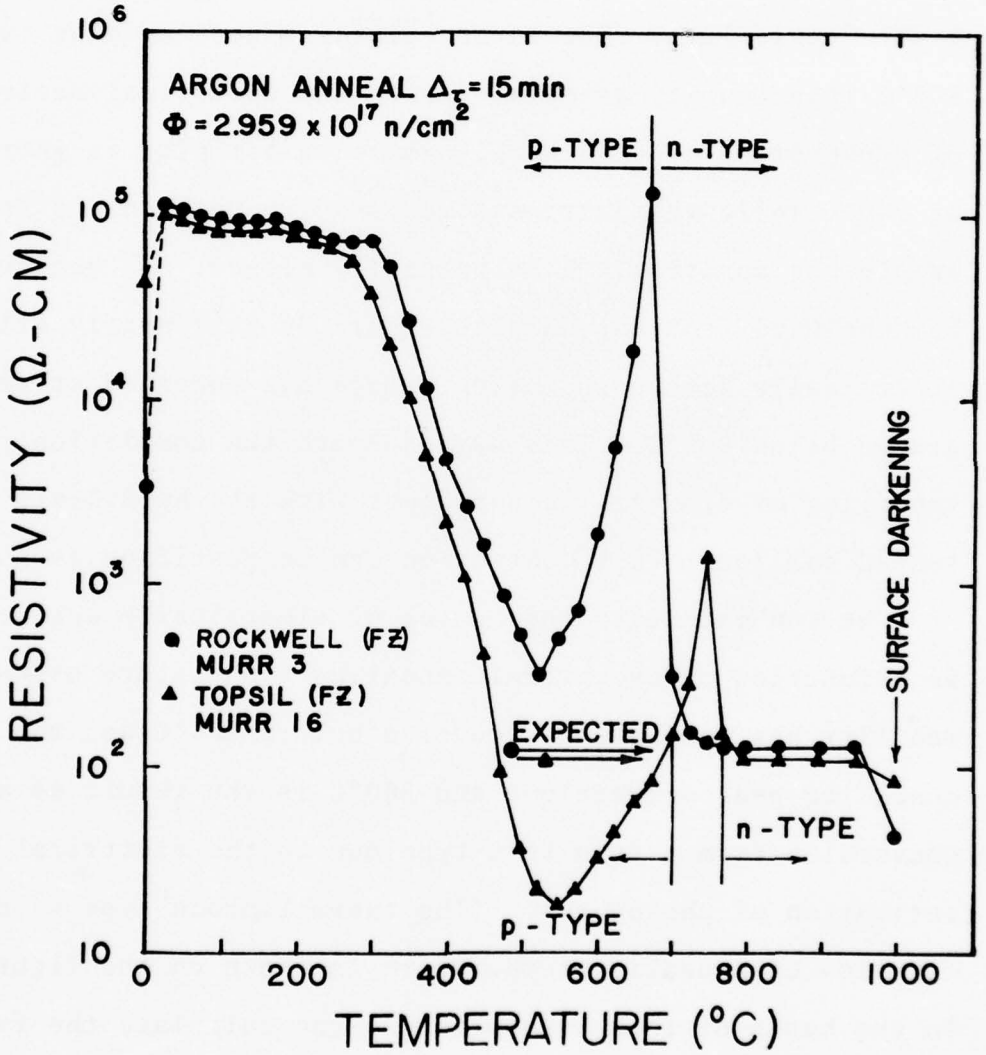

Figure 36. Isochronal annealing of two float zone samples irradiated to produce ∿100 Ω-cm n-type.

Kharchenko et al. also state that their Czochralski samples were p-type up to 600°C and n-type thereafter.[39] (Their Czochralski samples are apparently irradiated in-pool.) We conclude from our data in Figure 36 that electrical activity of the phosphorus begins at about 600°C in agreement with their conclusions. The large reverse annealing peak from 600-800°C is primarily associated with the electrical activation of phosphorus. The Rockwell sample resistivity is intrinsic at 700°C while the intrinsic resistivity peak in the Topsil sample has apparently been partially missed. It can further be concluded from the data in Figure 36 that nearly all the electrically active radiation damage has annealed at temperatures below 600°C. This may indicate the completion of the annealing of clusters in agreement with the hypothesis presented earlier. This contention can be justified as follows.

We can calculate the number of electrically active donors as a function of isochronal annealing temperature assuming the mobility has completely recovered before 600°C and the reverse annealing peak between 600 and 800°C is the result of a type conversion from p-type to n-type due to the electrical activation of phosphorus. (The thermal probe type as a function of annealing temperature is shown on the figure.) On the basis of this assumption we can calculate the fraction of phosphorus which is not electrically active (N/N_o) as a function of annealing temperature. We define that this fraction is unity at the resistivity minimum for normalization purposes. Then if the electrical activation is

governed by first order annealing kinetics,

$$\frac{d(N/N_o)}{dt} = -K(T)(N/N_o)$$

where $K(T) = \nu_o e^{-E/kT}$ is the temperature dependent rate at which the fraction of phosphorus not electrically active decreases at the various annealing temperatures. From the above

$$\ln (N_o/N) = (\nu_o \Delta\tau) e^{-E/kT}$$

where $\Delta\tau$ is the annealing time at temperature T. For equal annealing times at various temperatures, a semilog plot of $\ln N_o/N$ vs. 1/T yields the activation energy for the process while the intercept yields the defect jump frequency.

The result of this first order analysis is shown in Figure 37. It is clear that the first order annealing assumption is reasonable and that the first order annealing occurs throughout the type conversion peak in Figure 36. To have obtained this result, the two assumptions mentioned previously must be valid, i.e., a lack of electrically active damage at temperatures above 600° and the complete recovery of carrier mobility before 600°C.

The first order annealing analysis suggests that the activation energy for the phosphorus to become electrically active is 0.96 $\pm$ 0.05 eV while the jump frequency is about 2×10^2 sec^{-1}. This activation energy is remarkably close to the values given in the literature for the reorientation of the vacancy phosphorus E-center (E = 0.93 $\pm$ 0.05 eV,

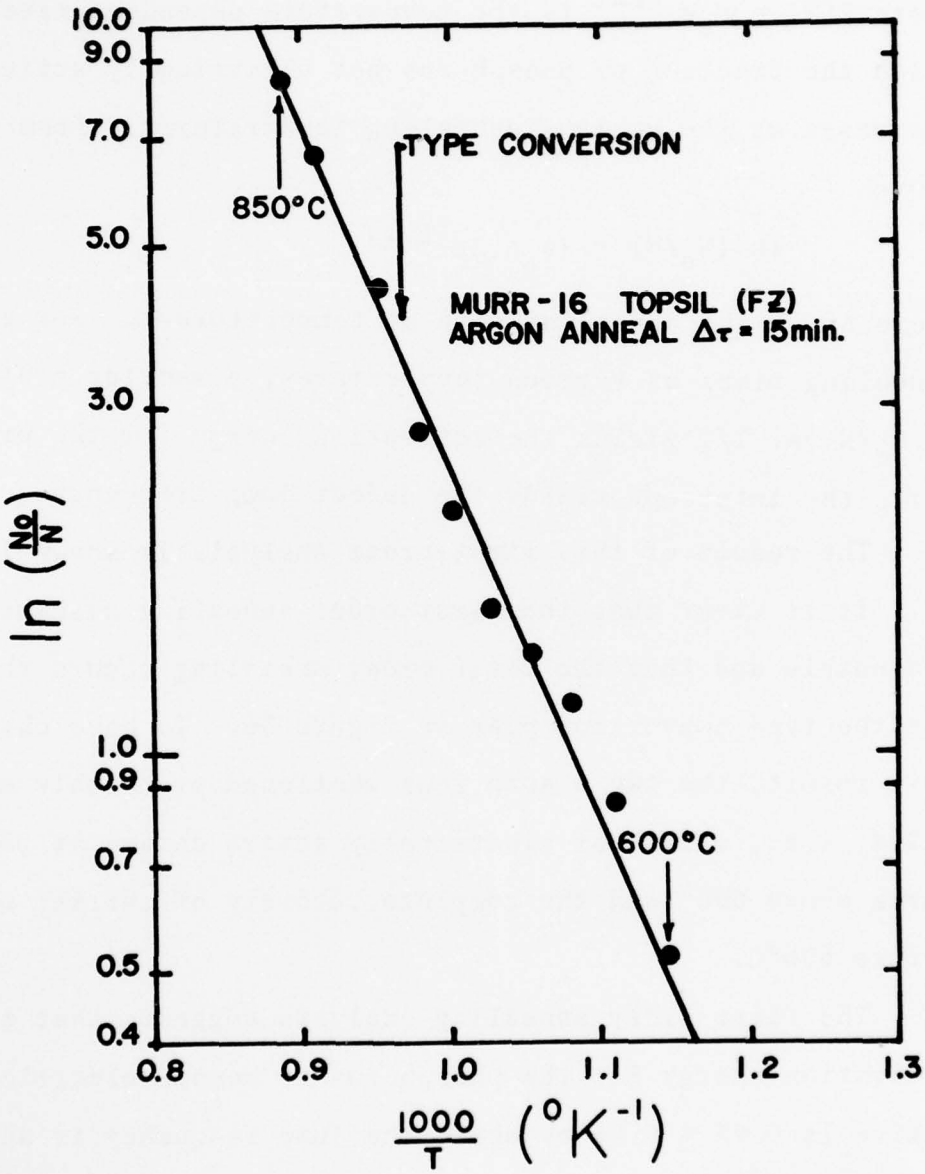

Figure 37. Semilog plot of the ln of the reciprocal of the fraction of phosphorus not electrically active vs. reciprocal annealing temperature for the Topsil sample shown in Figure 36.

$\nu_o = 1.6 \times 10^{13} sec^{-1})$[44] and for the electrical disappearance of a deep acceptor $(E_c - 0.4)$eV thought to be the E-center ($E = 0.94$ eV, $\nu_o = 10^8 sec^{-1}$).[45]

Watkins and Corbett suggest that the lower jump frequency in Ref. 45 indicates the diffusion of the E-center through the lattice over great distances ($10^{13}/10^8 = 10^5$ jumps before dissociation at a vacancy sink). They point out that an E-center reorientation followed by a vacancy phosphorus interchange is equivalent to an E-center jump through the lattice. If we make this same assumption, then we are observing $10^{13}/2 \times 10^2 = 5 \times 10^{10}$ jumps before annihilation! For a random walk of 5×10^{10} jumps of a distance of $\sim 2\mathring{A}$, the mean distance traveled would be

$$L_o = \sqrt{5 \times 10^{10}}\ (2 \times 10^{-8} cm) = 4.5 \times 10^{-3} cm.$$

This is of the order of the smallest sample dimension and would suggest vacancy anihilation at the sample surface. But this can not be the correct mechanism for E-center annihilation because it would deposit all the phosphorus at the sample surface. We know, however, that phosphorus is uniformly distributed in transmutation doped silicon. We must conclude, then, that free migration of E-centers in NTD-Si does not occur for some reason. One possibility is that the E-center becomes pinned in some way to its lattice position by the clustering with other defects. Since there are approximately three displacements per beta emission when

the phosphorus atom is created by transmutation, it is possible that a di-interstitial or di-vacancy, E-center complex is formed which remains stable up to the higher annealing temperatures observed here.

It should be noted in Fig. 36 that at the minimum resistivity near 600°C in the Topsil sample, the hole concentration is about $6 \times 10^{14} cm^{-3}$. Since the initial hole concentration was about 2 or $3 \times 10^{11} cm^{-3}$, we can safely infer that a very large acceptor concentration has been created as a result of irradiation and annealing to 550°C (an alternate interpretation would be the destruction of $6 \times 10^{14} cm^{-3}$ donors but this would imply a compensation ratio of 0.9996 before irradiation which is impossible because of the initial resistivity).

It will be shown shortly that similar acceptor defect concentrations have been observed in all float zone studied to date and that this defect concentration is nearly independent of irradiation fluence over a fluence range of 50:1. We conclude, therefore, that the magnitude of this concentration is dependent on the properties of the silicon before irradiation. The most likely impurity to be found in highly zone refined silicon in a concentration range larger than $3 \times 10^{13} cm^{-3}$ (Rockwell, Wacker) to $5 \times 10^{14} cm^{-3}$ (Topsil and T.I.) is oxygen. We, therefore, suggest that these acceptor defects are single or multiple defect-oxygen complexes, i.e. the oxygen impurity concentration is decorated as a result of the process of radiation damage and annealing to 550°C.

Figure 38 shows the recovery of resistivity and minority carrier lifetime on a Rockwell sample 1" dia x 1" long. The fluence for this irradiation was 50% of that necessary to produce type conversion. The annealing shows several unusual features which are found only in the Rockwell samples and which could possibly be related to the dislocation density. The resistivity between 200°C and 800°C is multivalued. Shortly after removal from the annealing furnace and quenching to room temperature in trichloroethylene, the resistivity is a minimum but rises to the second higher value while storing the sample in the dark. Upon illumination from a tungsten light, the resistivity returns to its t = o value. The resistivity can be cycled any number of times. The reciprocal of the minority carrier lifetime follows the resistivity in general. Very heavy trapping is observed in the same region as the largest change in resistivity. This sample type-converts at about 800°C. It should also be noted that a plateau in the recovery around 300°C is similar to the Czochralski sample annealing seen previously.

In an attempt to determine if sample contamination is responsible for the unexpected type conversion, a series of isochronal anneals were performed in argon and a vacuum of 5×10^{-7} torr. The fluences for these irradiations were in the range of $\Phi = 0.36\ \Phi_c$ to $\Phi = 0.56\ \Phi_c$ where Φ_c is the fluence required for exact compensation. The results are shown in Figures 39 through 45. A comparison of a pair of

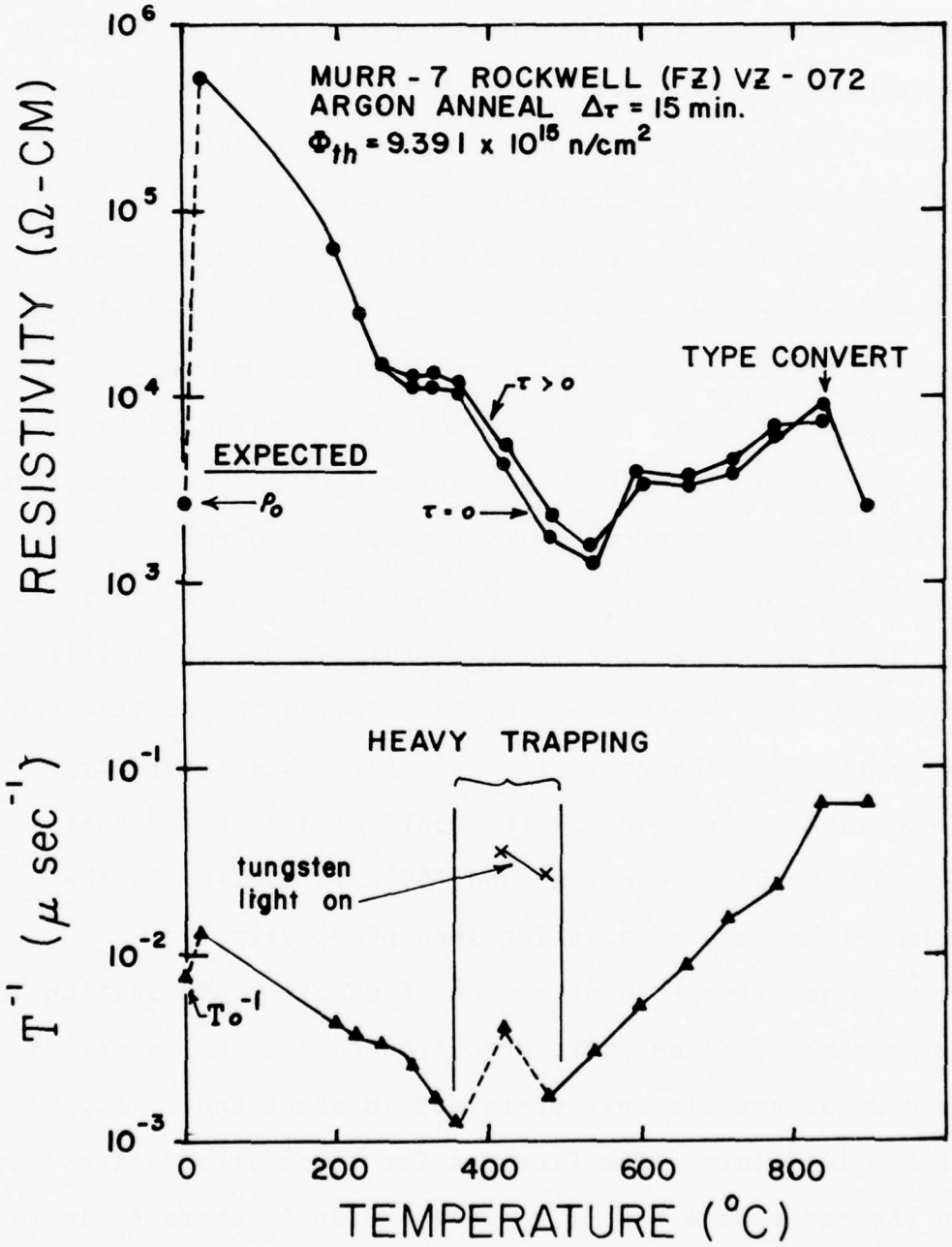

Figure 38. Isochronal annealing of resistivity and minority carrier lifetime of Rockwell float zone (argon anneal) bulk sample.

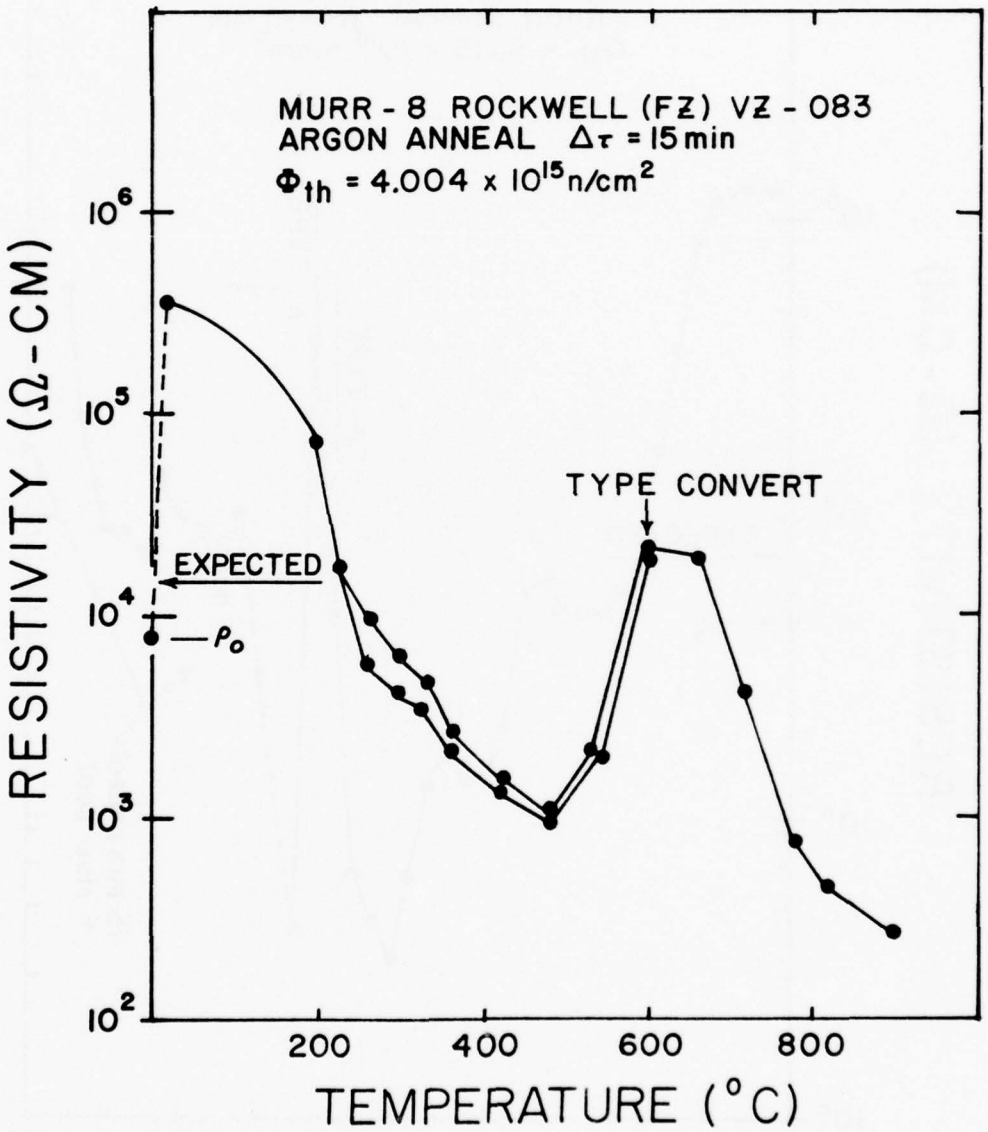

Figure 39. Argon isochronal anneal of Rockwell float zone wafer.

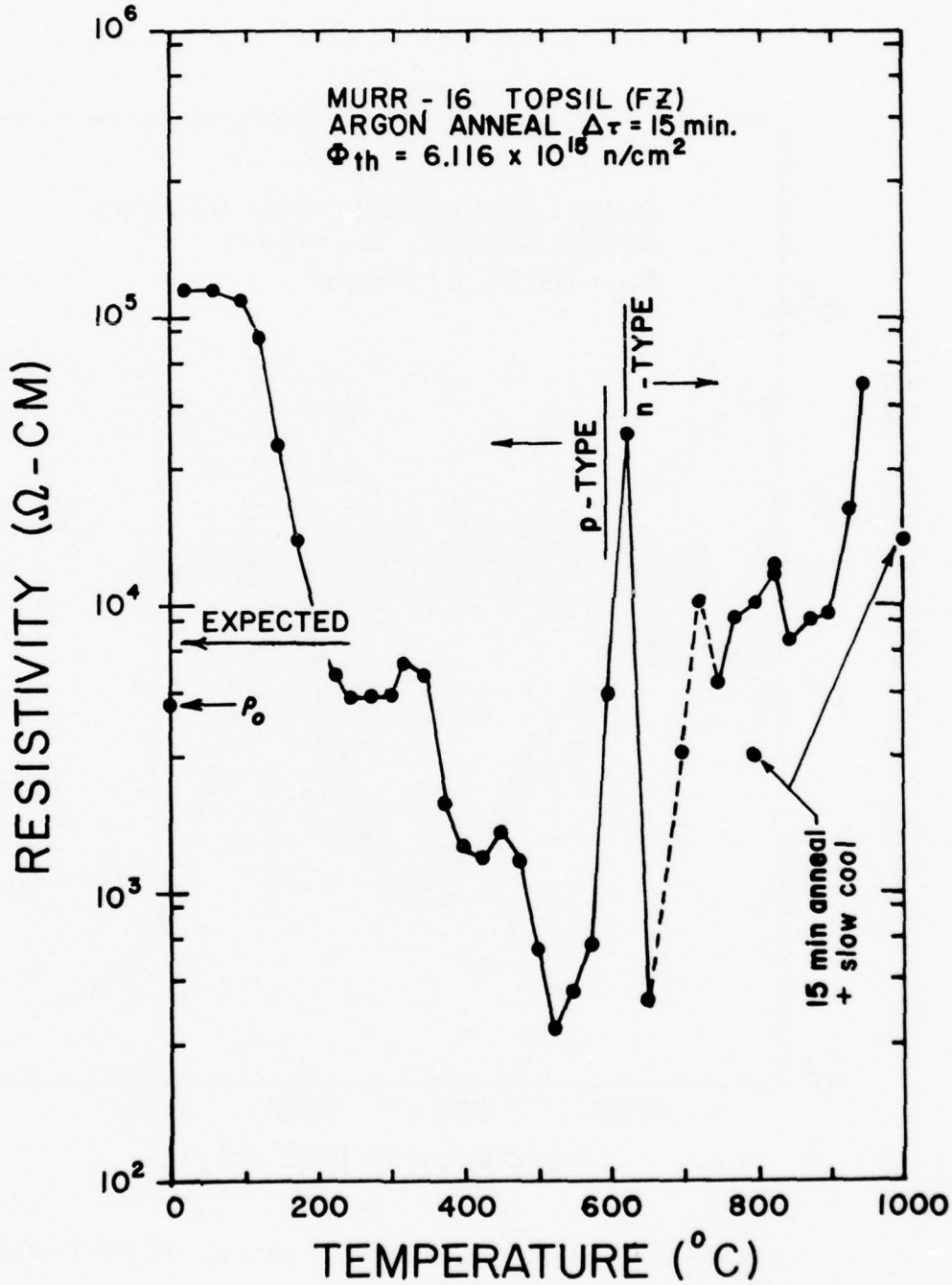

Figure 40. Argon isochronal anneal of Topsil wafer.

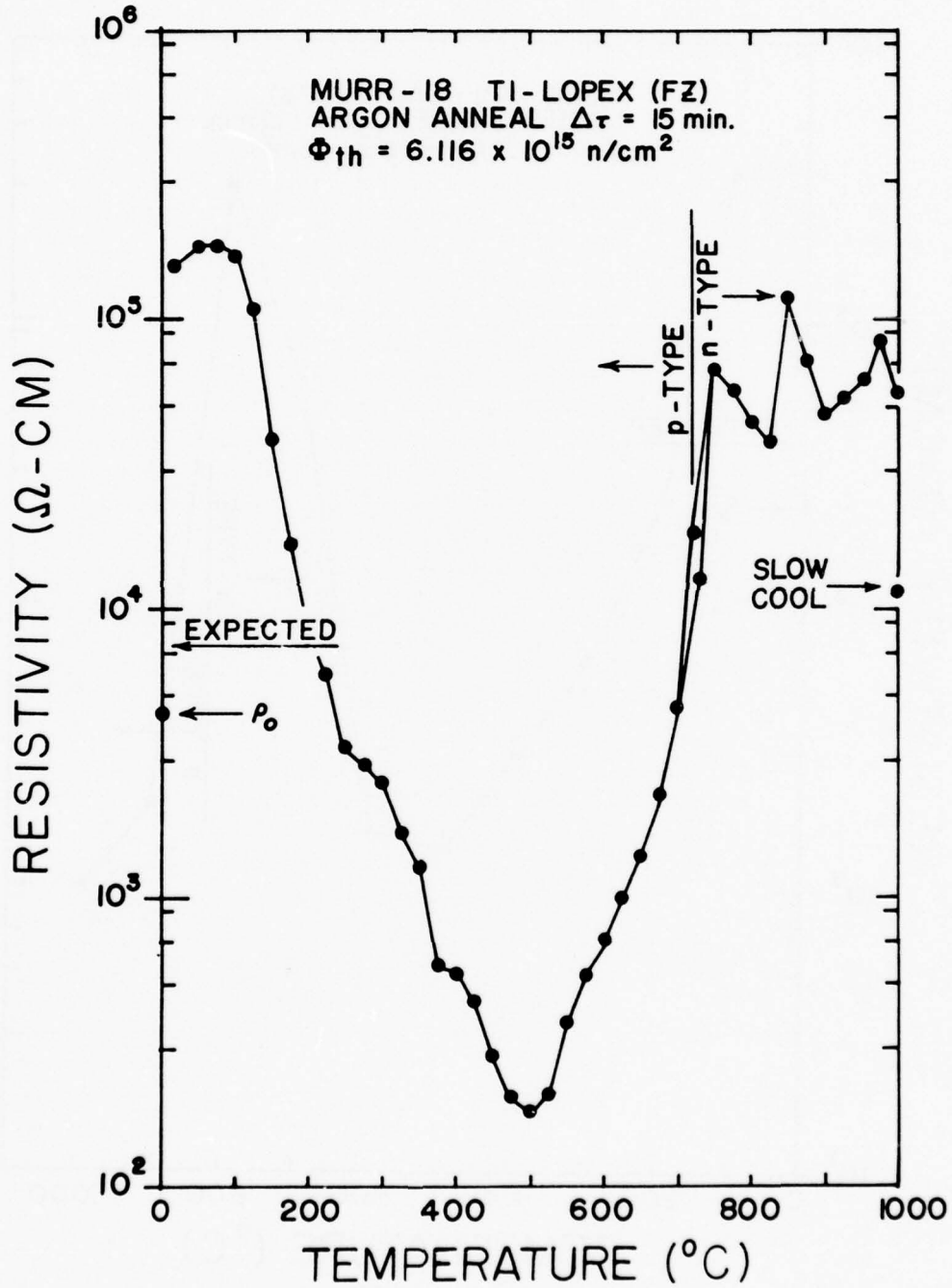

Figure 41. Argon isochronal anneal of T.I. Lopex wafer.

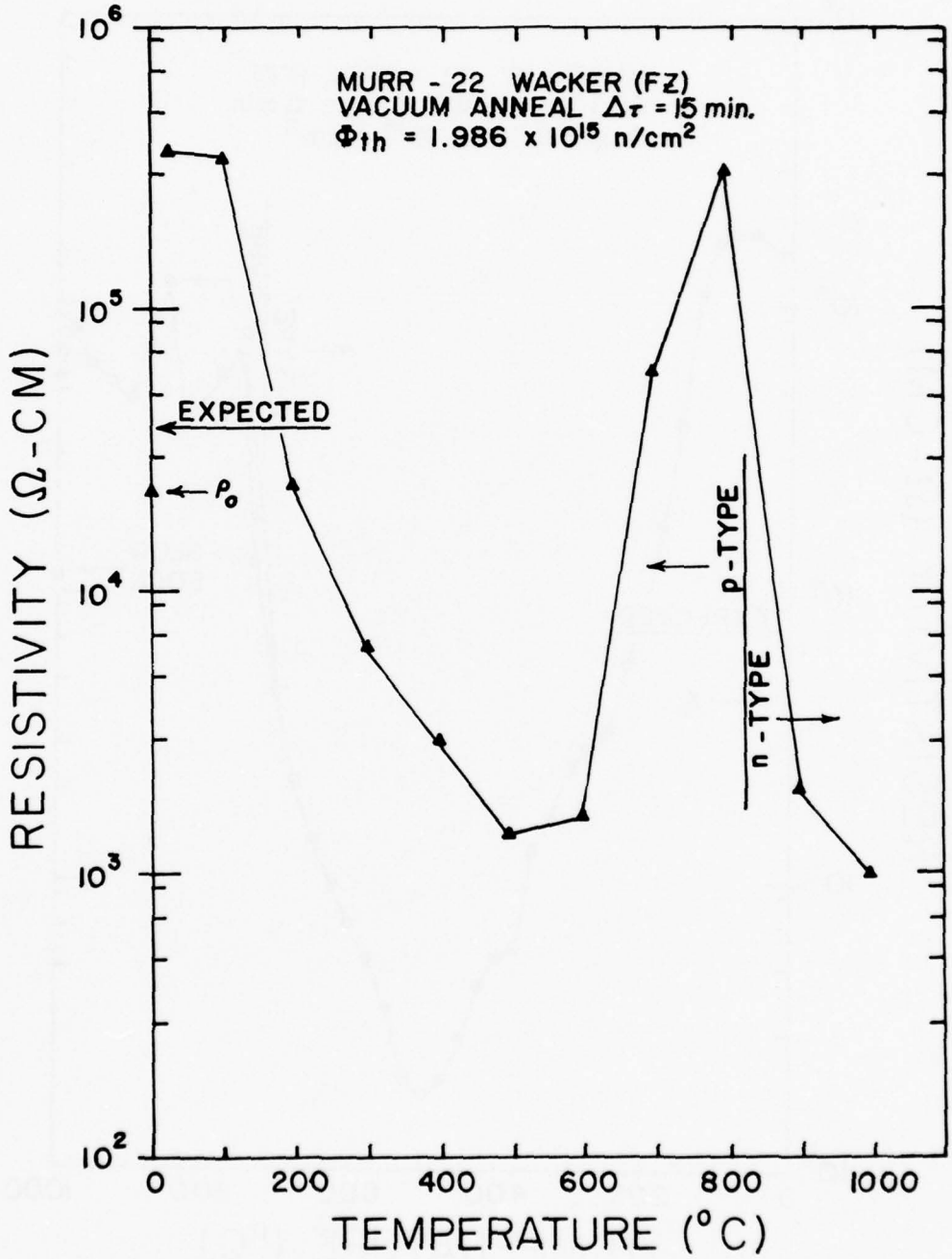

Figure 42. Vacuum isochronal anneal of Wacker wafer.

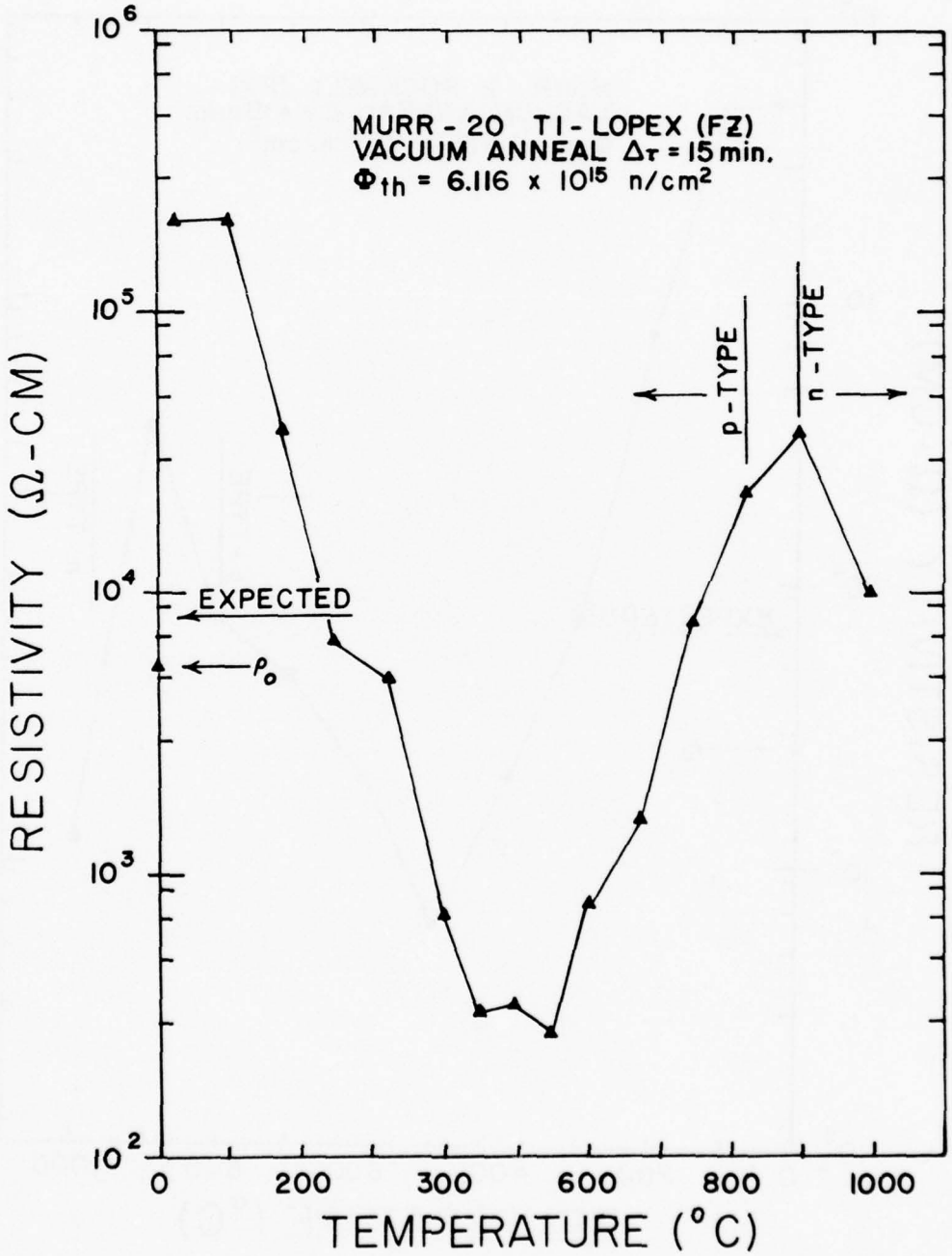

Figure 43. Vacuum isochronal anneal of T.I. Lopex wafer.

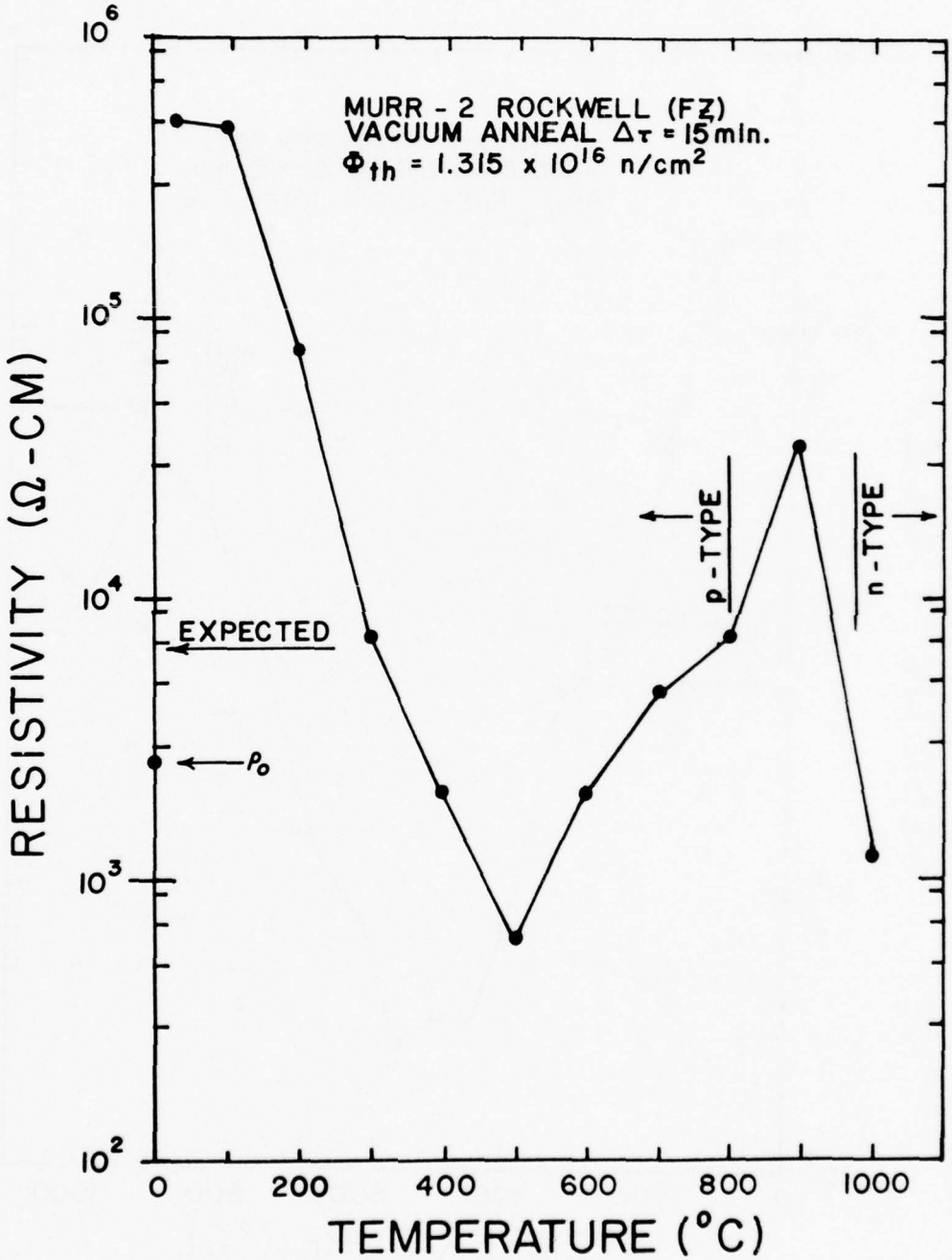

Figure 14. Vacuum isochronal anneal of Rockwell wafer.

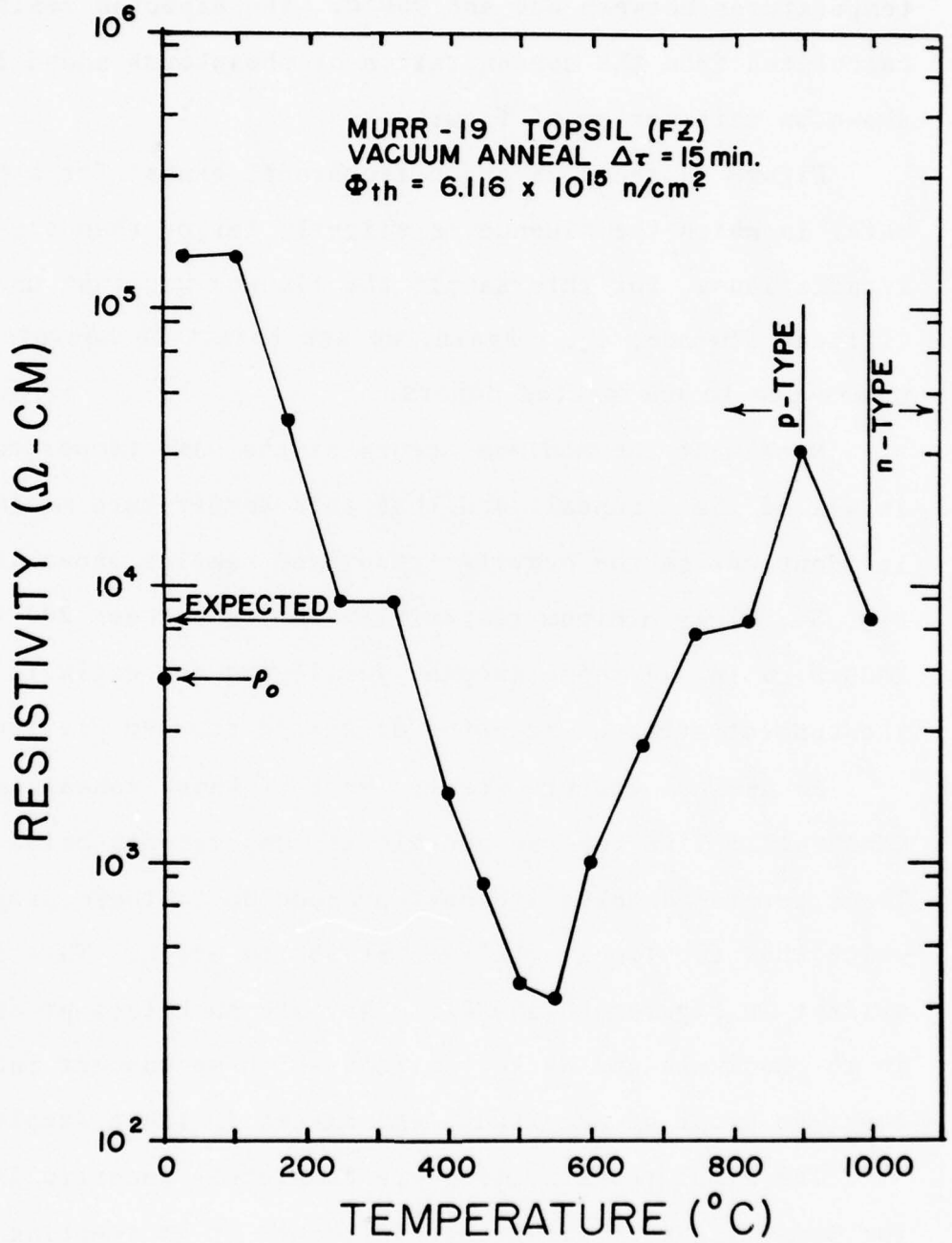

Figure 45. Vacuum isochronal anneal of Topsil wafer.

vacuum and argon anneals are shown in Figures 46 and 47. It can be seen that all of these samples type convert at temperatures between 600 and 900°C. The expected resistivities calculated from the concentration of phosphorus added is also shown on this series of figures.

Figure 48 shows an argon isochronal anneal for a Hughes wafer in which the fluence is slightly larger than the previous irradiations. For this sample the fluence was just under the critical fluence, ϕ_c. Again, we see that type conversion occurs due to unexpected donors.

Note that the minimum occurs at the same temperature in all of these anneals and that this temperature minimum is identical in the heavily irradiated samples shown in Fig. 36. This minimum resistivity varies between 200 to 2000 Ω-cm in all these samples justifying our estimates of the concentration of acceptor defects discussed previously.

An unusual feature seen in most of these anneals are the Czochralski like reverse anneals at temperatures below 600°C. These reverse anneals are most pronounced in those samples which show the lowest minimums at 550 to 600°C. This is evident in Figures 40 and 41. They are much less pronounced in the Rockwell and Wacker silicon which we suspect indicates about an order of magnitude less oxygen in these samples.

The final resistivities are completely uncontrollable for these light irradiations. Although it is tempting to suspect sample contamination during the anneal, we have been

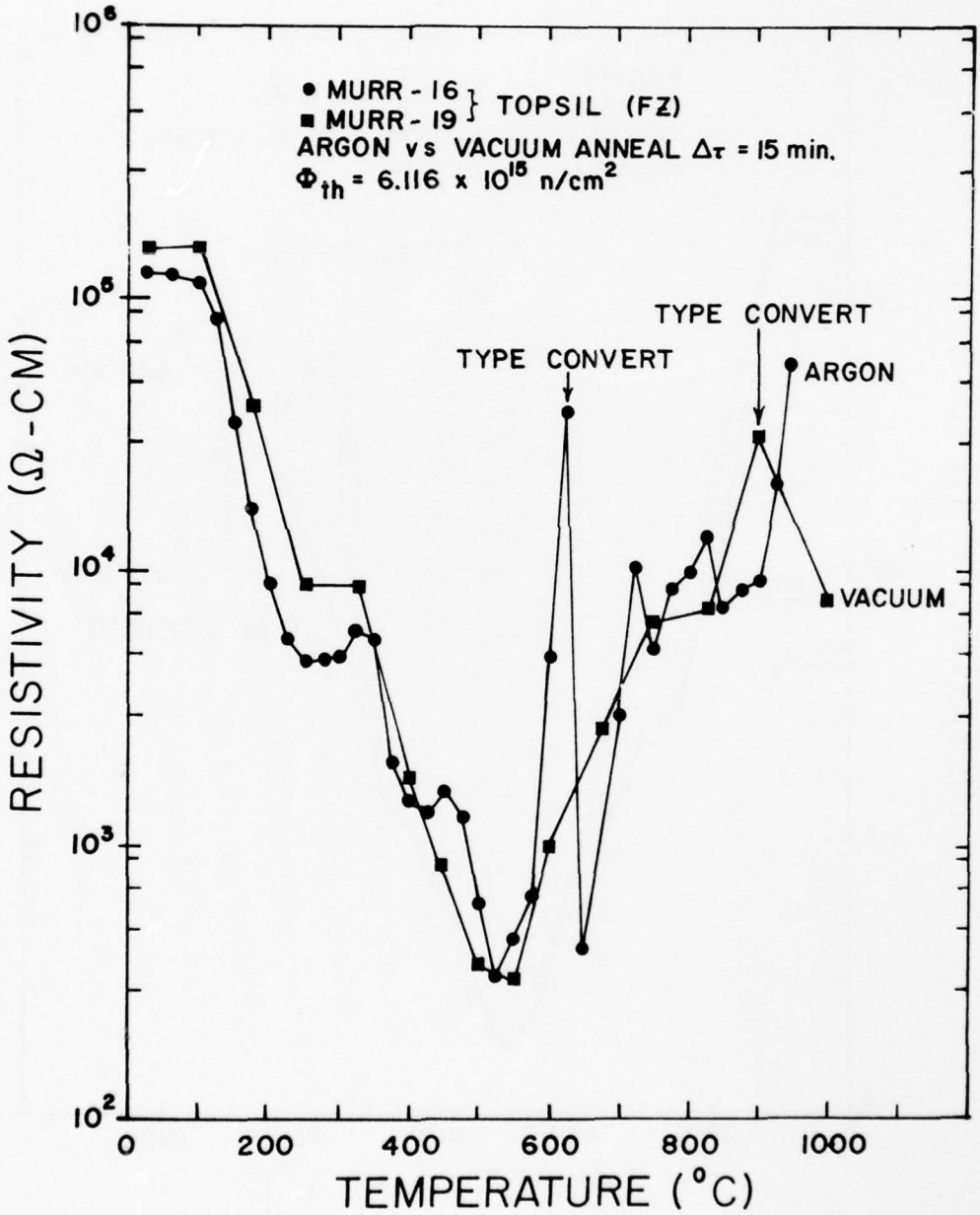

Figure 46. Comparison of vacuum and argon isochronal anneals for Topsil wafers.

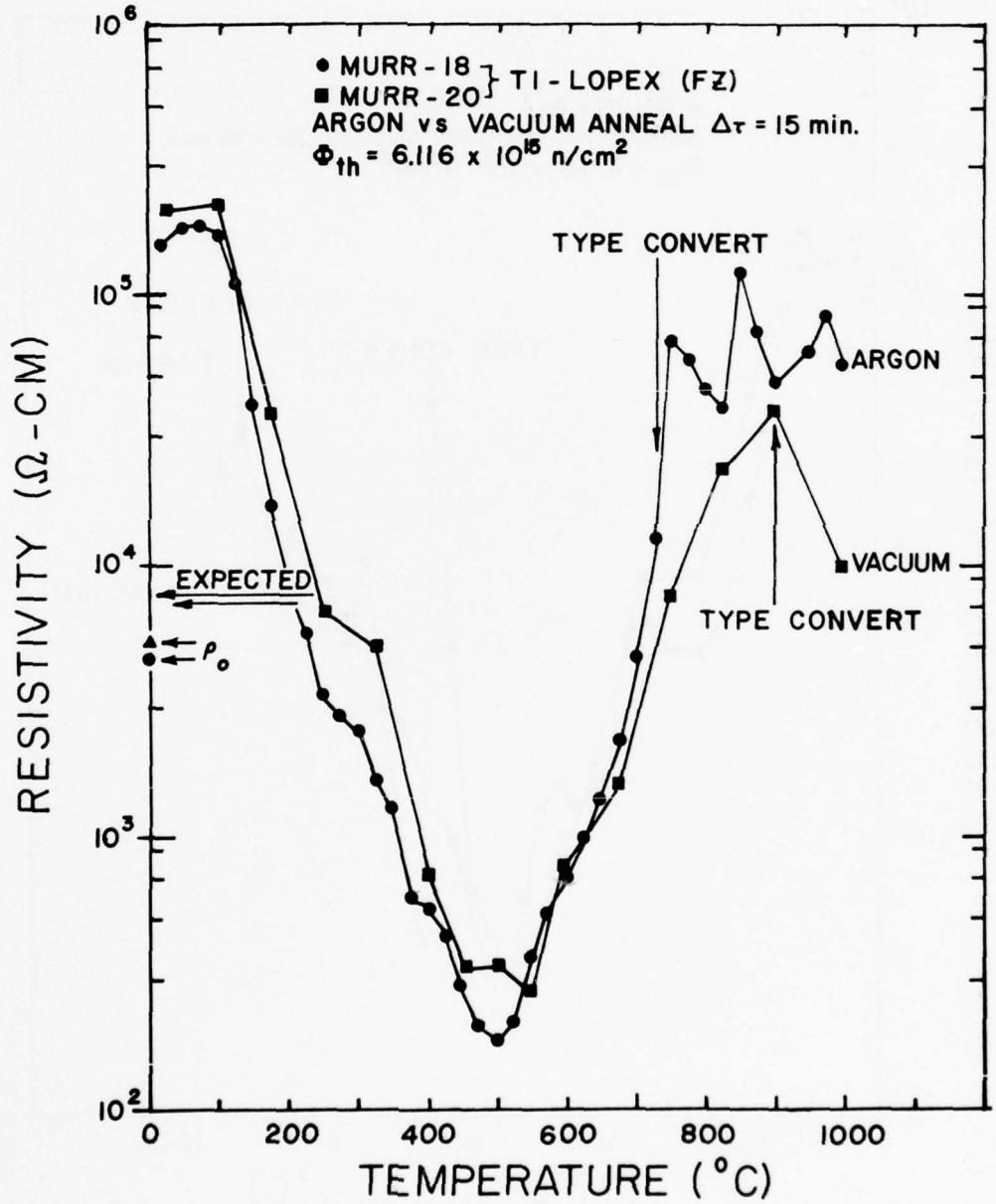

Figure 47. Comparison of vacuum and argon isochronal anneal of T.I. Lopex wafers.

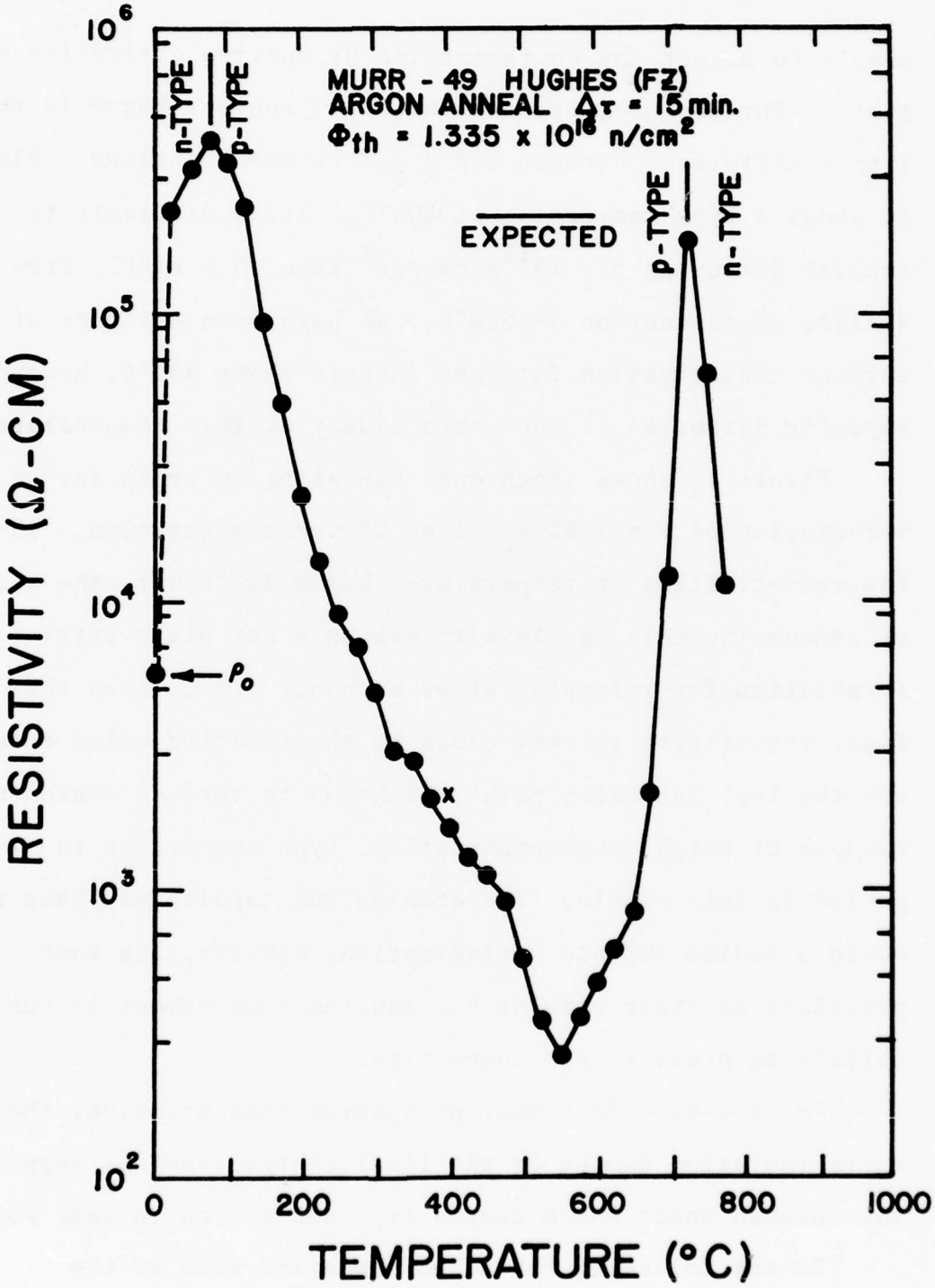

Figure 48. Argon isochronal anneal of Hughes wafer where $\phi \approx \phi_c$.

unable to detect any contamination by neutron activation analysis. Furthermore, Figures 46 and 47 suggest there is very little difference between argon and vacuum annealing. Figure 40 shows a type conversion at 600°C. It is difficult to imagine diffusing 3×10^{12} atoms/cm^3 into this sample from surface contamination at 600°C. We have seen evidence of surface contamination for some anneals above 950°C, however, impurity diffusion is much more likely at this temperature.

Figure 49 shows isochronal annealing in argon for an irradiation of $\Phi = 1.02\ \Phi_c$, i.e. 2% overcompensation. The low resistivities at temperatures below 300°C were the result of remounting this sample with wax on a hot plate after irradiation for relapping after etching. It is seen that the final resistivity is very close to the expected value except for the last annealing point which may be surface contamination. Because of slight overcompensation, type conversion is expected in this sample. The etching and lapping may have removed a sodium surface contamination; however, the same procedure on other samples has made no improvement in our ability to prevent type conversion.

Perhaps the additional phosphorus concentration, the extra radiation damage or the final charge type has suppressed the unknown donor which causes type conversion in some way.

In the following table, we summarize some of the prominent annealing features common to all samples investigated to date. The parameters listed below are the two "Czochralski-

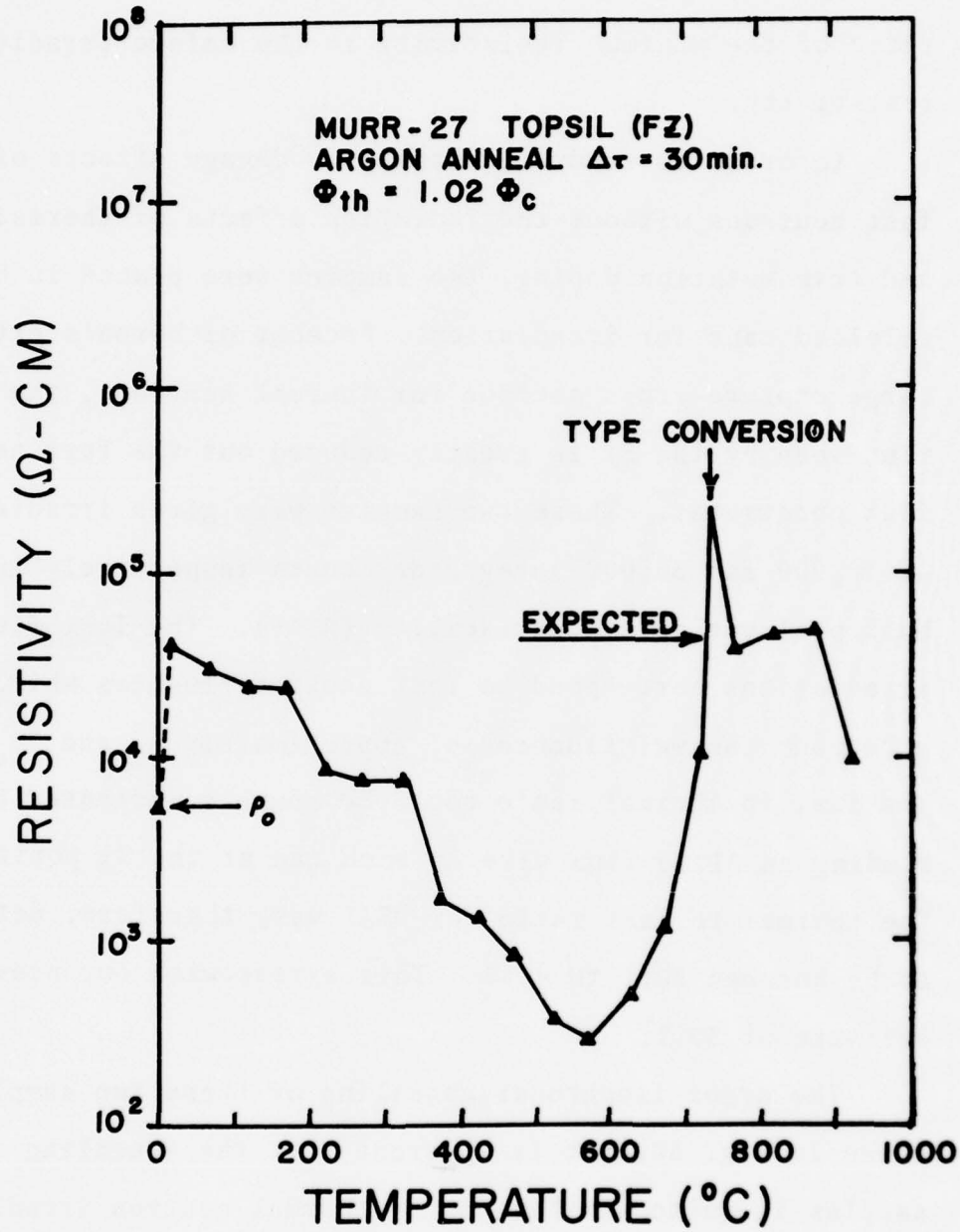

Figure 49. Argon isochronal anneal of Topsil wafer irradiated to $\Phi = 1.02\Phi_c$.

like" peaks, the minimum resistivity temperature and the ratio of the minimum resistivity to the before irradiation resistivity.

In order to study the radiation damage effects of the fast neutrons without the radiation effects of thermal flux and transmutation doping, two samples were placed in boron shielded cans for irradiation. Because of boron's extremely large capture cross section for thermal neutrons, the thermal flux seen by the Si is greatly reduced but the fast neutron flux penetrates. These two samples were given irradiations of 10,000 and 30,000 integrator counts respectively in the bulk pool variable flux facility (RSAF). The fast flux irradiations correspond to fast neutron fluences which would accompany thermal fluences of approximately ϕ_c and $3\phi_c$. The fast to thermal ratio could be roughly estimated by including an Al:Co flux wire in each can at the Si position. The thermal to fast ratio for RSAF was, therefore, determined to be between 20:1 to 40:1. This agrees with our previous estimate of 30:1.

The argon isochronal annealing of these two samples is shown in Fig. 50. It is apparent that the annealing of these samples is quite similar to the thermal neutron irradiation anneals presented earlier. We must conclude, therefore, that most of the electrically active radiation damage is caused by fast neutron damage.

TABLE 13. Summary of Prominent Annealing Features.

Sample	Temp. of 1st Peak	Temp. of 2nd Peak	Temp. of ρ_{min}	$\frac{\rho_{min}}{\rho_o}$	ρ_o
Topsil (Fig. 40)	330°C	450°C	520°C	.07	4000
T.I. (Fig. 41)	330°C	400°C	500°C	.04	4000
VZ-072-2 (Fig. 38)	330°C	missing	540°C	.48	2500
VZ-083-4 (Fig. 39)	320°C	missing	480°C	.13	8000
VZ-072-3 (Fig. 35)	300°C	missing	500°C	.20	2500
Wacker (Fig. 42)	310°C?	missing	480°C	.07	20000
Monsanto (Fig. 35) Czoch.	310°C	420°C			
Russian (Fig. 35) Czoch.	320°C	missing			

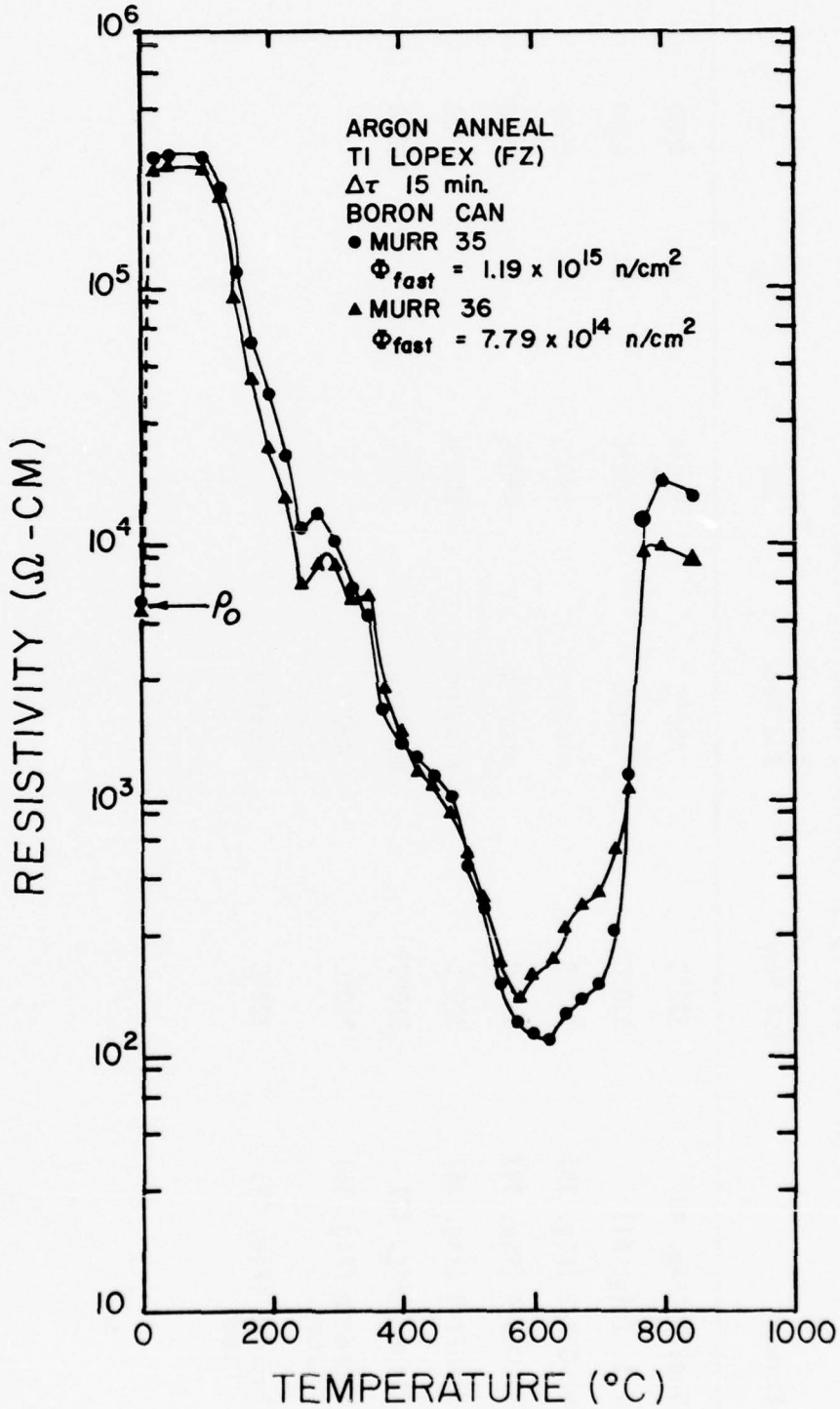

Figure 50. Argon isochronal anneals of fast neutron damage. Thermal neutron flux was suppressed by using boron irradiation can.

Except for a narrow temperature range around 300°C, the annealing of both samples up to 550°C is independent of fluence. In the region from 550°C up to the highest anneal temperature, changes in fluence produce differences in the two anneals and is, therefore, fluence dependent.

It should be noted that both samples recovered closely to their original values in contrast to those samples which have had phosphorus added by transmutation. There is no tendency in either of these samples to type convert! The resistivity in the region of 600 to 800°C corresponds to a donor concentration which is at least two orders of magnitude lower than in those samples containing transmutation produced phosphorus for light irradiations. The phosphorus is, therefore , dominating the compensation process in this range. Also, it should be noted that two small recovery stages in the range of 600 to 700°C are just visible in these two samples. These annealing stages were completely hidden in the transmutation doped samples. (A hint of one of these stages is seen in Figs. 41, 43, 47, and 48.)

From all of the above experiments, it is apparent that a single temperature annealing procedure can be devised. This procedure is as follows:

1. The annealing boat consists of a quartz boat with a 3/4" dia x 2" long silicon support ingot sliced in half lengthwise. This assembly remains inside a closed spectrasil annealing tube and is prepared by preheating the spectrasil annealing tube and boat at 800°C with

flowing argon through the tube for two or more hours. (See Fig. 51.)

2. A 2" float zone wafer is cleaved diametrically, cleaned with soap solution using swabs, D.I. water rinsed, blown dry with argon and swabbed with trichloroethylene. These semicircular liners are used to protect the test wafer from contamination.

3. The prepared spectrasil annealing tube is cooled and opened; the boat is moved to the mouth of the tube but NOT removed.

4. Float zone semicircles (liners) are etched in CP-4 (fresh) solution for 30 seconds in a dedicated container and rinsed in D.I. water.

5. Tweezers are cleaned in Caro's acid (1:1 -H_2O_2:H_2SO_4) (fresh), D.I. water rinsed, and argon blown dry.

6. Liners are removed from rinse, argon blown dry (holding with tweezers), and placed vertically in boat. (This operation is done close to the mouth of the tube).

7. The sample is swabbed with soap solution, D.I. water rinsed, argon blown dry, and swabbed with trichloroethylene.

8. Tweezers are recleaned as in #5.

9. The sample is etched in CP-4 for 30 seconds (dedicated container) D.I. water rinsed, argon blown dry (while

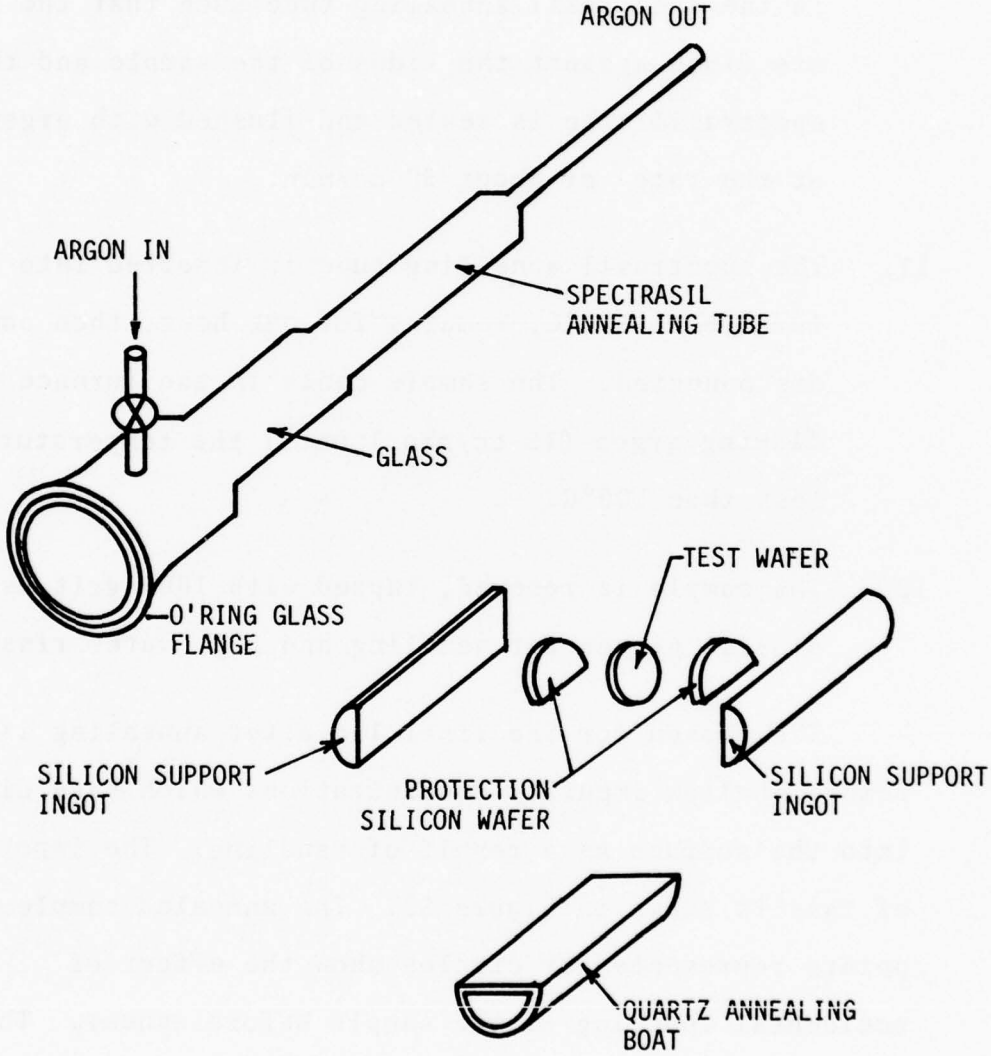

Figure 51. Annealing furnace tube, sample boat, and silicon spacers.

holding with tweezers) and placed between liners.

10. The sample boat is slid into the annealing position in the spectrasil annealing tube such that the liners are flush against the sides of the sample and the spectrasil tube is sealed and flushed with argon at the rate of about 30 cc/min.

11. The spectrasil annealing tube is inserted into the furnace at 800°C, remains for one hour, then power is disconnected. The sample cools in the furnace in flowing argon (15 cc/min.) until the temperature is less than 100°C.

12. The sample is removed, lapped with 1000 grit using plastic gloves for handling and D.I. water rinsed.

The reason for the final lap after annealing is to remove shallow impurity concentrations which have diffused into the surface as a result of handling. The importance of this is shown in Figure 52. The annealed sample data points represented by circles show the effect of accidental touching of the sample before anneal. The lapping removes these impurities and dramatically improves resisitivity fluctuations. The final average value near 800 Ω-cm is very close to the expected resistivity value for this sample.

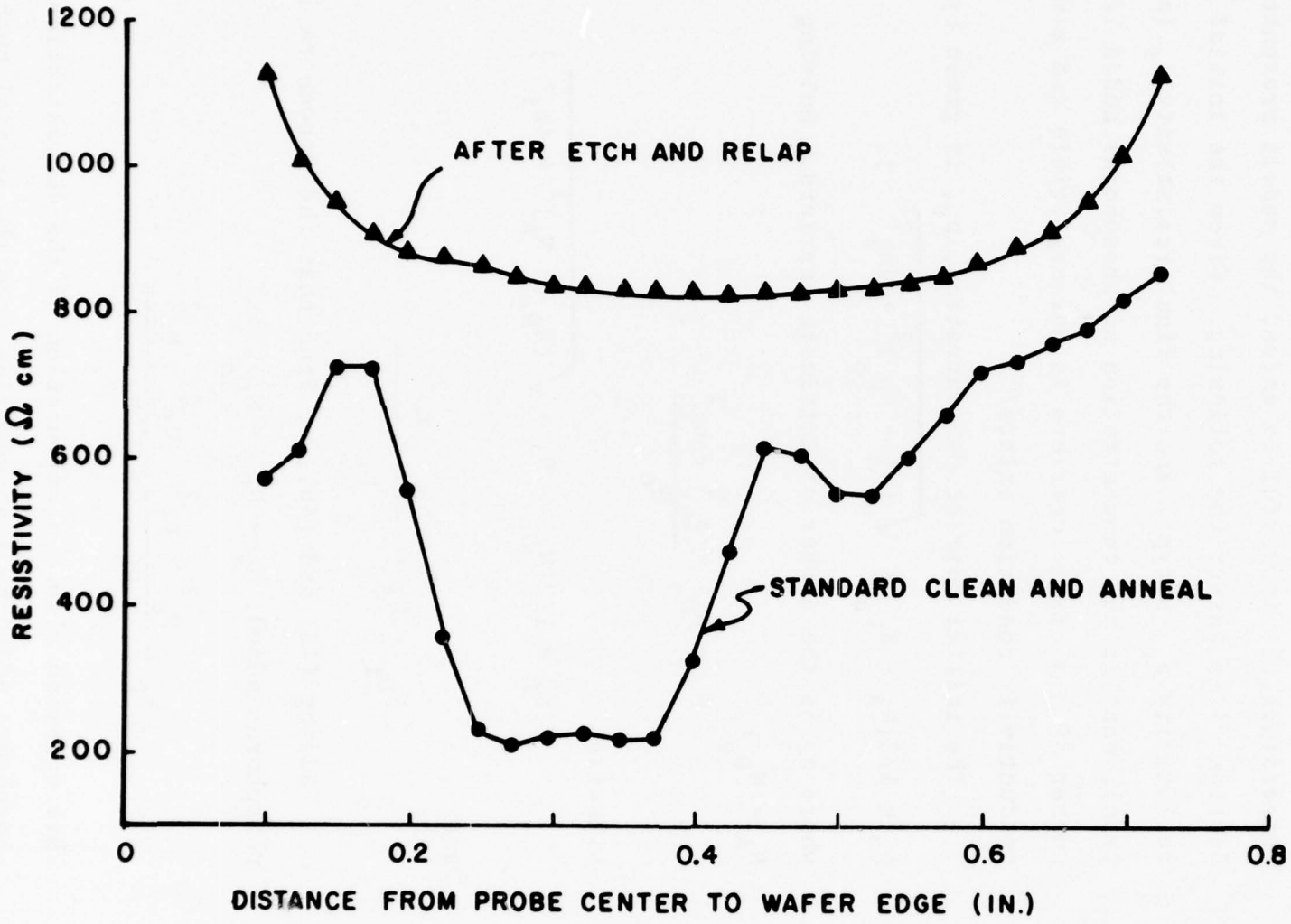

Figure 52. The effect of a final lap on $\rho(x)$.

In order to evaluate the success of our single anneal temperature, it is useful to extend the models presented in Section II to answer the following. Given the initial resistivity ρ_o (p-type) and the final resistivity ρ_f (n-type), what is the concentration of phosphorus added if the number of intrinsic carriers is not negligible and a mixed conductivity condition exists?

The initial carrier concentration, p_o, is given by

$$p_o = 1/2[N_A - N_{D_o} + \sqrt{(N_A - N_{D_o})^2 + 4n_i^2}\ ]$$

where n_i is the number of intrinsic carriers. Solving for $N_A - N_{D_o}$,

$$N_A - N_{D_o} = \frac{p_o^2 - n_i^2}{p_o} \quad . \tag{45}$$

Likewise,

$$n_f = 1/2[N_{D_f} - N_A + \sqrt{(N_{D_f} - N_A)^2 + 4n_i^2}\ ]$$

and

$$N_{D_f} - N_A = \frac{n_f^2 - n_i^2}{n_f} \quad . \tag{46}$$

Adding (45) and (46), we find that the concentration of phosphorus added, $N_P = N_{D_f} - N_{D_o}$, is

$$N_P = \frac{p_o^2 - n_i^2}{p_o} + \frac{n_f^2 - n_i^2}{n_f} \quad . \tag{47}$$

This equation allows a calculation of the concentration of phosphorus added by transmutation from the initial number of

holes (p-type) and final number of electrons (n-type). But these concentrations are related to the measured resistivity and $b = \mu_n/\mu_p$ by Eq. (13)

$$\rho = \begin{cases} \dfrac{p}{e\mu_p\,(bn_i^2 + p^2)}, & \text{p-type} \\[2ex] \dfrac{n}{e\mu_p\,(bn^2 + n_i^2)}, & \text{n-type.} \end{cases}$$

Solving these relations for n or p as a function of the resistivity, ρ, we find that

$$n_f = 1/2\left[\frac{1}{\rho_f e\mu_p b} + \sqrt{\left(\frac{1}{\rho_f e\mu_p b}\right)^2 - \frac{4n_i^2}{b}}\right] \quad (48)$$

$$p_o = 1/2\left[\frac{1}{\rho_o e\mu_p} + \sqrt{\left(\frac{1}{\rho_o e\mu_p}\right)^2 - 4bn_i^2}\right]. \quad (49)$$

Thus, given ρ_o and ρ_f, we can calculate p_o and n_f from (48) and (49), and by substitution into (47), we obtain the concentration of phosphorus added in the presence of mixed conduction for the case where n_i is not negligible. It should be noted that (47) reduces to $N_p = p_o + n_f$ if $n_i \ll p_o$, n_f. Likewise, under similar conditions (48) and (49) become

$$n_f = \frac{1}{\rho_f e\mu_n}, \quad p_o = \frac{1}{\rho_o e\mu_p}. \quad (50)$$

For $p_o \gg n_i$ but $n_f \sim n_i$ we have a condition which exists for slightly overcompensated samples. For these conditions

$$N_p = p_o + \frac{n_f^2 - n_i^2}{n_f} \tag{51}$$

where

$$p_o = \frac{1}{\rho_o e \mu_p} \text{ and } n_f \text{ is obtained from (48).}$$

The results of the single 800°C anneal temperature procedure are show in Table 14. The success of achieving the correct resistivity for overcompensated material has been as spectacular as the failures for undercompensation. In Table 14, the initial and final resistivities, the concentration of phosphorus added as expected from the integrator calibration, $N_p(E)$, the concentration of phosphorus added as calculated from the resistivities, $N_p^{(o)} = K\Phi$, and the percentage error between expected and observed phosphorus concentration is shown. Note that a resistivity of over 100,000 Ω-cm has been achieved in MURR-70. This represents an uncompensated carrier concentration of only $3.77 \times 10^{10} cm^{-3}$, about three times the intrinsic carrier concentration. The conventional compensation ratio N_A/N_D is about 0.95. Because of the success of these last experiments, it was felt that the Ga doped Si could be successfully compensated. The remainder of the compensation experiments were, therefore, performed on samples taken from Rockwell ingot GZ-156, a Ga doped ingot.

A very simple and accurate technique was devised to

TABLE 14. Results of single temperature annealing procedures for different target resistivities.

Sample No.	ρ_f(n-type) (Ω-cm)	ρ_o(p-type) (Ω-cm)	Φ/Φ_c	$N_p^{(E)} = K\Phi$ (Expected) (ppb)**	$N_p^{(o)}(\rho)$ (Observed) (ppb)	$\frac{N_p^{(E)} - N_p^{(o)}}{N_p^{(E)}} \times 100$
MURR-16 (Topsil)	115.64	*58560	++20.6	0.7893	0.7758	-1.71%
MURR-3 (Rockwell) (VZ-072-3)	134.03	4188	16.4	0.7893	0.7285	-7.7% Resistivity edge effects
MURR-29 (Rockwell) (VZ-083-7)	6038.7	12510	1.788	0.03617	0.03505	-3.1%
MURR-27+ (Topsil)	43,490	5248	1.022	0.05291	0.05394	+1.9%
MURR-70 (Rockwell) (VZ-083-50-3)	102,000	18970	1.000	0.0133	0.01405	+5.64%

*Resistivity before second irradiation.

**1 ppb = $4.996 \times 10^{13} cm^{-3}$

+Argon anneal for 1 hr. at 800°C + slow cool.

++Calculated approximately from initial resistivity before 1st irradiation.

determine the boron compensation. After multiple zone passes to reduce impurities other than boron to negligible concentrations but before the addition of Ga, a fourpoint probe measurement of the starting ingot, VZ-107, indicated that $\rho = 2.4 \times 10^3$ Ω-cm and that p = 0.108 ppb = $5.42 \times 10^{12} cm^{-3}$. This value, obtained from Rockwell, was used to determine the critical fluence, ϕ_c. Ga was then added to the ingot.

Although this procedure should have worked well, several problems arose. The current and voltage leads on the Rockwell apparatus were hooked to the wrong instruments leading to an estimated error of 20%. Furthermore, a measurement of $\rho(x)$ vs. x on undoped wafers from this ingot (GZ-156 -C,D,G, and H) indicated surface contamination from unknown sources. This is shown quite clearly in Fig. 53 for GZ-156-G. The resistivity near the edge drops to about 1 Ω-cm. Since this sample was only a half wafer (its shape is shown in the upper right of Fig. 53). the edge effect on the four point probe technique was claimed to be the source of the difficulty by the Rockwell group. We, therefore, performed a similar experiment on a half wafer from VZ-083 both before and after cleaving into a half wafer shape. The results of this experiment are shown in Fig. 54. As logic and theory would dictate, the apparent resistivity for the half wafer from VZ-083 rises at the edges. We can only conclude, then, that surface contamination exists on wafer GZ-156-G. We have returned this wafer to Rockwell, at their request, for further

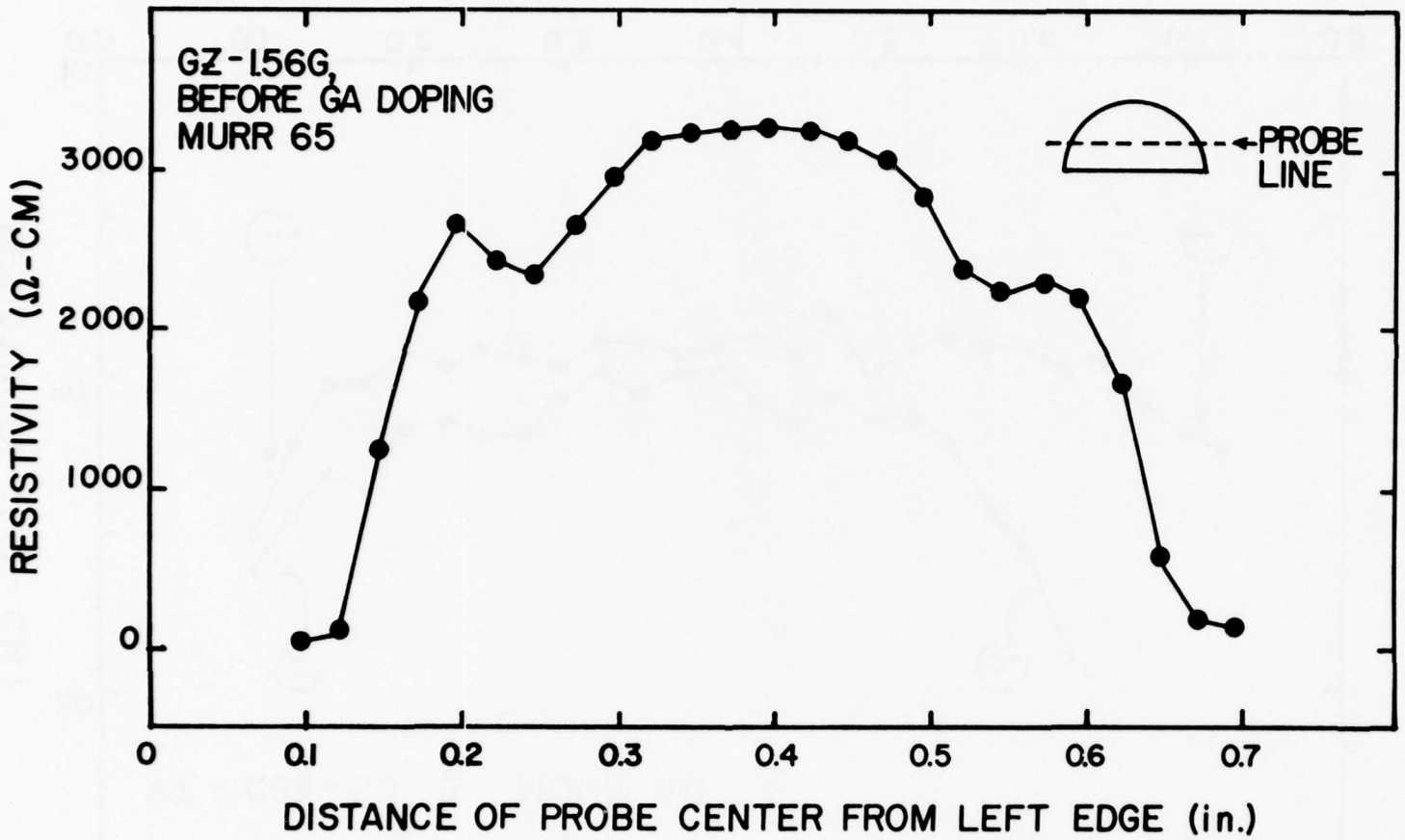

Figure 53. ρ(x) vs. x for undoped wafer from GZ-156, the ingot to be used for NTD detector fabrication.

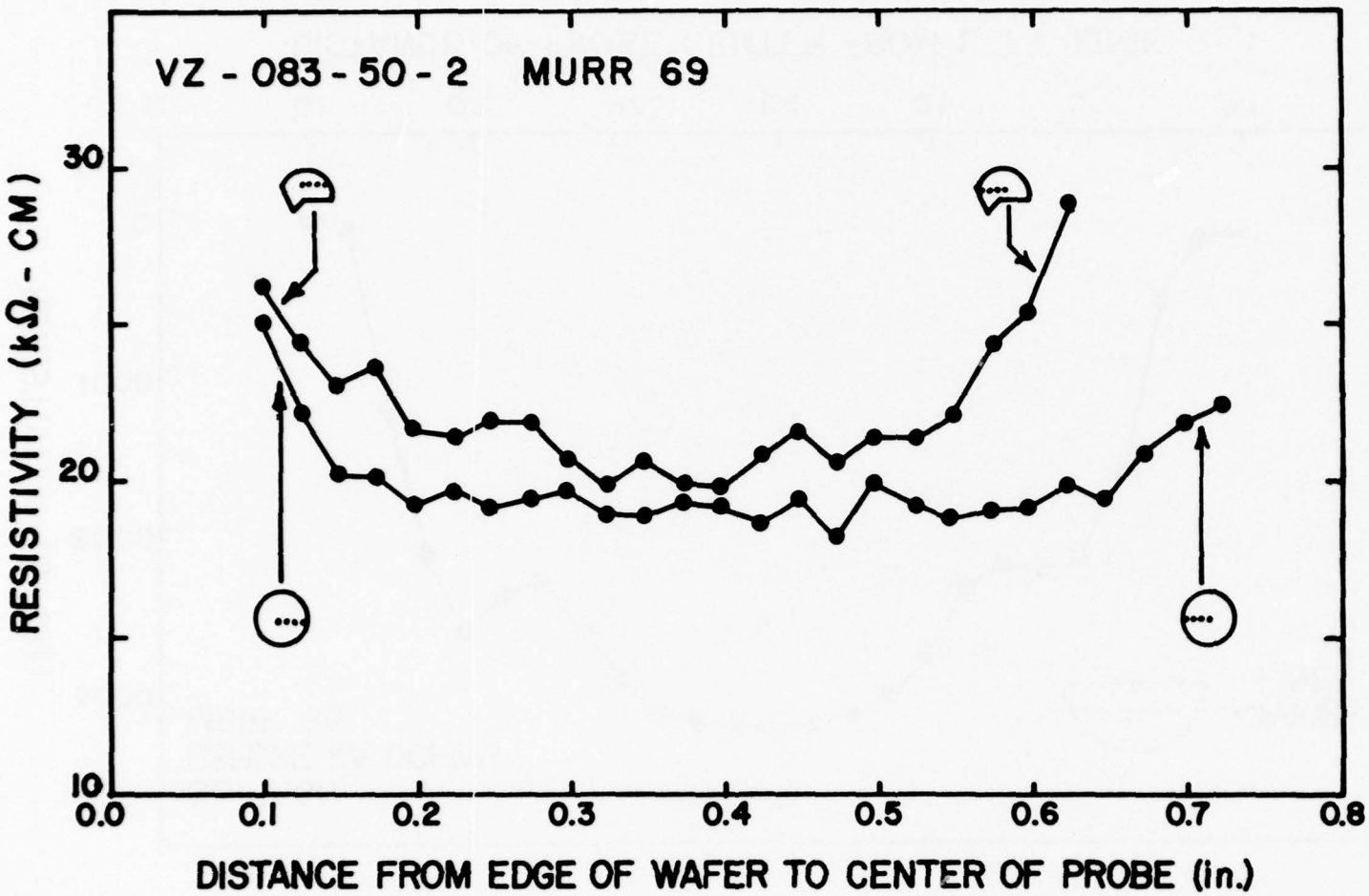

Figure 54. $\rho(x)$ vs. x before and after cleaving into a half wafer for VZ-083.

analysis. A second half wafer with similar $\rho(x)$ vs. x characteristics has been retained by MURR for activation analysis.

Since it was not clear which value of overcompensation of the boron concentration would produce the best D*, compensation ranges for ϕ/ϕ_c from about 1:1 up to 20:1 were performed. This range of doping ratios was requested by Rockwell. These irradiations are summarized in Table 15.

All of these samples were slightly underirradiated (-3 to -10%) due to a lack of calibration factor for the high number of integrator counts encountered for these samples. This is of little consequence because of the 20% error in initial resistivity determination and the nonuniformity of resistivity for GZ-156-G. One set of samples was irradiated, cleaned, and annealed at MURR while an identical set was irradiated but not annealed or cleaned. Both sets were sent to Rockwell. Three samples were retained by MURR for isochronal annealing experiments (MURR-52, MURR-53, and MURR-56) corresponding to ϕ/ϕ_c values from 1 to 3. All other samples from this set were returned to Rockwell for detector fabrication.

Isochronal anneals of the Ga doped samples (MURR-52, MURR-53, and MURR-56) were performed to evaluate any new difficulties which might arise because of defect-Ga complexing. The results of these argon isochronal anneals are shown in Fig. 55. By 800°C all samples have recovered to their initial value as expected for these heavily Ga doped samples. All of

Irrad. Log (1322 counts/hr)

TABLE 15: Summary of Irradiations (Ga doped Si).

Ga Doped Rockwell GZ-156

Sample No.	Counts	$\Phi x10^{-16}$ Integ.	$\Phi x10^{-16}$ Fluxwire	$\frac{\Phi}{\Phi_c} \approx \frac{N_P}{N_B}$	N_P added (ppb)	Anneal/Exp. S.C. = slow cool	Irrad. No/Position *sent to Rockwell
GZ-156-6 MURR 50	20648	3.219	(-4.7%) 3.067	1.0	0.108	Unannealed*	Meese-23
GZ-156-9 MURR 51	20648	3.219	3.067	1.0	0.108	MURR-800°C+S.C. Argon*	RSAF 12-16
GZ-156-10 MURR 52	(Broken during irradiation) 20648	3.219	3.067	1.0	0.108	Isochronal MURR	
GZ-156-7 MURR 53	41296	6.438	(-5.3%) 6.098	2.0	0.216	MURR-Isochronal Argon	Meese-24
GZ-156-11 MURR 54	41296	6.438	6.098	2.0	0.216	MURR-800°C+S.C. Argon *	RSAF 12-16
GZ-156-12 MURR 55	41296	6.438	6.098	2.0	0.216	Unannealed*	
GZ-156-8 MURR 56	61944	9.657	(-6.04%) 9.074	3.0	0.324	MURR-Isochronal Argon	Meese-25
GZ-156-13 MURR 57	61944	9.657	9.074	3.0	0.324	MURR-800°C+S.C. Argon *	RSAF 12-16
GZ-156-14 MURR 58	61944	9.657	9.074	3.0	0.324	Unannealed*	

TABLE 15: Summary of Irradiations (Ga doped Si) (Cont.).

Irrad. Log (1322 counts/hr)

Ga Doped Rockwell GZ-156

Sample No.	Counts	$\Phi x10^{-16}$ Integ.	$\Phi x10^{-16}$ Fluxwire	$\frac{\Phi}{\Phi_c} \approx \frac{N_p}{N_B}$	N_p added (ppb)	Anneal/Exp. S.C. = slow cool	Irrad. No/Position *sent to Rockwell
GZ-156-15 MURR 59	103240	16.095	new scale (-3.1%) 15.596	5.0	0.540	MURR-800°C+S.C.*	Meese-26 RSAF 12-16
GZ-156-16 MURR 60	103240	16.095	15.596	5.0	0.540	Unannealed*	
GZ-156-17 MURR 61	8020	32.19	(-9.94%)* 28.99	10.0	1.08	MURR-800°C+S.C.*	Meese-27 I-2 50-75 cm 8019 cts/ppb
GZ-156-18 MURR 62	8020	32.19	28.99	10.0	1.08	Unannealed*	
GZ-156-19 MURR 63	16040	64.38	(-10.65%)* 57.52	20.0	2.16	MURR-800°C+S.C.*	Meese-28 I-2 50-75 cm
GZ-156-20 MURR 64	16040	64.38	57.52	20.0	2.16	Unannealed*	

*First calibration runs in I-2 position

the effects seen in the undoped material are masked by the Ga concentration which is greater than $10^{16} cm^{-3}$. Sample MURR-52 was taken from the broken wafer. Because of four point edge effects, the apparent resistivity of this sample is slightly higher.

The evaluation of D* vs. degree of overcompensation has not been completed unfortunately, since, at the close of this contract, detectors have not been fabricated from these Ga doped wafers by Rockwell as promised. We urge that this set of samples be recovered by AFML for in-house evaluation. We believe that the center sections of these wafers, at least, are suitable for evaluation of D* vs. N_P/N_B ratio.

As a final set of experiments, we have considered both theoretically and experimentally the magnitude of the resistivity fluctuations as a function of the degree of overcompensation, i.e., the phosphorus to boron ratio. These experiments are extremely important since they demonstrate conclusively that nuclear transmutation doping provides superior wafer uniformity for all phosphorus to boron ratios greater than about 1.3. For samples overcompensated to a ratio of 2:1, transmutation compensated detector material possesses resistivity fluctuations which are about an order of magnitude better than conventionally compensated material.

We proceed by considering the fluctuations in conventionally compensated material. Typical results[46] obtained at Rockwell for a [P]/[B] ratio of about 1.61 are:

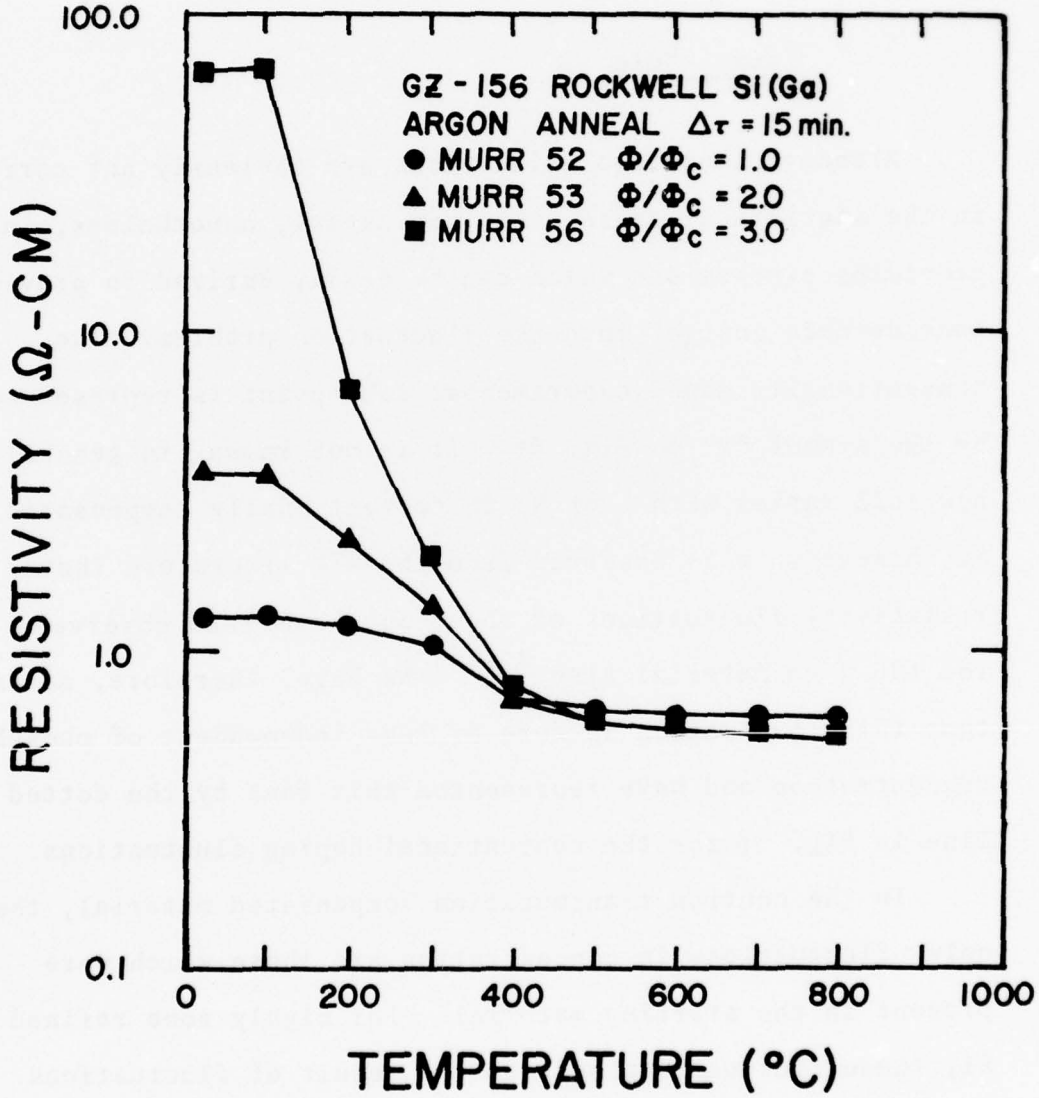

Figure 55. Isochronal argon anneals for transmutation compensated Ga doped Si.

$$\frac{\Delta\rho}{\bar{\rho}} = \frac{400\ \Omega\text{-cm}}{1350\ \Omega\text{-cm}} \cong 29.6\%$$

where we will use the definitions

$$\Delta\rho = \rho_{max} - \rho_{min}$$

and

$$\bar{\rho} = \frac{\rho_{max} + \rho_{min}}{2} .$$

Although these two definitions are obviously not correct in the statistical sense, they are useful, nonetheless, in providing expressions which can be easily derived to provide considerable insight into the fluctuation problem. The conventionally doped experimental data point is represented by the symbol "x" on Fig. 56. It is not known, in general, how $\Delta\rho/\bar{\rho}$ varies with ρ or N_p in conventionally compensated Si; however, it is observed from the NTD literature that resistivity fluctuations of about 30% have been observed for 100 Ω-cm material also.[47-49] We have, therefore, assumed that this fluctuation is more or less independent of phosphorus concentration and have represented this fact by the dotted line in Fig. 56 for the conventional doping fluctuations.

In the neutron transmutation compensated material, the only fluctuations in concentration are those which were present in the starting material. For highly zone refined Si, these fluctuations must be the result of fluctuations in boron concentration. The phosphorus added by transmutation is completely uniform, a fact which will be demonstrated by the calculations to follow; therefore, the impurity fluctuation $\Delta[B]$ is a constant where [B] represents the concentration of

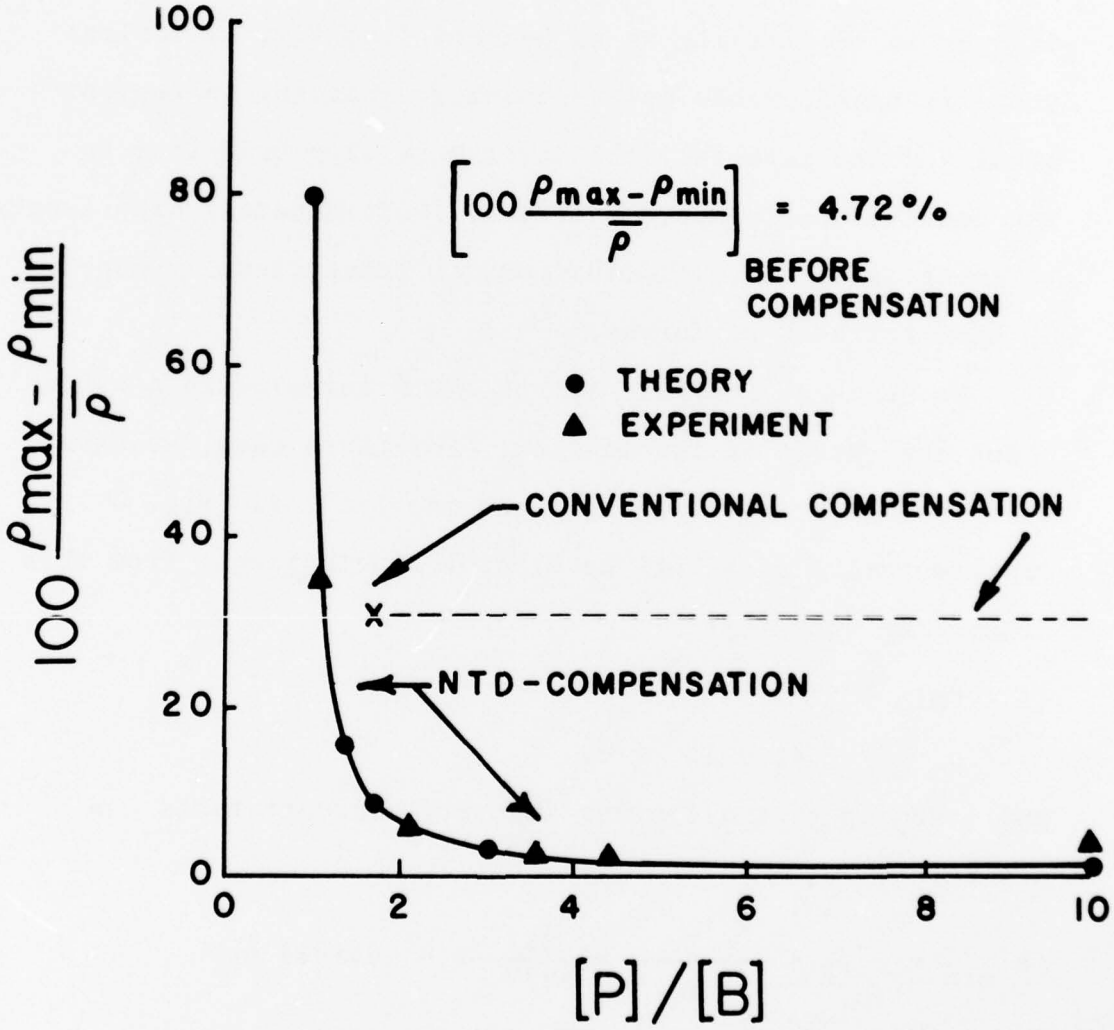

Figure 56. Experimental and theoretical resistivity fluctuations as a function of phosphorus to boron concentration ratio for an initial resistivity fluctuation before compensation of 4.72%.

boron in the starting material. It is, therefore, obvious that the fluctuations in impurity concentration must be superior in the NTD material as compared to conventional phosphorus doping. Nevertheless, the percentage fluctuation in resistivity must get larger near exact compensation since very small changes in impurity concentration cause rapid changes in resistivity as is evident from Fig. 1. Unless there is considerable boron-phosphorus pairing in conventionally doped material, this fact must also hold true in the conventionally doped material. Unfortunately experiments to investigate those fluctuations in conventionally doped Si have not been performed.

We begin an analysis of the NTD material with a typical boron concentration fluctuation. For these data, we have used the resistivity fluctuations in VZ-072-#2 (Fig. 29) as representative of a best case boron fluctuation. From this figure, we find that

$$\rho_{min} = 2.29 \times 10^3 \ \Omega\text{-cm}$$

$$\rho_{max} = 2.40 \times 10^3 \ \Omega\text{-cm}$$

and assuming that all other impurity concentrations can be neglected,

$$[B]_{min} = p_{min} = \frac{K_p}{\rho_{min}} = \frac{253}{2400} = 0.1054 \text{ ppb}$$

$$[B]_{max} = p_{max} = \frac{K_p}{\rho_{max}} = \frac{253}{2290} = 0.1105 \text{ ppb}$$

Therefore,

$$\Delta B = [B]_{max} - [B]_{min} = 0.0051 \text{ ppb},$$

and

$$\overline{[B]} = \frac{[B]_{max} + [B]_{min}}{2} = 0.108 \text{ ppb}.$$

We must add 0.108 ppb phosphorus by nuclear transmutation for the average boron concentration to be compensated exactly, i.e., [P]/[B] = 1. When this is done, the highest resistivity in the wafer will be the intrinsic resistivity, ρ_i = 214,000 Ω-cm. Parts of the wafer will be n-type and parts will be p-type with resistivities lower than the intrinsic resistivity due to impurity fluctuations. However, because of differences in the mobility of electrons and holes, the resistivity drops more steeply from ρ_i on the p-type side of intrinsic, therefore, the minimum resistivity will be in p-type material. We now have, for [P]/[B] = 1

$$\rho_{max} = \rho_i = 2.14 \times 10^5 \ \Omega\text{-cm}$$

and we wish to calculate ρ_{min}. Approximately half of the carrier fluctuation will be on the p-type side, therefore, the hole concentration for this case can be calculated from

$$p = n_i + \frac{\Delta B}{2} \cong \frac{\Delta B}{2} = \frac{0.0051}{2} = 0.0026 \text{ ppb}$$

$$= 1.3 \times 10^{11} \text{cm}^{-3}.$$

The resistivity corresponding to this concentration is found from Eq. (13)

$$\rho_{min} = \frac{p}{e\mu_p(bn_i^2 + p^2)} ,$$

and using $\mu_p = 494 cm^2/V\text{-}sec$, $n_i^2 = 1.93 \times 10^{20} cm^{-6}$, and $b = 1.6$, we find that

$$\rho_{min} = 2.72 \times 10^4 \ \Omega\text{-cm}$$

$$\Delta\rho = \rho_{max} - \rho_{min} = (2.14 - 0.272) \times 10^5 \ \Omega\text{-cm}$$

and

$$\frac{\Delta\rho}{\rho_i} = \frac{2.14 \times 10^5 - 2.72 \times 10^4}{2.14 \times 10^5} \cong 77.9\%.$$

This calculated point is represented by the solid circle on Fig. 56 for [P]/[B] = 1. The second solid circle at 1.3 was obtained in a similar way.

Since the number of intrinsic carriers is negligible for all the other [P]/[B] ratios calculated, we will only illustrate one of these calculations.

For [P]/[B] = 1.63, the target phosphorus concentration is

$$[P] = (1.63)(0.108) = 0.176 \text{ ppb}.$$

The electron concentration which is uncompensated is given by

$$n = 0.176 - 0.108 = 0.068 \text{ ppb}$$

and

$$\rho_n = \frac{K_n}{n} = \frac{87.9}{0.068} = 1292.6 \ \Omega\text{-cm}.$$

To find the resistivity fluctuation, we need the electron concentration fluctuation. This is found from

$$n_{max} = 0.068 + \frac{[\Delta B]}{2}$$

$$= 0.068 + \frac{0.0051}{2} = 0.0706 \text{ ppb}$$

and

$$\rho_{max} = \frac{87.9}{0.0706} = 1245\ \Omega\text{-cm.}$$

Likewise,

$$n_{min} = 0.068 - \frac{[\Delta B]}{2}$$

$$= 0.068 - \frac{0.0051}{2} = 0.0655 \text{ ppb}$$

and

$$\rho_{min} = \frac{87.9}{0.0655} = 1342\ \Omega\text{-cm.}$$

Therefore,

$$\frac{\Delta\rho}{\rho} = \frac{1342 - 1245}{1292.6} \cong 7.5\% .$$

This data point is represented by the solid dot for the [P]/[B] ratio of 1.63. The remainder of the calculated points were obtained similarly. It is seen that the fluctuations are already a factor of four smaller than for conventional doping at the [P]/[B] ratio of 1.63 and the improvement increases for higher ratios. When the [P]/[B] ratio is 3, the resistivity fluctuations become smaller than the percentage error in the four point resistivity measurements. We, therefore, conclude that this ratio is ideal to obtain good uniformity in an IR detector array. This ratio is also close to that expected for a maximum D*.

It should be noted that an increase in resistivity fluctuations in the starting material increases the percentages shown in Fig. 56 while a decrease would lower this curve.

The triangles in Fig. 56 represent data points obtained experimentally from a set of similar undoped wafers where the [P]/[B] ratio was obtained by nuclear transmutation and the fluctuations were measured using four point resistivity probes. The data points at [P]/[B] = 4.45 and 10.0 were corrected for the fact that their initial resistivity fluctuations were 7.12% and 5.94% respectively instead of 4.72% assumed in the model calculation.

The $\rho(x)$ vs. x data for the samples used in the above experiment and taken after transmutation doping and annealing are shown in Fig. 57. The initial resistivity fluctuation and final [P]/[B] ratio is indicated by each sample number. The fluctuations decrease as the [P]/[B] ratio increases in accordance with the theory.

We believe that this set of calculations and experiments demonstrates that NTD-Si does indeed produce a more uniform resistivity profile and should, therefore, contribute greatly to IR detector array uniformity. This is one of the major conclusions to be obtained from this work.

V. PROGRESS AND ACCOMPLISHMENTS

The object of this research program was to develop the technique of neutron transmutation doping in silicon to the point that the compensation ratio can be controlled to a very high precision. Significant success in this task will allow much better control over the boron compensation in silicon used for extrinsic IR detection. This in turn should provide a better control over

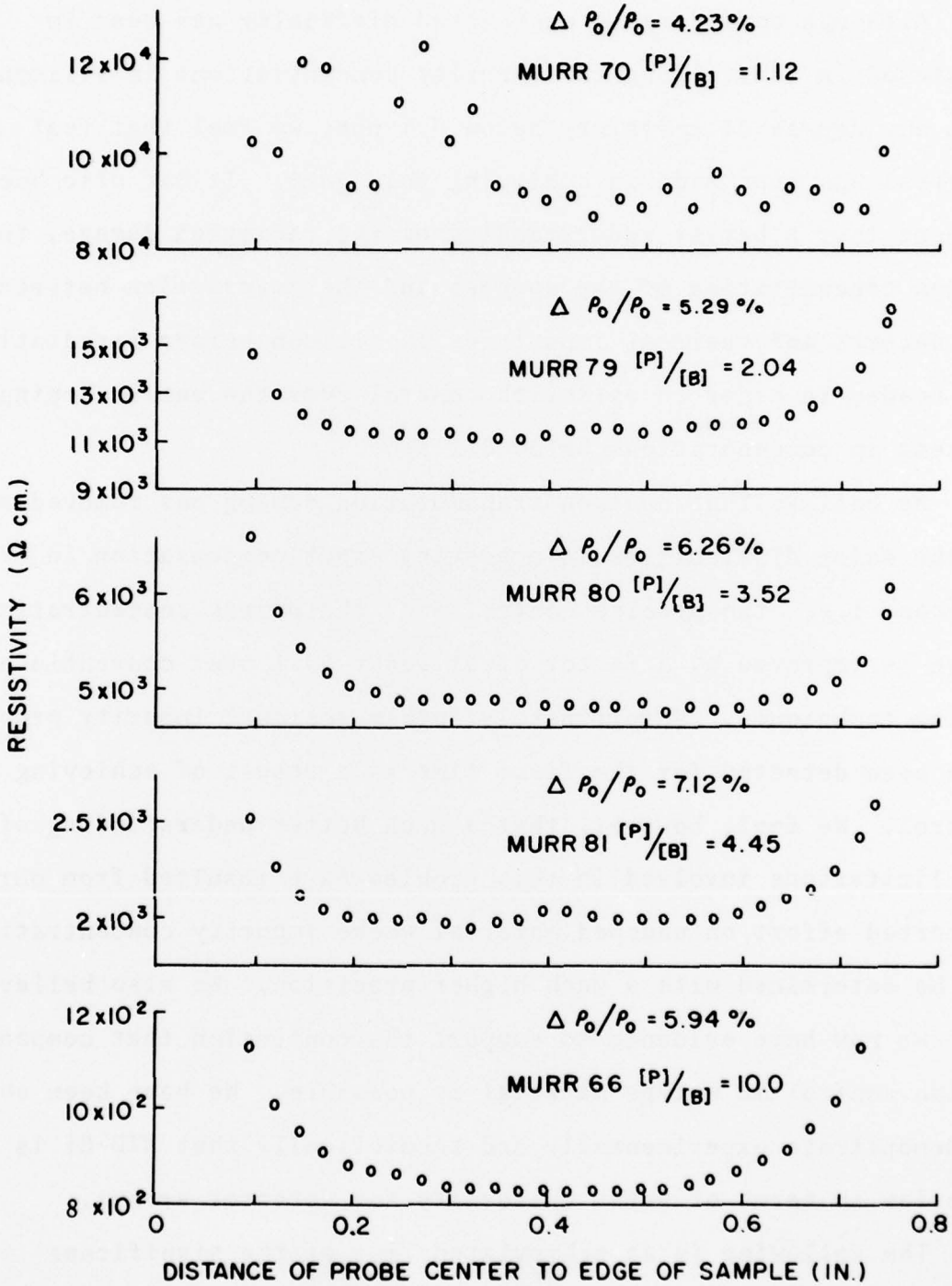

Figure 57. ρ(x) vs. x data for various ratios of [P]/[B] obtained by nuclear transmutation doping and annealing.

detector detectivity and temperature dependence.

Although considerable unexpected difficulty has been encountered in controlling the impurity concentrations in silicon with any degree of certainty below 0.1 ppb, we feel that real progress has been made in achieving this goal. It has also become evident that a better understanding of the radiation damage, the oxygen concentration of the samples and the interaction between the defects and residual impurities in silicon before irradiation are needed in order to establish control over the entire doping process in concentrations below 0.1 ppb.

We believe that neutron transmutation doping has removed one of the major difficulties in achieving exact compensation in silicon, i.e., the precise control over phosphorus concentration which is improved by a factor of at least 50:1 over conventional doping techniques. Unfortunately, other residual impurity problems have been detected for the first time as a result of achieving this control. We feel, however, that a much better understanding of the limitations involved in this problem have resulted from our concerted effort on undoped material where impurity concentrations can be determined with a much higher precision. We also believe that we now have evidence to support the contention that compensation control in n-type material is possible. We have been able to demonstrate experimentally and theoretically that NTD-Si is superior in terms of wafer uniformity for detector arrays.

The following is an abbreviated list of the significant accomplishments achieved during this program.

- Construction of the Bulk Pool Variable Flux Facility and demonstration of fluence reproducibility to $\pm$ 0.5%.
- Demonstration of doping concentration control to $\pm$ 1% for 100 Ω-cm material and $\pm$ 3% for resistivities as high as 100,000 Ω-cm.
- No significant impurity problems detectable by neutron activation analysis down to concentrations of better than 0.1 ppb with the exception of sodium in concentrations of 1 to 8×10^{13} atoms/cm^3.
- Pre-irradiation materials analysis of ρ, μ, and τ and activation analysis indicate that silicon from all sources are roughly comparable in quality. The largest exception is in minority carrier lifetime, τ, which is not as large as advertised in many cases.
- Theoretical analysis of the behavior of n, R_H, μ, and ρ versus fluence has been developed to evaluate results of neutron doping compensation of undoped materials.
- The theoretical cross section for phosphorus production has been verified to about $\pm$ 1%.
- Estimates have been made on the number of displacements as a function of fast to thermal neutron ratio. Importance of gamma recoil damage calculations have been verified.
- Several differences have been discovered between our annealing results and those found in the literature. These have been explained in terms of fast to thermal neutron ratio, and carrier type immediately after irradiation but before annealing.

- Have related in-core 1 Ω-cm radiation and subsequent annealing results discussed in literature to a radiation damage produced amorphous condition which alters annealing kinetics drastically.
- The activation energy and frequency factor for the electrical activation of transmutation produced phosphorus during annealing has been determined for the first time. This analysis suggests that vacancy-phosphorus pairs (E-centers) are related to the process of recovery of electrical activity.
- "Czochralski-like" annealing has been observed in lightly irradiated silicon ($\Phi \sim 0.5\ \Phi_C$) which suggests that clustering of radiation defects with residual oxygen is a problem which must be solved in float zone doped to concentrations below 0.1 ppb.
- The production of an acceptor defect in concentrations between 5×10^{13} to $5 \times 10^{14} cm^{-3}$ by irradiation and annealing has been demonstrated to be independent of fluence. This strongly suggests that this acceptor is related to an intrinsic residual impurity concentration in the silicon before irradiation. We propose that oxygen, which has been decorated with defects to make it electrically active, is the source of these acceptors. This result is exciting since it suggests that oxygen detection in silicon can easily be extended to lower than present day detection limits by several orders of magnitude.

- We have been able to produce a slightly overcompensated sample in at least one case where the residual uncompensated carrier concentration is $3.77 \times 10^{10} cm^{-3}$ or about $3n_i$. This corresponds to a resistivity of greater than 100,000 Ω-cm.
- A single temperature anneal procedure has been developed.
- The radiation effects of fast neutron fluence have been investigated.
- The thermal to fast ratio of position RSAF has been measured to be about 30:1.
- A series of 15 Ga doped samples have been compensated to [P]/[B] ratios of 1 to 20 for the production of IR detectors.
- Isochronal annealing of Ga doped material has been studied.
- Extensive theoretical work on NTD compensation near intrinsic resistivities has been developed. This knowledge has been used to estimate wafer uniformity as a function of phosphorus to boron ratio. It has been demonstrated conclusively both experimentally and theoretically that wafer uniformity is better in NTD-Si than conventionally doped material by factors of 5:1 to 30:1 over phosphorus to boron ratios of 2:1 to 10:1. In the NTD-Si the resistivity fluctuations for the ratios decrease from about ± 5% at a ratio of 2:1 to percentages too small to measure for a ratio of 10:1. It is, therefore, apparent that nuclear transmutation is an essential technique to produce IR detector array uniformity required for monolithic Si detector arrays.

VI. REFERENCES

1. M. Tanenbaum and A.D. Mills, J. Electrochem. Soc. 108, 171 (1961).

2. M. L. Schultz, Infrared Phys. 4, 93 (1964).

3. J. Messier and J. M. Flores, J. Phys. Chem. Solid 24, 1539 (1963).

4. W. Shockley, Electrons and Holes in Semiconductors, Van Nostrand, New York, (1950), p. 217.

5. Keithley Instruments, Inc., 28775 Aurora Road, Cleveland Ohio 44139.

6. Hewlett-Packard, 1820 Embarcadero Road, Palo Alto, California 94303.

7. Alessi Industries, 3195 Airport Loop Drive, Bldg. C, Costa Mesa, California 92626.

8. Signatone Corporation, 3012 Lawrence Expressway, Santa Clara, California 95051.

9. L. B. Valdes, Proc. I.R.E. 42, 420 (1954).

10. A. Uhlir, Jr., Bell System Tech. J. 34, 105 (1955).

11. A.S.T.M. Standard F84-73, 1916 Race Street, Philadelphia, Pennsylvania 19103.

12. L. J. Van der Pauw, Philips Res. Repts. 13, 1 (1958).

13. J. R. Ehrstein, ed., Semiconductor Measurement Technology, Spreading Resistance Symposium, NBS Special Publication 400-10, U.S. Dept. of Commerce, (December, 1974).

14. S. M. Ryvkin, Photoelectric Effects in Semiconductors, Consultants Bureau, New York, (1964).

15. General Radio, 300 Barker Ave., Concord, Massachusetts 01742.

16. Tektronix, Inc., P.O. Box 500, Beaverton, Oregon 97077.

17. S. M. Ryvkin, Ibid., p. 19-23. The equation (8.8) in this reference is incorrect. This expression should be written $V_m = V(\Delta\sigma/\sigma_c)[1 + (1 + \Delta\sigma/\sigma_o)]^2$. This error does not change the conclusions drastically; however, the correct expression has been used to obtain Eq. (20) in this report.

18. Air Products and Chemicals, Inc., Advanced Products Div., 1919 Vultee Street, Allentown, Pennsylvania 18103.

19. Patrick M. Hemenger, Rev. Sci. Instrum. 44, 698 (1973).

20. Varian Instrument Division, 611 Hansen Way, Palo Alto, California 94303.

21. J. S. Blakemore, Semiconductor Statistics, Pergammon Press, New York (1962), p. 140.

22. Ibid. p. 148.

23. Ibid. p. 149.

24. Ibid. p. 58.

25. H. D. Barber, Solid-State Electronics 10, 1039 (1967).

26. F. J. Morin, et al., Phys. Rev. 96, 833 (1954).

27. N. F. Mott and W. D. Twose, Adv. in Phys. 10, 107 (1961).

28. A. Miller and E. Abrahams, Phys. Rev. 120, 745 (1960).

29. B. T. Shklevskii, Sov. Phys. Semicond. 6, 1053 (1973).

30. R. Baron, M. H. Young, J. K. Neeland and O. J. Marsh, Appl. Phys. Lett. 30, 594 (1977).

31. G. H. Kinchin and R. S. Pease, Repts. Prog. in Phys. 18, 1 (1955).

32. J. J. Loferski and P.P. Rappaport, Phys. Rev. 98, 1861 (1955); Ibid. 111, 432 (1958); J. Appl. Phys. 30, 1296 (1959).

33. D. S. Billington and J. H. Crawford, Jr., Radiation Damage in Solids, Princeton University Press, Princeton, N. J., (1961), Chapter 2.

34. J. J. Kalwaski and R. K. Thatcher, TREE Handbook, Defense Atomic Support Agency, DASA1420, p. E-26.

35. Ibid. p. E-28

36. H. C. Schweinler, J. Appl. Phys. 30, 1125 (1959).

37. M V. Chukichev and V. S. Vavilov, Sov. Phys. Semicond. 3, 1103 (1961).

38. V. A. Kharchenko and S. P. Solov'ev, Sov. Phys. Semicond. 5, 1437 (1972).

39. V. N. Mordkovich, S.P. Solov'ev, E. M. Temper, V.A. Kharchenko, Sov. Phys. Semicond. 8, 139 (1974).

40. J. W. Mayer, L. Eriksson and J. A. Davis, Ion Implantation in Semiconductors, Academic Press, New York (1970), p. 100.

41. Ibid. p. 7.

42. Ibid. p. 6.

43. Ibid. pp. 114-115.

44. G. D. Watkins and J. W. Corbett, Phys. Rev. 134, A1359 (1964).

45. H. Saito, M. Hirata, and T. Horiuchi, J. Phys. Soc. Japan 18, Suppl III, 246 (1963).

46. M. Arst, Rockwell International, Space and Missile Division, 3370 Miraloma Avenue, Anaheim, California 92803, private communication.

47. W. E. Haas and M. S. Schnöller, J. Electron. Mat. 5, 57 (1976).

48. H. A. Herman and H. Herzer, J. Electrochem. Soc. 122, 1568 (1975).

49. H. M. Janus, I.E.E.E. Trans. Electron. Devices ED-23, 797 (1976).

☆U.S. Government Printing Office: 1978 — 757-080/761